INTERNAL CHARACTERISTICS OF MAGNETIC CLOUDS AND INTERPLANETARY CORONAL MASS EJECTIONS

Von der Fakultät für Physik und Geowissenschaften
der Technischen Universität Carolo-Wilhelmina
zu Braunschweig
zur Erlangung des Grades eines
Doktors der Naturwissenschaften
(Dr.rer.nat.)
eingereichte
D i s s e r t a t i o n

von Luciano Rodriguez Romboli
Aus Mendoza / Argentinien

Vorveröffentlichungen der Dissertation

Teilergebnisse aus dieser Arbeit wurden mit Genehmigung der Gemeinsamen Naturwissenschaftlichen Fakultät, vertreten durch den Mentor oder den Betreuer der Arbeit, in folgenden Beiträgen vorab veröffentlicht:

Publikationen

· Rodriguez L. and G. Stenborg, El clima espacial: satélites y astronautas en peligro?, Ciencia Hoy, 13(74), 10–22, 2003.
· Rodriguez L., J. Woch, N. Krupp, M. Fränz, R. von Steiger, R. Forsyth, D. Reisenfeld, and K.-H. Glaßmeier, A statistical study of oxygen freezing-in temperature and energetic particles inside magnetic clouds observed by Ulysses, J. Geophys. Res., 109, A01108, doi:10.1029/2003JA010156, 2004.
· Rodriguez L., J. Woch, N. Krupp, M. Fränz, R. von Steiger, C. Cid, R. Forsyth, K.-H. Glaßmeier, Bidirectional proton flows and comparison of freezing-in temperatures in ICMEs and magnetic clouds, Proc. IAU Symposium 226 on Coronal and Stellar Mass Ejections, Beijing, China, 2004 (submitted).
· Wimmer-Schweingruber R.F. et al., In-situ Solar Wind and Field Signatures of Interplanetary Coronal Mass Ejections, Report of Working Group B, Space Science Reviews, in press, 2004. (ISSI CME book).
· Gazis P. et al., Interplanetary Coronal Mass Ejections in the Outer Heliosphere and at High Latitudes, Report of Working Group H, Space Science Reviews, in press, 2004. (ISSI CME book).

Tagungsbeiträge

· Rodriguez L., J. Woch, N. Krupp, M. Fränz, R. von Steiger, R. Forsyth, Multi-Instrument study of Interplanetary Coronal Mass Ejections (ICMEs), (poster), EGS-AGU-EUG Joint Assembly, Nice, France, April 2003.
· Rodriguez L., J. Woch, N. Krupp, K.-H Glassmeier, Characterization of Interplanetary Coronal Mass Ejections (ICMEs) seen by Ulysses, (oral), IMPRS seminar at MPS, Katlenburg-Lindau, Germany, May 2003.
· Rodriguez L., J. Woch, N. Krupp, K.-H Glassmeier, Coronal Mass Ejections seen in interplanetary space, (oral) Seminar of the Institut für Geophysik und Meteorologie, TU Braunschweig, Braunschweig, Germany, December 2003.
· Rodriguez L., J. Woch, N. Krupp, K.-H Glassmeier, Signatures of Magnetic Clouds in the solar wind, (oral), IMPRS seminar at MPS, Katlenburg-Lindau, Germany, February 2004.
· Rodriguez L., J. Woch, N. Krupp, and M. Fränz, Eyecciones coronales de masa vistas en el espacio interplanetario, (oral), Universidad de Alcalá, Madrid, Spain, January 2004.
· Rodriguez L., J. Woch, N. Krupp, M. Fränz, R. von Steiger, and K. H. Glassmeier, A statistical study of oxygen freezing-in temperature and energetic particles inside

magnetic clouds observed by Ulysses, (poster), European Geosciences Union, Nice, France, April 2004.

· Rodriguez L., J. Woch, N. Krupp, M. Fränz, R. von Steiger, C. Cid, R. Forsyth and K. H. Glassmeier, Internal structure of magnetic clouds seen by Ulysses, (oral), COSPAR, Paris, France, July 2004.

· Rodriguez L., J. Woch, N. Krupp, M. Fränz, R. von Steiger, C. Cid, R. Forsyth and K. H. Glassmeier, Topology and internal structure of magnetic clouds inferred from Ulysses measurements, (oral), IAU Symposium 226 on Coronal and Stellar Mass Ejections, Beijing, China, September 2004.

To my family…

Abstract

Coronal Mass Ejections (CMEs) are extremely dynamical and huge events in which the solar plasma, initially contained in closed coronal magnetic field lines, is ejected into interplanetary space. When a CME is detected in-situ by a spacecraft located in the interplanetary medium, it is then termed Interplanetary CME (ICME). A set of signatures in plasma and magnetic field data is used to identify it. Among ICMEs, Magnetic Clouds (MCs) represent a special kind of ICME in which the internal magnetic field configuration resembles that of a flux rope (a twisted helical magnetic filament). Using in-situ data provided by instruments onboard the heliospheric mission Ulysses, 40 magnetic clouds have been identified out of 147 ICMEs in the time period between 1992 and 2002. These events constitute the database for this thesis.

The ionization level of the solar wind plasma serves as a robust tool to characterize the different types of solar wind. Charge states of heavy ions have been used in this work to infer the temperatures in the source region of ICMEs. MCs show increased temperatures with respect to non-cloud ICMEs and surrounding solar wind. By combining these data with a magnetic field model, insights into the internal structure of magnetic clouds are provided. Zones of increased temperatures are found to be confined to the flux rope region. Different elements provide information on the temperature at different heights in the solar corona. The temperature obtained from oxygen ions shows larger differences with the surrounding solar wind when compared with the temperatures from carbon and iron. In this way, oxygen ions are the best tracers for magnetic clouds in the solar wind.

Energetic particles can be used to study the ICME topology, internal structure and magnetic connectivity to the Sun. The intensity response of protons and helium ions to a magnetic cloud passage depends heavily on the energetic background, governed by the conditions in which each event is immersed. The elemental composition of the population contained in magnetic clouds has been used in this thesis to identify the mechanism by which these particles are accelerated. The abundance ratios found are consistent with those for gradual solar energetic particle events (SEPs). In this mechanism, interplanetary shocks (simultaneous, abrupt jumps in the magnetic field, speed, density, and temperature of the plasma) accelerate particles from the solar wind suprathermal population up to the MeV range. Directional anisotropies of the energetic particles are used to infer magnetic topology of the MCs. The energetic protons within magnetic clouds are found to be predominantly bidirectional, pointing towards closed magnetic structures, probably with one or both foot points connected back to the Sun.

CONTENTS

LIST OF FIGURES

LIST OF TABLES

Chapter 1   Introduction

The Sun, as a highly dynamic star, influences the Earth as well as the whole interplanetary space, up to the far limits of the Heliosphere. In this chapter, an overview of the solar structure, its most important properties and dynamics will be presented; along with a description of the solar wind and solar transient events. The solar wind represents the medium by which the Sun extends its atmosphere swiftly into the vastness of the solar system. It was first discovered more than 50 years ago, but the properties of the solar wind are still being investigated and, some, newly discovered by modern space missions. The magnetic field of the Sun, embedded in the solar wind, is convected outwards. In this way, the so-called Interplanetary Magnetic Field (IMF) is formed. Its geometry and general properties are tightly bound to the Sun's activity and rotation. The IMF provides a path for charged particles, accelerated at the Sun and further out, to propagate into interplanetary space. Different mechanisms may cause thermal or suprathermal particles to be accelerated up to fractions of the speed of light. In interplanetary space, shocks created by speed or pressure differences between solar wind parcels are one of the responsible causes for this acceleration. Shocks are expected to appear in connection with disturbances in the solar wind. The most important ones in terms of space weather, geoeffectiveness, energy release and rate of occurrence, are Coronal Mass Ejections (CMEs) and their interplanetary counterparts (ICMEs). Among them, Magnetic Clouds (MCs) are a special subset in which the magnetic field structure is organized in a particular way. They are of key importance in understanding interplanetary evolution of CMEs. Furthermore, MCs are of utmost relevance regarding space weather issues, since they are very prone to affect the Earth magnetosphere, due to their characteristic internal magnetic field structure. An introduction to these topics, along with the objectives of this work will be presented in this chapter.

1.1   The Dynamic Sun and the Heliosphere

1.1.1 Structure of the Sun

Figure 1.1 provides a general overview of the Sun's structure. Each of the various layers in which the Sun is divided exhibits distinctive properties and processes.
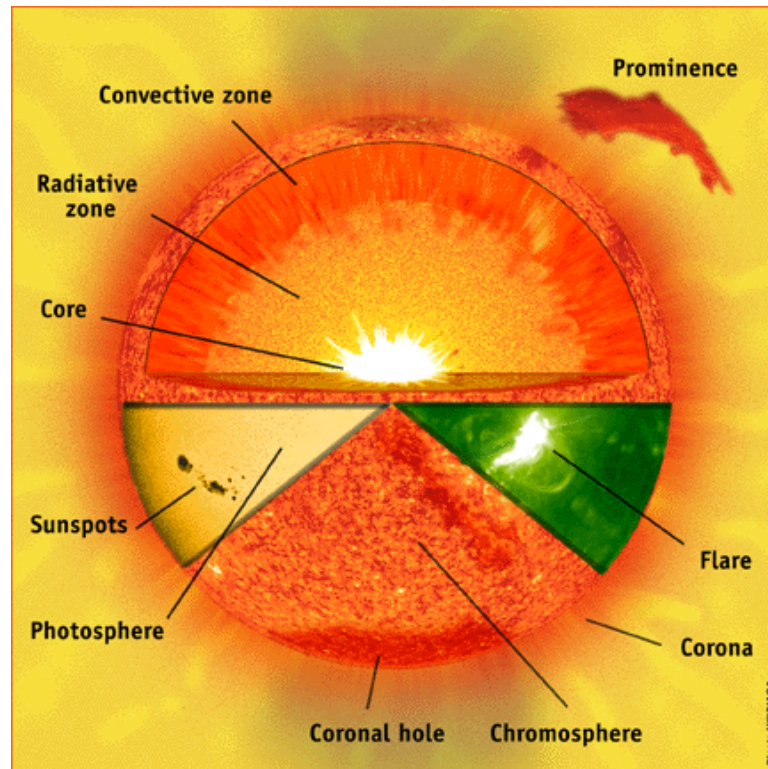
Figure 1.1: Solar Interior and atmosphere. From center to surface: the core, the radiative zone, and the convective zone. The solar atmosphere comprises the photosphere, the chromosphere, and finally the outermost layer, the corona. From "SOHO Explore" (sohowww.nascom.nasa.gov)

The core extends up to 25% of the solar radius (Rs). There, the Sun's energy is generated by fusion of hydrogen into helium. The energy is then transported to the surface through the radiative zone by radiation processes. This zone extends from the external part of the core up to 80% of the solar radius. The density and temperature decrease here from $20g/cm^3$ and $7x10^6$ K, respectively, to $0.2g/cm^3$ and $2x10^6$ K in the uppermost part. The outermost layer in the solar interior is the convective zone. In this region, the opacity of the plasma is so high that transport by radiation is no longer possible and it is then replaced by convection.

The solar atmosphere can also be divided in different layers. Height is measured outwards from the level at which the optical depth τ (at 5000 Å) is unity. The optical depth τ gives a measure of how opaque a medium is to radiation passing through it. It is measured downwards from the top of the atmosphere, so that it equals 0 at the top and 1

at the surface. The lower layer is called photosphere, which is less than 1% Rs thick. It is normally considered as the surface of the Sun. After reaching a minimum of 4300 K, the temperature gradually increases with height, this region is called chromosphere. At 2000 km above the photosphere, the temperature reaches 8500 K. At this point, the hydrogen is no longer capable of emitting the dissipated heat. As a consequence the temperature increases up to 500000 K in a few hundred km. This thin region of abrupt temperature increase is called transition zone. In the outermost layer of the atmosphere, the corona, the temperature continues rising, reaching one million degrees at 8000 km height. Figure 1.2 shows the temperature and density profiles in the solar atmosphere. A comprehensive and detailed view on these topics is given by Lang [2001].
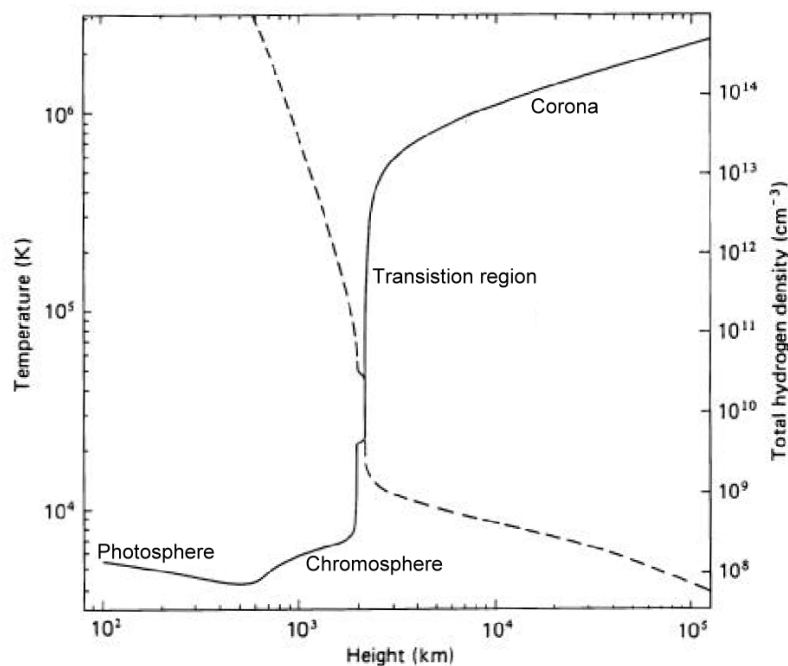
Figure 1.2: Temperature and density of the solar atmosphere as functions of the distance from the solar surface. From Cravens [1997].

1.1.2 The corona and solar wind

The abrupt increase of the temperature in the transition region ends in the corona. The high temperature levels (around 10^6 K) are maintained through several solar radii (1 R_s = 6.96 x 10^8 m). Due to the low densities prevailing in the corona and the high luminosity of the solar photosphere, the corona is only visible during solar eclipses or by the means of coronagraphs which cover the solar disk. A coronagraph is a telescope used to observe the corona by measuring photospheric light scattered by free electrons and dust particles. It uses an occulting element to cover the glare of the Sun's disk. The top right panel of Figure 1.3 shows the corona during solar maximum in 2002. An eclipse view of the corona during solar minimum can be seen in the top left panel of Figure 1.3. In the

bottom panel, a sketch of the magnetic field configuration for each case is shown. The top right image in Figure 1.3 was obtained by the LASCO (Large Angle Spectroscopic Coronagraph; Brueckner et al., 1995) instrument, a package of three coronagraphs that together image the solar corona from 1.1 to 30 R_s. LASCO is onboard SOHO (Solar and Heliospheric Observatory; Domingo et al., 1995), an ESA/NASA space mission developed to obtain a better understanding of the structure and dynamics of the Sun.
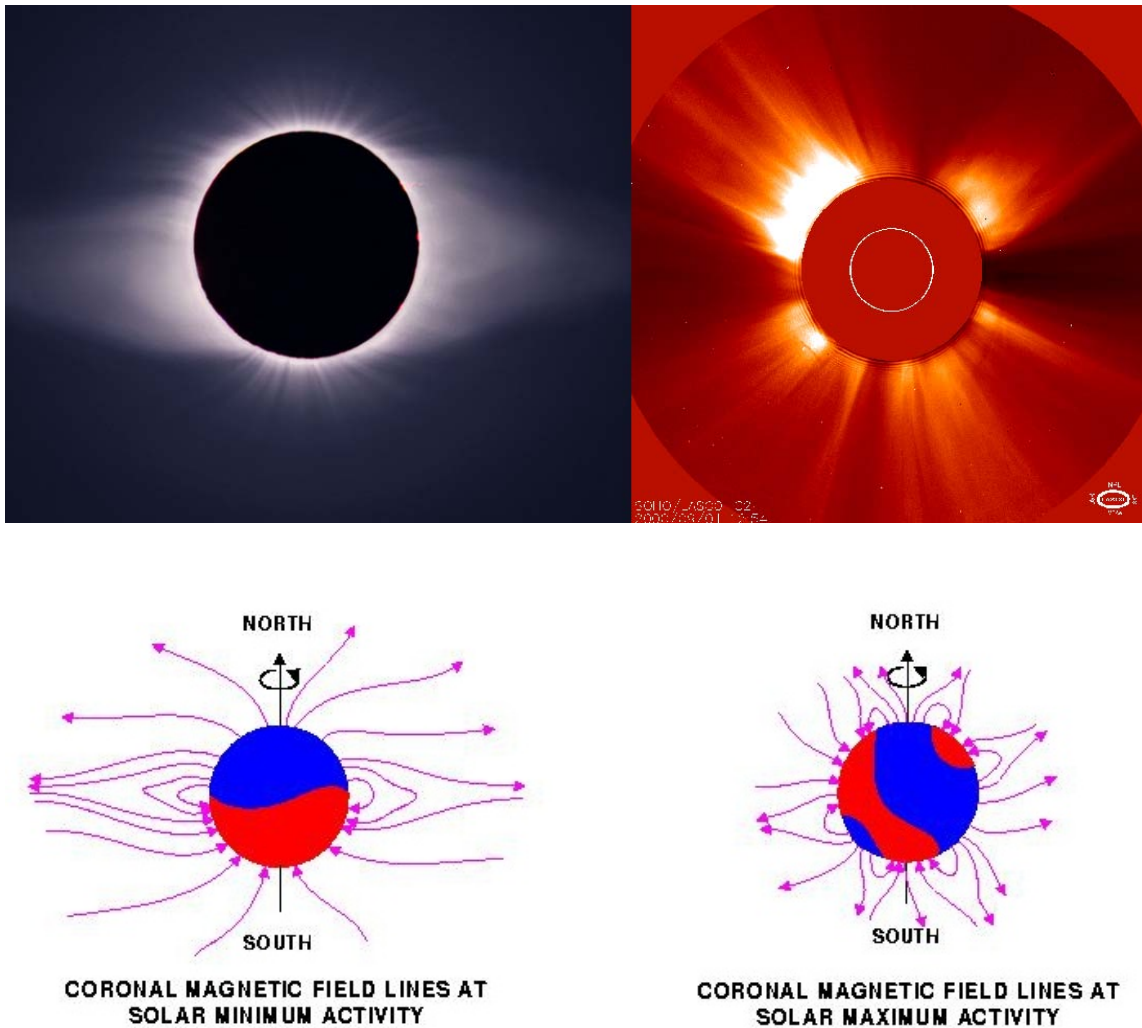
Figure 1.3: Top Left: Eclipse of October 1995, photo by Wendy Carlos and Fred Espenak. Top Right: The corona in September 2000, as observed by the LASCO C2 coronagraph, onboard SOHO (ESA & NASA). Bottom: Coronal magnetic field lines at solar minimum and solar maximum (courtesy R. Forsyth, http://www.sp.ph.ic.ac.uk/~forsyth/reversal/), the colors and arrows represent the different magnetic polarities.

The coronal temperature is much higher than the temperature of the photosphere. This fact is in contrast to the simple picture of a hot star in a cool interstellar environment. Large amounts of energy should be pumped into the corona to maintain the temperature difference. The processes which generate and supply this excess energy are not yet known. The corona cannot be in hydrostatic equilibrium and is therefore in continuous expansion, this expansion forms the solar wind (SW), which sweeps out up to the most

remote parts of the solar system. The fact that there exists a continuous particle stream emanating from the Sun came to light by indirect measurements, observing the ion tails of comets which point radially away from the Sun. Hoffmeister [1943], found nevertheless that the ion tail is deviated ~5° from the solar radius vector. Almost a decade later, Biermann [1951] realized that the radiation pressure of the sunlight could not account for the accelerations observed in the ion tails and proposed a corpuscular radiation instead. In this way, he was able to explain that the deviation angle of the tail is given by the ratio between the comet's transverse orbital velocity component and the velocity of the corpuscular radiation. Parker [1958a] found that the topmost layers of the corona must flow away from the Sun at a velocity like that of Biermann's corpuscular radiation. The flow was termed *solar wind* by Parker [1958b], and accepted widely after Neugebauer and Snyder [1962] demonstrated definitely its existence with data from the Mariner-2 probe on its way to Venus.

The solar wind is a collisionless plasma consisting mostly of protons (~95%), double ionized helium (or alpha particles, ~4%), and trace amounts of heavy ions. The heavy elements, even though rare, provide extremely important information about the origin of the solar wind and about transient processes occurring in the Sun's atmosphere and in the heliosphere.

In-situ measurements of solar wind plasma demonstrated the existence of latitudinal gradients in solar wind speed. With the Helios spacecraft the bimodal nature of the solar wind was exposed (Bame et al., 1977; Schwenn et al., 1978). The fast wind (with speeds above 600 km/s) originates in coronal holes. The slow wind (speed below 400 km/s) originates in the regions were the magnetic configuration is dominated by closed loops with both ends of the magnetic field lines rooted on the Sun (see Figure 1.3). Table 1.1 provides some characteristic parameters of the two types of solar wind. The nature of the solar wind was later studied extensively with data from the Ulysses mission (e.g. Woch et al., 1997), results which will be more deeply discussed later in this work.

Parameter	Slow Wind (<400 km/s)	Fast Wind (>600 km/s)
v_p [km/s]	327	702
n_p [cm-3]	8.3	2.7
F_p [108cm-2s-1]	2.7	1.9
n_α/n_p [%]	3.8 (highly variable)	4.8 (stationary)
T_p [10^4 K]	3.4	23
Source	Helmet streamers, loops	Coronal holes
Signatures	Very variable	Stationary

Table 1.1: Parameters of the slow and fast solar wind. Shown are the proton speed (v_p), the proton density (n_p), the proton flux (F_p), the helium to proton ratio (n_α/n_p), the proton temperature (T_p), the sources and signatures. Adapted from Schwenn [1991].

The elemental abundances of the solar wind are different from the ones found in the photosphere. Elements with low first ionization potential (FIP) are enhanced in the solar wind with respect to their photospheric values (factor of ~4 higher in the slow wind and ~2 in the fast wind). This is the so called "FIP Effect". There are several theories which have been developed to explain the FIP effect (e.g., summary by Meyer, 1993).

1.1.3 The solar cycle and the coronal magnetic field

The Sun is an active star. Its activity is not constant, it follows a cycle, called the solar cycle (or the sunspot cycle) which was identified by the variable sunspot numbers. The period of this cycle is in average 11 years, but it varies in time between about 9.5 and 12.5 years. Throughout the solar cycle, changes occur in the Sun's internal magnetic field that affect the surface disturbance level.

During solar activity minimum, Figure 1.3 left panel, the Sun presents a clear bimodal nature. On one side, the polar regions of the Sun are characterized by the presence of magnetic field lines which extend far out into the heliosphere, termed *polar coronal holes*. They possess low density and are the main source of the fast solar wind. The second distinctive region in solar minimum is the activity belt around the solar equator, the streamer belts. This is an area dominated by closed magnetic field loops, with both ends anchored in the Sun. The slow solar wind originates from this region.

During solar activity maximum, Figure 1.3 right panel, the situation is very different. Closed loop configurations can be seen covering most of the Sun's surface. The streamer region around the equator is highly tilted and there are more streamers forming and disappearing constantly. Coronal holes are generally much smaller and can be seen at any latitude.

After each cycle, the solar magnetic field reverses polarity (the blue changes to red and vice versa in the bottom left panel of Figure 1.3).

1.1.4 The interplanetary magnetic field

The solar activity and its influence is a consequence of the existence of the Sun's magnetic field. The structure of the heliosphere is heavily dominated by this field, the solar wind and the rotation of the Sun. Due to the almost infinite conductivity of the plasma, the magnetic field is frozen into the solar wind. In this way, the shape of the magnetic field lines will be determined by the plasma flow velocity and the Sun's rotation. Parker [1958a] illustrated in his model the spiral shape of the interplanetary magnetic field (IMF), shown in Figure 1.4. The mathematical treatment of the frozen in concept and, in general, of well known plasma processes which are covered in space plasmas textbooks (e.g. Baumjohann and Treumann, 1997) will not be discussed here.
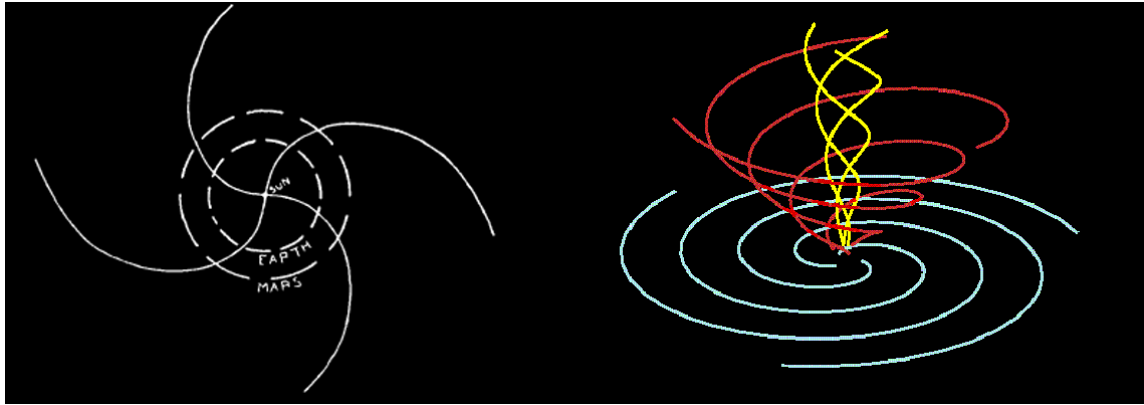
Figure 1.4: Left: Spiral shape of the IMF in the ecliptic plane, carried out by the solar wind. From Parker [1958a]. Right: Extension of the Parker configuration to high latitutes, from solar-heliospheric.engin.umich.edu/Theory/.

Fisk [1996] proposed a different configuration to the one shown in Figure 1.4. He noticed that the footpoints of the magnetic field on the solar wind source surface rotate differentially about their axis. The fact that the Sun's magnetic field is not only constantly expanding, but it is slightly offset from the Sun's axis of rotation is also considered. One of the important consequences of this model is that field lines connect directly from low to high heliospheric latitudes, allowing for example the transport of energetic particles from low to high latitudes without the need for cross-field diffusion. The configuration of the heliospheric magnetic field for high heliolatitudes resulting from this model is shown in Figure 1.5.
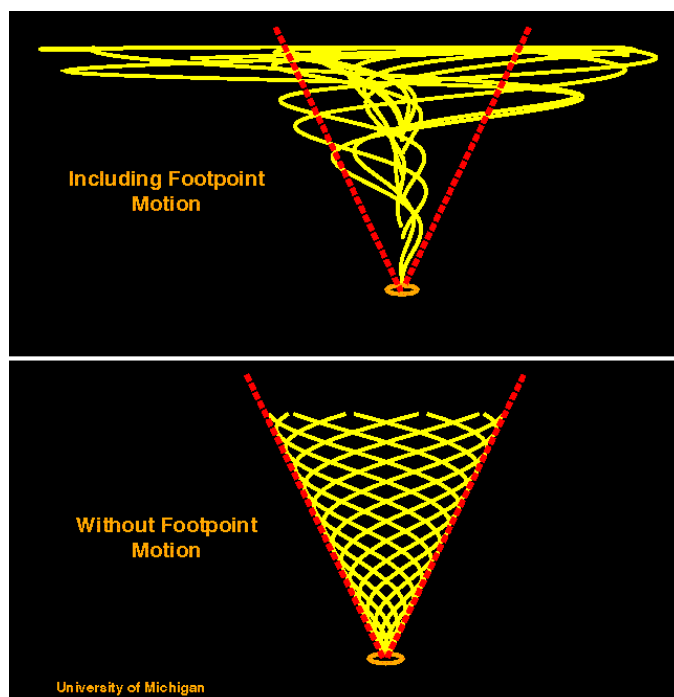
Figure 1.5: The top panel depicts the modifications to the high latitude Parker heliospheric field (bottom panel). After Fisk [1996], from solar-heliospheric.engin.umich.edu.

1.2   Solar disturbances and ejections of solar mass

1.2.1 Flares and Coronal Mass Ejections (CMEs)

Early in 1860, Carrington was the first who observed a solar flare and noticed a connection with a strong geomagnetic storm only 17 hours later. Flares occur when magnetic energy accumulated in the solar atmosphere is suddenly released. They are recognized in UV and X-rays as a sudden and intense variation in brightness, as shown in Figure 1.6. As the magnetic energy is being released, particles are extremely heated (to temperatures higher than 10 million K) and accelerated. These particles are detected later in interplanetary space, even in the near-Earth space, and beyond.
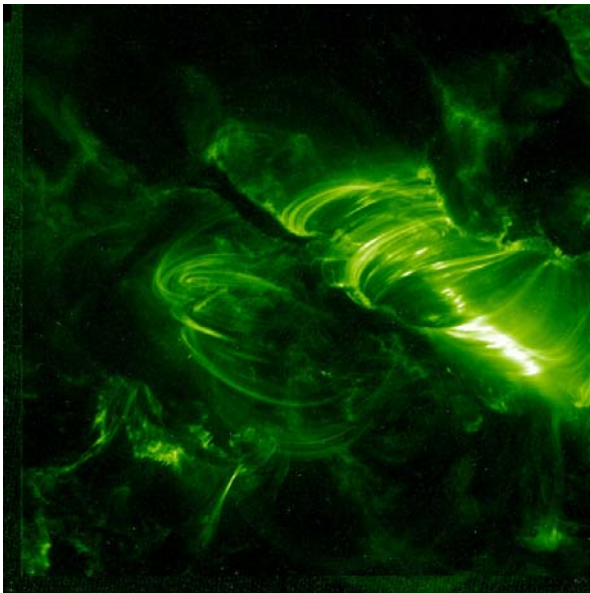
Figure 1.6: Strong flare in April 2000, observed by TRACE. Credit: NASA / LMSAL.

For a long time flares were believed to be the drivers of geomagnetic activity. The common association of disturbances in near-Earth space with solar flares led to a paradigm of cause and effect in which large solar flares came to be understood as the fundamental cause of these disturbances (Gosling, 1993a).

Today it is known, that the above paradigm is wrong (e.g. Gosling, 1993b) and that most major, transient disturbances in near-Earth space are produced by solar events known as Coronal Mass Ejections (CMEs). The relation between CMEs and flares is not very well established. They are seen either occurring together or separated. It seems that neither of them represents a necessary cause for the other to occur. Both phenomena are a consequence of the always changing solar magnetic field.

CMEs are extremely dynamical huge events in which the plasma, initially contained in closed coronal magnetic field lines, is ejected into interplanetary space. CMEs were not observed directly until coronagraphs were first flown in space in the early 1970s (OSO-7 and Skylab). Currently with SOHO, providing solar coverage since 1996, the amount of

data on CMEs has served to demonstrate the huge diversity presented by them:

- Speeds varying from 50 to more than 2000 km/s.
- Angular widths from a few degrees up to 360°
- More than 3 events (on average) are observed per day during solar maximum. During solar minimum CMEs are originating close to the equator and occur, on average, less than once per day.
- Ejected mass from 5 to 50 billion tons
- Energies between 10^{23} and 10^{24} J

Halo CMEs (CMEs propagating in the direction of the Sun-Earth line) may reach the Earth in a matter of days or even hours, as was the case of the CME in October 29th 2003, which arrived at Earth in less than 19 h. If this flow of charged particles and embedded magnetic field collides with Earth, it can have dramatic effects on the magnetosphere, ionosphere and even at ground level. The resulting geomagnetic storms can cause disruptions in communication networks, errors in navigation and geophysical systems, satellite failures (see e.g. Rodriguez and Stenborg, 2003), electricity blackouts, radiation hazards to astronauts and disruption of flow meters in oil pipelines.

In Figure 1.7 a non-halo CME observed by the LASCO coronagraph on SOHO is shown. In this image, one can observe the so called 3-part structure, formed by a leading edge, a dark void or cavity and a bright kernel. Each of these structures is believed to have a correspondence on features observed in X-Ray or EUV, but unambiguous identification has not been achieved. Even greater ambiguity exists when the attempt to identify the features is made in interplanetary space (see e.g. Gopalswamy et al., 1998). The MHD model of CME initiation proposed by Low and Zhang [2002] (see also references therein) identifies the CME front with the expelled coronal mass, the cavity with a flux rope and the bright kernel with an erupted prominence. This is the scheme most widely adopted.

The mentioned diversity regarding CME properties is of course also present in their morphology. Classification schemes based on different characteristics observed in white light have been developed (e.g. Cremades and Bothmer, 2004) in order to find a link between the distinctive features seen in coronagraphs and the origin of CMEs.
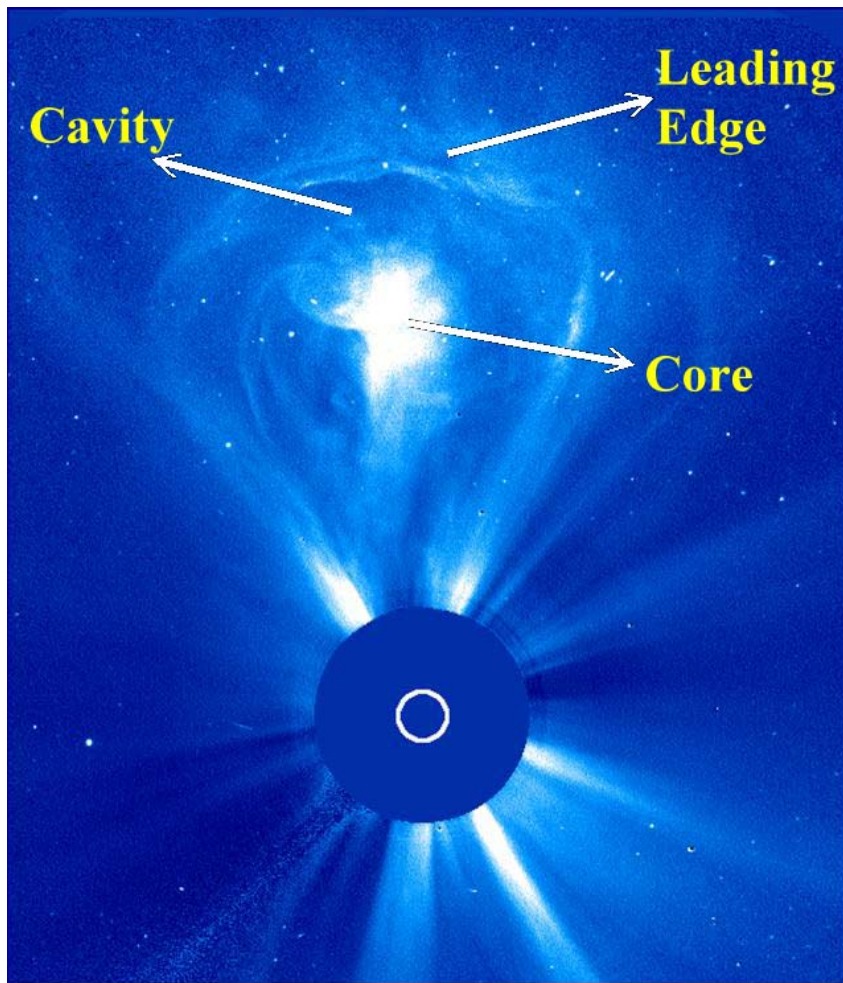
Figure 1.7: CME captured by the LASCO coronagraph onboard SOHO. The so-called 3-part structure is clearly seen in this event. Image courtesy SOHO/LASCO.

In the next years much is expected from the upcoming STEREO mission (Rust, 1998), which will provide stereoscopic views on CMEs. In spite of the technological advances, important basic questions such as the flare-CME relation or the fate of the 3-part structure in interplanetary space are still open.

1.2.2 Interplanetary Coronal Mass Ejections (ICMEs)

If a CME is detected in-situ by a spacecraft located in the interplanetary medium, it is called ICME. This is connected to the definition of CME by Munro [1979]: "A CME is a new, discrete, bright feature appearing in the FOV of the coronagraph and moving outwards over a period of minutes to hours". An ICME is simply the interplanetary manifestation of a CME, even though there is nothing 'simple' about it.

Some features found in CMEs are not found in ICMEs and vice versa. There are, for example, no clear signs of a 3-part structure in in-situ data. Nevertheless, for isolated cases, authors have been able to find cold plasma trailing an ICME (Schwenn et al., 1980; Gosling et al., 1980) which resembles the chromospheric prominence material. Some ICMEs drive shocks in interplanetary space, but these are not identified in coronagraph data.

ICMEs are detected by a set of signatures, defined in Table 1.2. This table represents a collection of the signatures related to ICMEs by several authors gathered from the

literature. It is extremely rare to see every signature occurring for a single ICME. Normally only a subset of them is present. Furthermore it may occur that portions of an ICME are characterized by certain signatures and other parts of the same structure present different signatures. None of the mentioned signatures is a necessary condition for ICME identification, meaning that any of them can be absent and the structure may still be an ICME. Neither is any of them a sufficient condition, which by its sole presence allows to confidently identify an ICME in a solar wind parcel. Because of these reasons, the identification of ICMEs in solar wind plasma and magnetic field data is still 'something of an art' (Gosling, 1990).

A further difficulty in identifying ICMEs is the determination of boundaries. Signatures do not normally correlate exactly in time and space. Where the event starts and where it ends depends somehow on the weight that each of the different signatures is given.

One of the signatures more commonly used for the identification of ICMEs is the presence of bidirectional suprathermal electron distributions (BDEs) of ~100eV. The flow of counterstreaming electrons along magnetic field lines indicate that either the ends of these field lines connect back to the corona or that the field lines form a closed loop, entirely disconnected from the Sun. The latter explanation of the phenomena (e.g. Montgomery et al., 1974) is being gradually replaced by the former (e.g. Larson et al., 1997).

Signature	Physycal Significance	Selected reference
Decreased proton T	Expansion	Richardson and Cane [1995]
Negative V slope	Expansion	Klein and Burlaga [1982]
Upstream forward shock	Superalfvénic speed / expansion	Parker [1961]
$T_e > T_p$	Expansion	Richardson et al. [1997]
Ion acoustic waves	Expansion	Lin et al. [1999]
n_α/n_p enhancement	Source process (flare relation?)	Hirshberg et al. [1972]
$^3He/^4He$ enhancement	Prominence material	Ho et al. [2000]
Highly ionized ions	High T in source region	Henke et al. [2001]
Occurrence of He+	Chromospheric material	Schwenn et al. [1980]
Bidirectional suprathermal electrons	Closed magnetic structures	Gosling et al. [1987]
Bidirectional ~MeV particles	Closed magnetic structures	Marsden et al. [1987]
Cosmic Ray depletions	Magnetic shielding	Cane [2000]
Rotation in B	Flux rope	Klein and Burlaga [1982]
Enhancement and low variance in |B|	Magnetically dominated structure	Klein and Burlaga [1982]
Low plasma beta	Magnetically dominated structure	Burlaga [1991]

Table 1.2: Signatures used to identify ICMEs in the Heliosphere. Partially from Zurbuchen and Richardson [2004].

The global magnetic structure of ICMEs has been a subject of much debate for a long time (e.g., Morrison, 1954; Cocconi et al., 1958; Gold, 1959). Tongue, bottle, bubble, and connected or disconnected configurations have been proposed (Figure 1.8). Suprathermal particles serve as tracers of magnetic field lines, providing information on the global configuration of ICMEs and a tool for discerning between these different

ICMEs topologies due to their small gyroradii, high speed and large particle scattering mean free paths in the smooth magnetic field typical of ICMEs (e.g., Richardson et al., 1997).

Particles of higher energies have also been used as tracers of the magnetic field (e.g. Marsden et al., 1987) in order to infer which magnetic configuration is present in the ICME. Bidirectional flows of energetic particles may point towards a possible connection of the CME legs into the Sun. Furthermore, the composition of these high energy particles provides important clues to identify correctly the acceleration mechanism and origin of the particles (see Section 1.3).

In the thermal energy range, charge state composition provides information on its source region in a similar way (but not quite the same) as the composition information for higher energy particles. By measuring solar wind charge states in interplanetary space, properties of its source on the Sun can be derived. It is in this way, that composition analysis of the thermal population provides valuable information for ICME identification and further classification. They represent a less explored field in ICME research than bulk plasma and magnetic field analysis, mainly because of highly demanding instrument requirements.
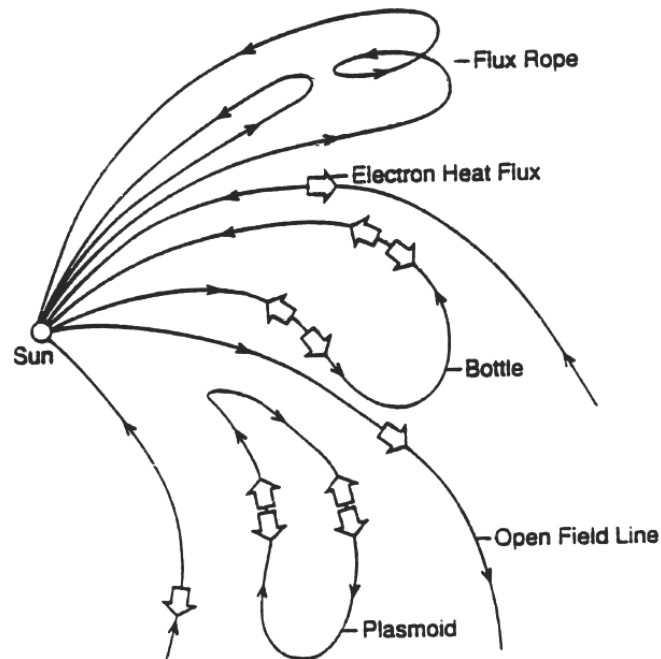
Figure 1.8: Schematic illustrations of four generic types of interplanetary magnetic topologies. At bottom is a simple open topology, connected at one end to the Sun and at the other end to the interstellar medium. Heat flux is expected to be uni-directional away from the Sun as shown by the arrow. Just above is a completely disconnected plasmoid. Heat flux is expected to be either absent or bidirectional. Next above is a magnetic bottle or tongue, connected at both ends to the Sun. The heat flux here is also expected to be bidirectional. At the top is pictured the simplest flux-rope topology. It is also connected at both ends to the Sun but contains one or more loops. From Feldman and Marsch [1997].

1.2.3 Magnetic Clouds (MCs)

If a certain subgroup of the signatures described in Table 1.2 is present in an ICME, then this structure is called a Magnetic Cloud (MC). The specific signatures which have to be present are the following:

- Smooth rotation in **B** with low variance
- Low proton temperature
- Low plasma beta

The presence of these three signatures clearly states that Magnetic Clouds represent a kind of ICMEs in which the magnetic field shows a certain degree of order, allowing the use of magnetic field models and numeric tools which ease the identification and characterization of MCs.

The magnetic field inside a MC consists of twisted helical lines with decreasing angle between the helical lines and the axial field, from the edges to the center (see Figure 1.9). That is why in-situ magnetic field data show a smooth rotation of the magnetic field as the spacecraft is immersed in the cloud. It is assumed that MCs are the interplanetary manifestation of solar flux ropes, since their magnetic structure resembles that of a flux rope. Whether all ICMEs include a flux rope, which is then 'lost' or simply not sampled in the case of non-cloud ICMEs, is still not clear.
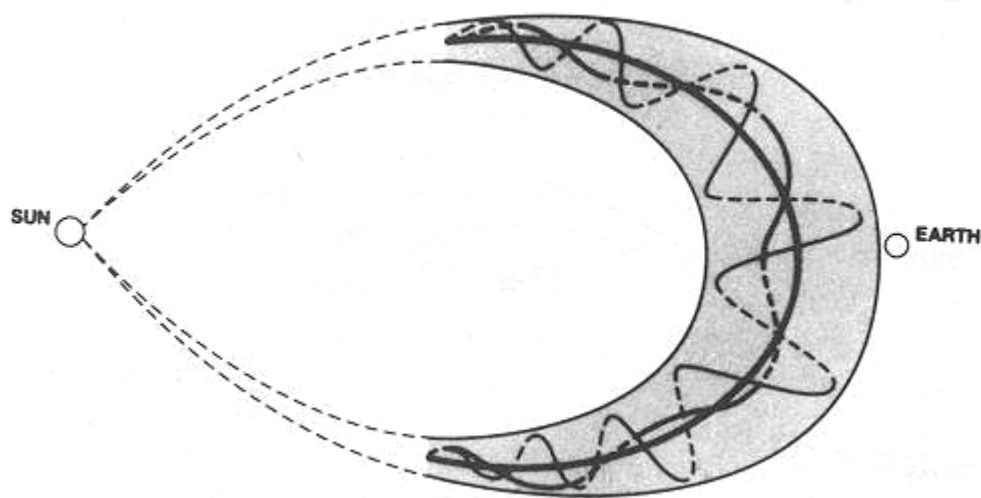
Figure 1.9: Magnetic field configuration inside a MC. From Burlaga. [1990].

The general knowledge of the magnetic configuration in MCs has been obtained from in-situ measurements and comparison with on-disk images. With magnetometers onboard spacecrafts such as Ulysses (examples and detailed explanation are given in Chapter 3) a rotation in the components of the magnetic field vector is seen, which must be of course accompanied by the other required signatures. The rotation alone is not enough to affirm

the existence of a MC.

Bidirectional suprathermal electrons (BDEs) have also been used to characterize the magnetic structure of MCs. The presence of a counterstreaming flow of electrons along the magnetic field may indicate that the 'legs' of the MC are still connected to the Sun. The streaming direction and the flux of electrons may vary extensively throughout a BDE event (e.g. Crooker et al., 1990; Bothmer et al., 1996), indicating that the connection of the magnetic field lines to the Sun is patchy. Shodhan et al. [2000] found considerable variability in the duration of BDE events inside magnetic clouds and concluded that 'magnetic clouds comprise a random mix of intertwined volumes of magnetically open and closed field lines'. As it was previously mentioned, energetic particles can also be used to trace the magnetic topology of MCs; among others, this point will be pursued in Chapter 5.

A good indication of magnetically dominated structures, such as MCs, is a low plasma beta. The plasma beta is defined as the ratio of plasma to magnetic pressure in the following way:

$$\beta = \frac{nkT}{\mathbf{B}^2/8\pi} \qquad (1.1)$$

Low plasma beta indicates that the magnetic pressure in a cloud is higher than the gas pressure. The total pressure inside a magnetic clouds is normally higher than in the surrounding solar wind, therefore it will expand. At the same time, this expansion will provoke a decrease in the plasma temperature.

As it was mentioned in the previous section, charge states of ions in the solar wind represent a powerful tool to characterize material ejected from the Sun. Henke et al. [1998] introduced the idea that MCs are associated with higher ionization levels than non-cloud ICMEs. In this way, charge states may represent a signature for magnetic clouds, which can complement the already mentioned ones. This point and its possible further implications will be discussed in the following chapters.

Magnetic clouds are normally modelled as cylinders, with the configuration illustrated in Figure 1.10. In Chapter 3, a description of several models (including the one used in this thesis) will be given.
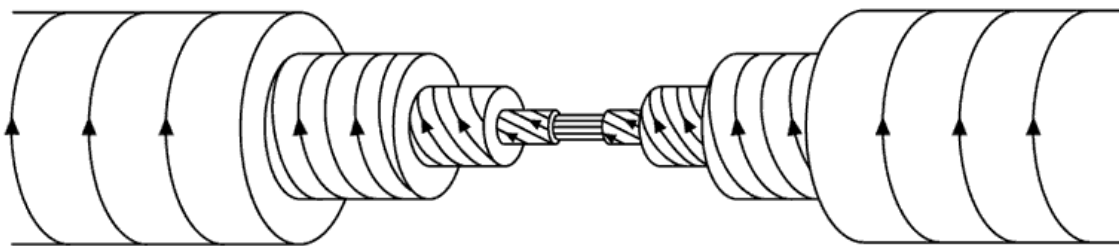
Interior Structure of Flux Rope

Figure 1.10 Internal magnetic field configuration in a flux rope. From Russell and Elphic [1999].

MCs are extremely geoeffective if the magnetic field they contain has a southward orientation. When this condition is fulfilled, reconnection on the dayside of the magnetosphere will be triggered. Magnetic flux from the dayside will be stripped and moved into the magnetospheric tail, so that the dayside magnetopause moves inward, while the tail magnetopause moves out. The field lines in the tail stretch, until they collapse inward towards Earth. In this way, the plasma contained in these field lines is strongly heated and compressed. A sudden intense flux of electrons at the top of the atmosphere is generated, producing a brilliant auroral display as the atmospheric atoms are excited by collisions with the electrons at altitudes above 100 km, and then radiate. The upper atmosphere also becomes much more strongly ionized at these altitudes than before, and hence more electrically conducting. In this manner electric currents flow whose magnetic effects can be observed on the ground.

1.3   Energetic particles in the heliosphere

As can be seen in Figure 1.11, there exists a large variety of processes in the heliosphere which can accelerate particles up to high (keV - GeV) energies. Some of the most important ones, in the frame of this work, will be discussed in this section and a general overview of shock acceleration mechanisms will be given.
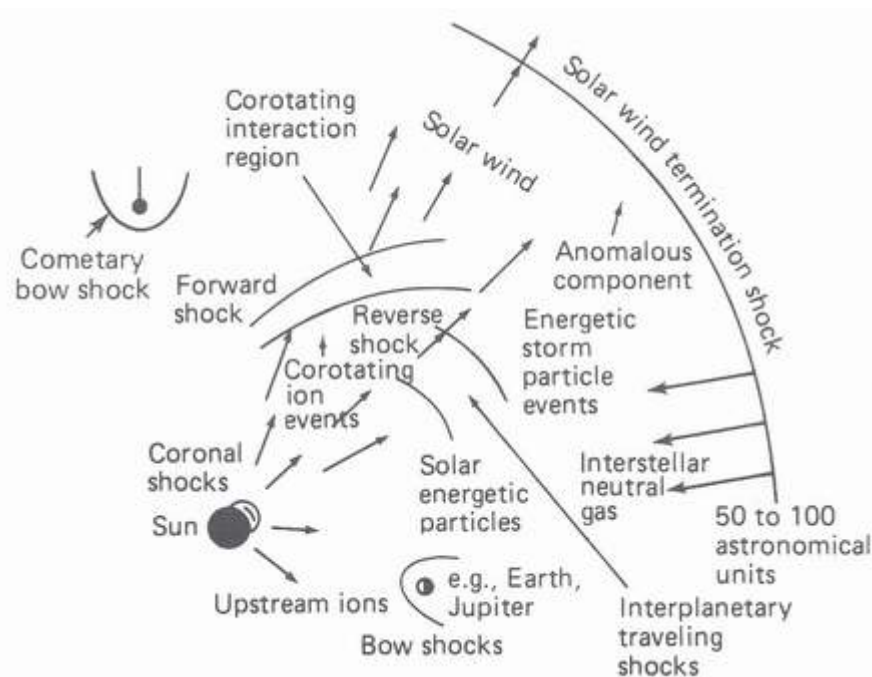
Figure 1.11. A schematic view of particle acceleration processes in the Heliosphere (adapted from Rosner et al., 1984).

1.3.1 Sources and populations

The Sun, the planets, and the vastness of the galaxy are some of the sources of the particles detected in interplanetary space. The properties of the different particle populations provide information about the acceleration mechanisms and propagation. Thus energetic particles can also be used as probes for the properties of the interplanetary medium. The classification used for the different particle populations existing in the heliosphere is based on their behavior in time, energy, direction and by the elemental and ionic composition. The most important populations in the heliosphere (see also review by Reames [1999] and chapter 9 of Kallenrode [1998]) are:

- Galactic cosmic rays (GCR): They are originated outside the solar system but generally from within our galaxy. GCRs are atomic nuclei from which all of the electrons have been stripped away during their high-speed passage through the galaxy. GCRs have been accelerated to nearly the speed of light, probably by supernova remnants. They are measured isotropically all over the solar system. The low energy portion of the distribution is modulated by the interplanetary magnetic field. The energy range spawns from 10 MeV/amu to more than 10 GeV/amu.

- Solar energetic particles (SEP): They are the result of transient processes on the Sun (or caused by it), and thus highly variable in space and time. The energies may extend up to hundreds of MeV/amu. A division into gradual and impulsive events is usually made in the context of SEP (Figure 1.12). In the former, particles are believed to be accelerated by interplanetary shocks driven by Coronal Mass Ejections (CMEs). They last days, are proton rich and the average ionization state of Fe is around 14. In the latter, the acceleration mechanism is related with flares. They last hours, are ^{3}He, electron and Fe rich with an average Fe charge state around 20.
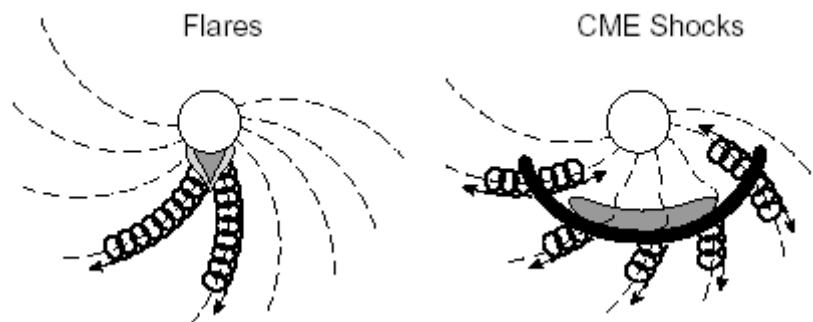
Figure 1.12: Flares and CME shocks as acceleration mechanisms for impulsive and gradual SEP events, respectively. From Reames [1999].

- Anomalous cosmic rays (ACR): They are found in the lower part of the energy spectra of GCRs (~10 MeV), but differ from them in many aspects (composition,

charge states, energy spectrum and variation with the solar cycle). The source for the ACRs is the pick-up population, originally neutral particles of interstellar origin which become ionized and are then carried out by the solar wind. The acceleration of these particles occurs at the heliospheric termination shock. The accelerated particles propagate then inwards, and are termed ACR.

- Particles accelerated at corotating interaction regions (CIR): Through the solar rotation, the fast wind coming from coronal holes and the slow wind from coronal streamers interact. The fast wind compresses and deflects the slower and denser slow wind ahead of it. In this way a region of interaction, which rotates along with the Sun, is created. In the front part of it a forward shock and in the rear part a reverse shock will eventually develop. In these shocks, particles can be accelerated up to 1-10 MeV/amu. The composition of these events correlates with the corresponding solar wind, differentiated from SEP events basically by an increased C / O ratio.

- Planetary bow shocks are also capable of accelerating particles, up to some tens of keV/amu (or up to about 10MeV/amu in the Jovian magnetosphere).

In Table 1.3, the principal characteristics of each population are described.

Type	Energy MeV/amu	Duration	Source region	Acceleration
GCR	10 - 1000	Continuous	Interstellar	?
ACR	0 - 10	Continuous	Interstellar	Shock
Gradual SEP	0.01 - 100	Days	SW	Shock
Impuls. SEP	0.01 - 100	Hours	Low corona	Flare
CIR	0.5 - 10	Days	SW	Diffusive

Table 1.3: Characteristics of the energetic particles in the Heliosphere. SW stands for solar wind. Adapted from Fränz [1994].

The composition of the energetic particles found within, and adjacent to, MCs has not been extensively studied. To which of the above populations they are associated (if any) will be analysed in Chapter 5.

Figure 1.13 shows a representation of the energy spectra of the mentioned energetic particle populations in the heliosphere. The peak at approximately 800 eV/nucleon corresponds to the slow solar wind. Higher speed streams produce a shoulder on the solar wind distribution. The suprathermal region from 10 keV/nuc to 100 keV/nuc is relatively unexplored, and the origin of the most important contributions is not yet identified. These are the first spectra to extend continuously from solar wind to cosmic ray energies. Up to 30 MeV/nucleon the contribution from anomalous and galactic cosmic rays (ACRs and GCRs) is overwhelmed by that from gradual solar energetic particle (SEP). Around 1 MeV/nuc there are contributions from impulsive solar flares and particles accelerated in corotating interaction regions (CIRs)
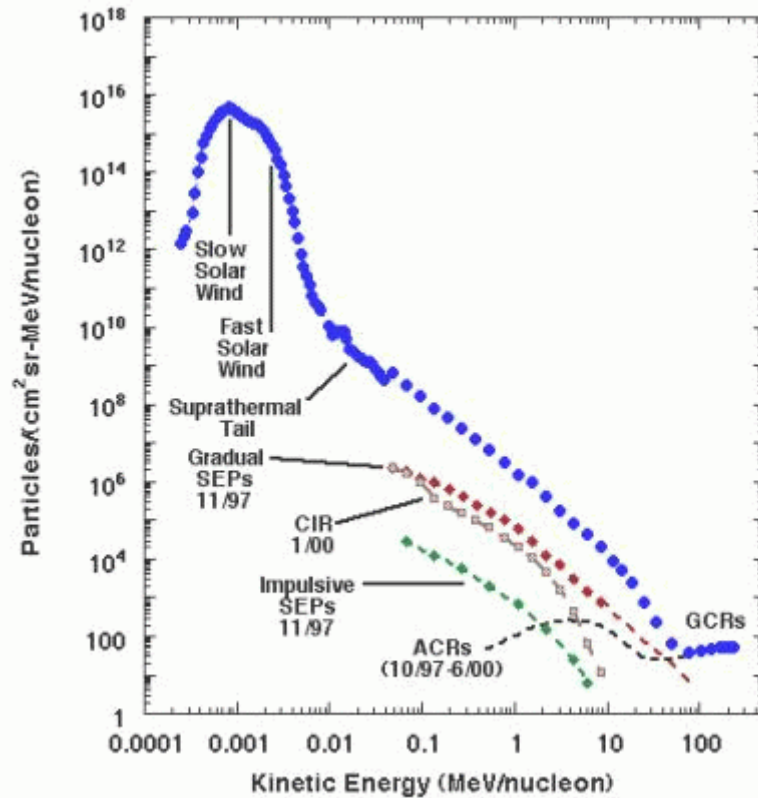
Figure 1.13. Spectra of oxygen representing the different mechanisms of particle acceleration found in the heliosphere (and beyond). Figure by Richard Mewaldt (Caltech), George Gloeckler and Glenn Mason (University of Maryland) with data from the ACE spacecraft. (http://www.srl.caltech.edu/ACE/ACENews/ACENews54.html)

1.3.2 Interplanetary shocks as a mechanism for particle acceleration

This section will describe the processes acting at shock fronts which are capable of accelerating particles to high (~MeV) energies. The literature used in this section (Kallenrode, 1998; Reuss, 1998; Stone and Tsurutani, 1985) can provide further details. Magnetic field irregularities at both sides of the shock front scatter the particles. Furthermore many particles will be reflected back and forth in these irregularities. They will travel, in this way, several times through the shock front. At the same time, there is a relative velocity between the convected scatter centers at both sides of the shock. The reflected particles will be accelerated due to the relative motion. A condition for the reflection is that the particles upstream from the shock should have a sufficiently high velocity in order for them to reach (and overtake) the shock travelling in front. This means that:

$$\mathbf{u} \cdot \cos(\theta) \cdot \cos(\theta_{Bn}) > \mathbf{V} \tag{1.2}$$

must be fulfilled.

      u   particle velocity,
      θ pitch angle,

θ_{Bn} shock normal angle (between the shock normal and the magnetic field)
V shock velocity.

If θ_{Bn} is close to 90° then this acceleration mechanism will work only for particles with a very high speed. For this reason, this mechanism is most efficient for quasi-parallel shocks ($0° < \theta_{Bn} < 45°$). This acceleration process is called Fermi acceleration or diffusive shock acceleration. The energy spectrum expected from this mechanism is a power law:

$$J(E) = J_0 \cdot E^{-\gamma} \tag{1.3}$$

J   Particle flux
γ spectral index, depends only on the ratio of the flow speeds (upstream and downstream) in the shock rest frame

For quasi-perpendicular shocks ($45° < \theta_{Bn} < 90°$), the particles are affected by the electric induction field and the acceleration process is called shock drift acceleration (SDA). In this mechanism, a charged particle drifts in the electric induction field in the shock front. In the shock rest frame this is:

$$\mathbf{E} = -(\mathbf{u}_u \times \mathbf{B}_u) = -(\mathbf{u}_d \times \mathbf{B}_d) \tag{1.4}$$

u   plasma speed in the upstream (u_u) or downstream(u_d) region

This electric field is directed along the shock front and perpendicular to both magnetic field and bulk flow. Therefore it is maximum at perpendicular shocks and vanishes for parallel shocks. The particle needs to move relative to this electric field to obtain energy and accelerate. The shock itself is a discontinuity in the magnetic field. Therefore a particle can drift along the shock front (due to gradient and curvature drifts) and perpendicular to the magnetic field and its gradient.

The average energy gain factor is lower than 5. This value is too small to account for acceleration of particles from the solar wind population (eV) up to the MeV energy range. For efficient acceleration to occur, additional scattering is needed. This scattering will feed the particles back into the shock for further acceleration. It is provided mostly by the turbulence generated by the shock itself. In other words, in order to obtain elevated energies the particles must undergo the SDA process several times.

The shock generates not only turbulence, but also waves, from which the particles can gain or loose energy. This is a stochastic process, and the acceleration method is called second Fermi acceleration or stochastic acceleration. This process is of minor importance in interplanetary shocks, compared to other processes already discussed. It is, nevertheless, important for solar flares.

1.4   Open questions and objectives

The basic picture of CMEs in the heliosphere is normally depicted by magnetic field and proton and alpha particle dynamic properties. Charge state data of heavy elements have only newly started to be used in relation to ICMEs. It will be shown here that they provide one of the best tools to identify CME material in interplanetary space. Furthermore, it will be investigated how the observations of charge states in interplanetary space relate back to what is seen at the Sun at the moment of the CME eruption. This is the only piece of in-situ data that can provide direct information of its source region. It has been suggested (Bame et al., 1979; Lepri and Zurbuchen, 2004) that a relation may exist between CME plasma and flares. They may produce the elevated charge states seen in ICMEs. Another important question related to ICME evolution is the 3-part structure seen in coronagraph images which, so far, has not been identified in in-situ data. This is mostly due to a density effect, since density is what a coronagraph basically measures. In this work it will be investigated, whether there is a possibility to detect in interplanetary space variations in CME charge state distributions corresponding to a 3-part structure. Finally, questions will be addressed, like: How do the different ions behave inside a magnetic cloud? Why do they show different profiles? How do these differences relate to the source region?

In relation to energetic particles, the analysis will be two-fold. In a first approach, the response of the energetic particle background to ICME passage will be investigated. It is important to understand whether ICMEs represent an obstacle to the normal particle propagation, or if it is favoured by them. The second step represents the analysis of the particles found within ICMEs. Where do they come from? How were they accelerated? What is the composition of these particles telling us? These are some of the questions which will be explored in this work. A further topic concerns the relation between the energetic particles and the peculiar magnetic field configuration in magnetic clouds: Are the clouds still connected to the Sun or do they propagate detached from it?

This thesis is based mainly on charge state composition data of the thermal plasma together with intensities, composition and directional information of energetic ions and electrons in the keV and MeV ranges. The data are provided by several instruments on the Ulysses spacecraft. More information on these instruments, the data and the Ulysses mission will be given in Chapter 2. Furthermore, the description is complemented with real data, in order to give a reference frame for the mission and for the heliospheric conditions as viewed by Ulysses. A complete dataset comprising the mentioned variables in conjunction with magnetic field and bulk plasma data will be used. In this way, a comprehensive view of ICME characteristics comprising different aspects provided by in-situ data will be undertaken. The picture of ICMEs in the heliosphere will be enhanced by the combination of this rich dataset. In Chapter 3, a description of the methods used to treat and combine these data will be provided. The following two chapters will be devoted to the exploration of the internal structure and characteristics of ICMEs by means of charge state distributions (Chapter 4) and energetic particles (Chapter 5). Finally, in Chapter 6 a summary and conclusions will be provided.

Chapter 2   Instrumentation

The joint ESA - NASA Ulysses mission was conceived to explore and study the three-dimensional heliosphere. It was the first spacecraft able to sample the solar wind over the poles of the Sun, up to a heliographic latitude of 80º. Its primary objectives were to investigate for the first time, as a function of heliographic latitude, the properties of the solar wind, the structure of the corona, the heliospheric magnetic field, solar radio bursts and plasma waves, solar X-rays, solar and galactic cosmic rays, and both interstellar and interplanetary neutral gas and dust. In this chapter a description of the mission will be given, its trajectory, the science payload and selected key results. The EPAC and SWICS instruments, which provided the data used in this work, will be explained in detail. Some aspects of the scientific insights procured by the Ulysses mission will also be discussed, as far as they provide the solar and interplanetary context for ICME observations

2.1 The Ulysses spacecraft

2.1.1 Trajectory, solar and heliospheric conditions

Ulysses was launched onboard the space shuttle Discovery in October 1990. To reach the out-of-ecliptic trajectory, it was sent out to Jupiter, whose immense gravity was used in 1992 to deflect the spacecraft into a highly inclined orbit (80° with respect to the ecliptic). The spacecraft reached the Sun's south pole for the first time in June 1994. Ulysses continued its orbit around the Sun, through perihelion, reaching the north pole in June 1995. The out-of-ecliptic orbit has a period of 6.2 years, approximately half of a solar cycle. In 1998 the spacecraft reached aphelion for the second time and captured again the solar wind from the south and north poles in 2000 and 2001, respectively. The third Ulysses orbit started in early 2004 with a distant Jupiter encounter, 0.8 AU farther away than at its closest approach in 1992, but nevertheless very important for Jovian science. In February 2004, ESA's Science Programme Committee unanimously

approved a proposal to continue operating the Ulysses spacecraft until March 2008. The mission has been so far a complete success. In 2007 and 2008, the European-built space probe will fly over the poles of the Sun for a third time. Figure 2.1 shows schematics of the first 2 orbits which provided the observations for this thesis.
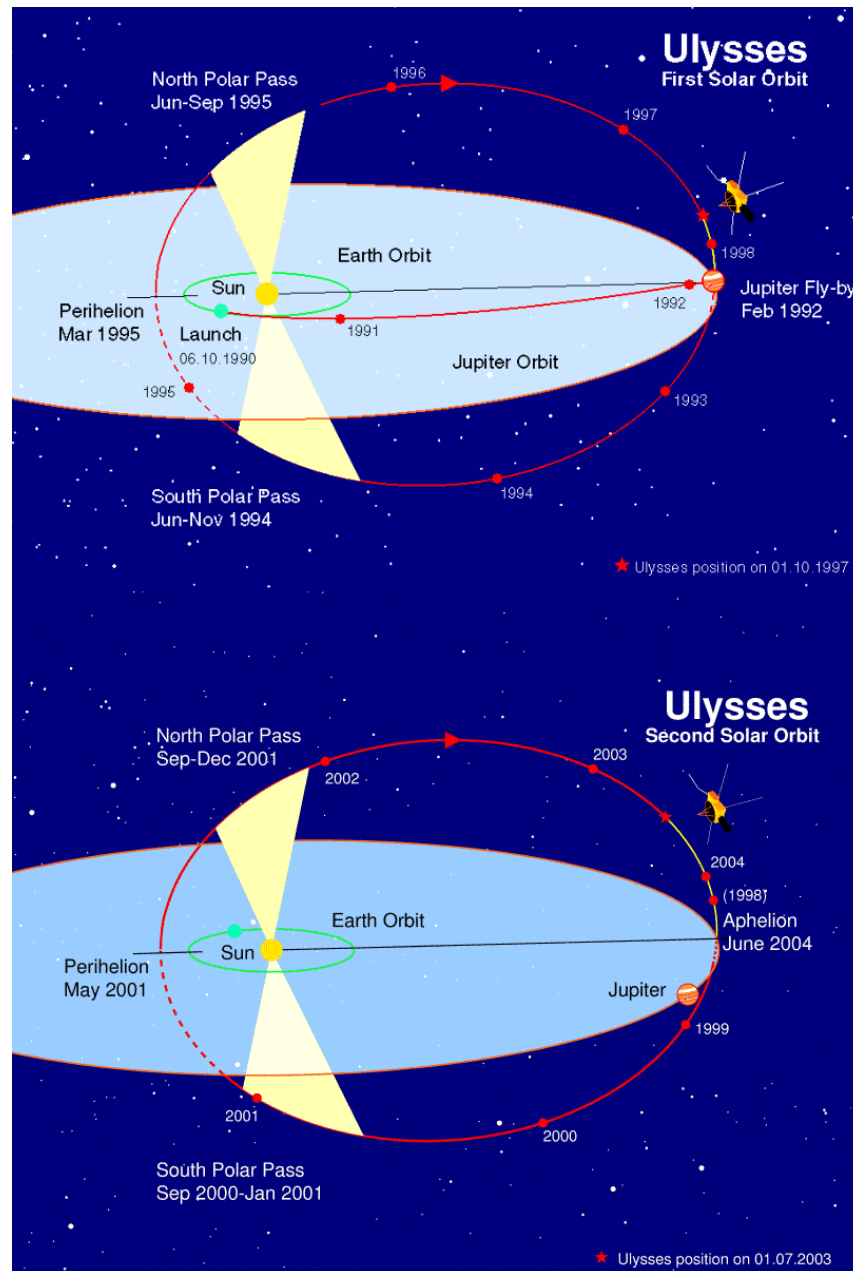
Figure 2.1. Ulysses first and second orbits around the Sun. From http://helio.estec.esa.nl/ulysses

Unlike the previous high-latitude passes in 2000 and 2001 that brought Ulysses over the solar poles near the maximum of the Sun's activity cycle, conditions for the third polar passes are expected to be much quieter. In fact, they will be similar to those in 1994 and 1995 when the spacecraft first visited the Sun's poles. However, there will be an

important difference: the Sun's magnetic polarity in 2007/2008 will be opposite to that of the previous solar minimum, due to the solar magnetic cycle. There is another difference between the solar minimum polar passes in 2007/2008 and those in 1994/1995. During its first high-latitude exploration, Ulysses did not have the benefit of being part of a fleet of solar and heliospheric spacecraft that now includes SOHO, Cluster, ACE, Wind and Cassini. The launch of new missions like the dual-spacecraft STEREO, Solar-B and Solar Dynamics Observatory, will add a further dimension to heliospheric studies over the next few years.

In Figure 2.2, key plasma and magnetic field parameters for the entire mission are plotted along with the sunspot number. The first mark in the plot represents the Jupiter fly-by in 1992, which is actually better characterized by the energetic particles as it will be shown later in this chapter. Shortly after Ulysses departed from Jupiter and immersed into southern latitudes, it started to encounter the first signs of solar wind coming from the polar coronal holes of the Sun. Alternating fast and slow wind created a region highly dominated by Corotating Interaction Regions. These CIRs characterize the transition region between slow and fast solar wind. By the end of 1993 the spacecraft was totally embedded in fast solar wind south of ~35° degrees Ulysses was entering previously unexplored regions of the heliosphere. The fast wind persisted for more than one year until equatorial regions were encountered again in 1995. From 1995 to 1998 the spacecraft sampled the northern part of the heliosphere, which showed similar (but not identical) characteristics to its southern counterpart.

In 1998 Ulysses was back at its aphelion to start the second orbit. Jupiter this time was on the opposite side of the Sun. The second orbit is remarkably different from the first one since it occurred during the maximum of the solar activity cycle. This can be noticed from the absence of typical slow and fast wind patterns. During the second half of 2001, while ascending to reach the north solar pole, Ulysses detected the formation of the northern polar coronal hole. The fast solar wind in this period was the first indication that the declining phase of the solar cycle was about to commence. CIR patterns were seen to occur again as in the first orbit, but were less marked due to the still relatively active phase of the solar cycle.
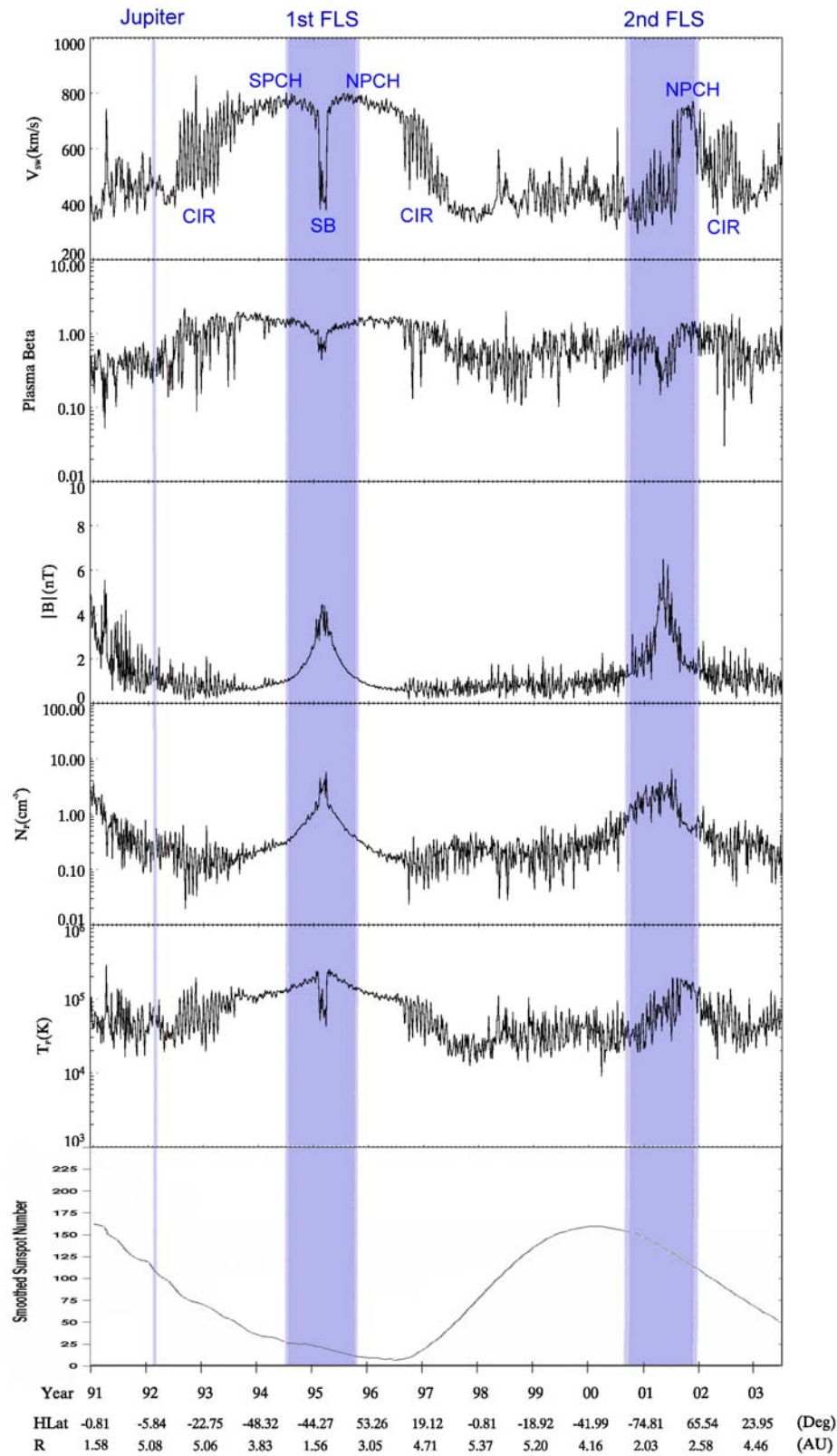
Figure 2.2. Ulysses mission plot. From top to bottom: solar wind speed, plasma beta, magnetic field magnitude, proton density, proton temperature and smoothed sunspot number. Shaded regions mark the Jupiter fly-by and the two Fast Latitude Scans (FLS) in which Ulysses traversed rapidly from southern into northern latitudes at ~1.5 AU from the Sun. Acronyms: CIR (corotating interaction region), NPCH (north polar coronal hole), SPCH (south polar coronal hole), SB (streamer belts). This plot was created for this work with data from the Ulysses magnetometer, SWOOPS and SWICS instruments, sunspot data: SIDC, Royal Observatory of Belgium.

In Figure 2.3, polar plots of solar wind speed as a function of latitude for Ulysses' first two orbits are shown. The first orbit took place during the declining phase of the solar cycle and minimum, while the second orbit encountered solar maximum conditions. This is reflected in the solar wind patterns. During solar minimum a clear differentiation is found between fast wind from the polar coronal holes and slow wind from the equatorial streamers. Noticeable on the polar representation are also the Corotating Interaction Region (CIR) patterns. They were found while Ulysses was immersed in a region of highly variable solar wind speed, at moderate latitudes during 1992-1993 and 1996. At solar maximum, the bimodal pattern has disappeared and is replaced by a mix of slow and fast wind. As it was discussed before, estimations of this behavior were already made, especially based on Helios results; the Ulysses results completed the general scenario. Important insights were gained into the heliospheric magnetic field structure, with measurements made with the Ulysses magnetometer (VHM/FGM). The polarity during the first orbit is clearly showing a definite orientation in each hemisphere (in Figure 2.3, orange and yellow colors represent outward and inward, respectively, directed magnetic fields). During solar maximum this pattern is replaced by a mixture of polarities at all latitudes. Before the second north pole pass, the polarity has reversed, as seen by the change from outward to inward directed magnetic field in the north pole coronal hole.

Ulysses provided important evidence about the relation between composition of the solar wind and its bulk properties. For example, the anticorrelation between the O^{+7}/O^{+6} ratio and the solar wind speed is shown in Figure 2.4.
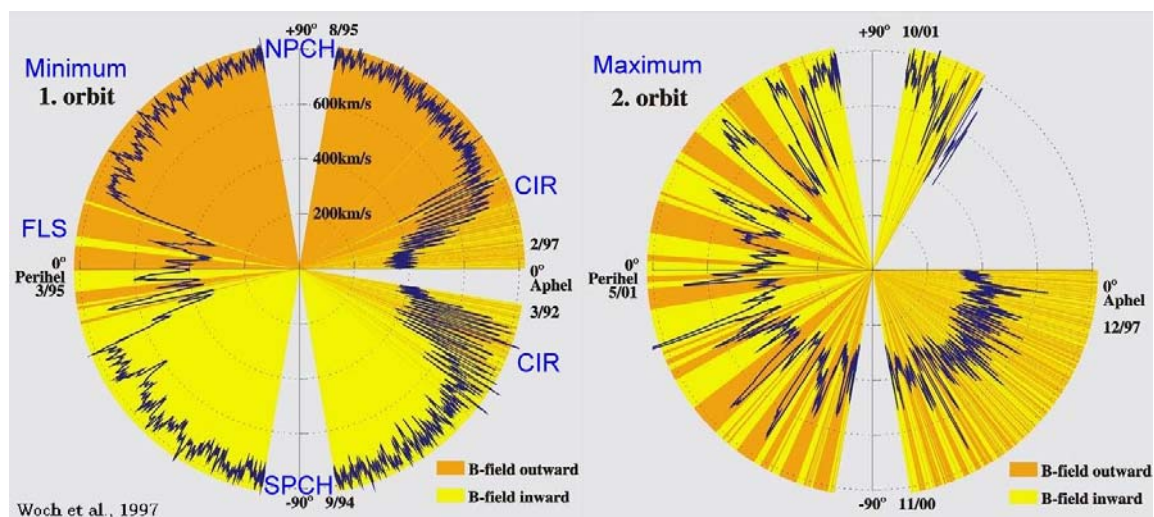
Figure 2.3. Polar plots of solar wind speed and magnetic field as a function of latitude for Ulysses' first two orbits. The difference between both orbits is remarkable, the solar wind structure changes from a 2-pattern structure during solar minimum (first orbit), to a mixture of states during solar maximum (second orbit). The magnetic field polarity during the first orbit is clearly showing a definite orientation in each hemisphere, during solar maximum this pattern is again, lost. NPCH: northern polar coronal hole, SPCH: southern polar coronal hole, FLS: fast latitudinal scan. Adapted from Woch et al. [1997].

Charge states will be extensively used throughout this work, a first approach to their importance is given here. The O^{+7}/O^{+6} ratio is displayed as its equivalent oxygen freezing-in temperature. This calculation will be described in Chapter 3. In the same figure, the ratio of the abundances of two heavy ions in the solar wind, magnesium and oxygen (Mg/O), are shown in red. They also are anticorrelated with the solar wind speed. The compositional boundaries between the two types of plasma are very sharp, much better defined than by solar wind speed.
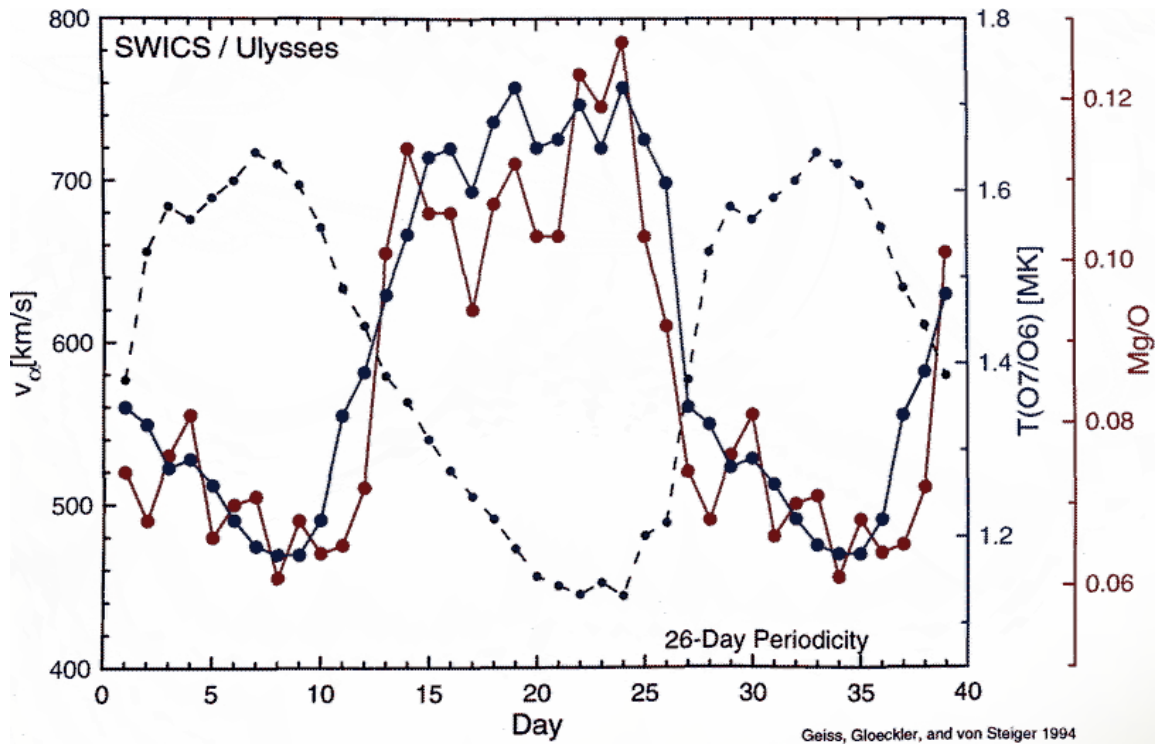
Figure 2.4. Solar wind speed, oxygen freezing-in temperature and ratio of magnesium to oxygen. Notice the anticorrelation of oxygen freezing-in temperature and Mg/O with solar wind speed. The data comprises nine solar rotations using superposed epoch method. From Geiss et al. [1994].

2.1.2 Science payload

The science payload of Ulysses is summarized in Table 2.1. A schematic diagram of the payload is shown in Figure 2.5.

Instrument	Description
COSPIN	Energetic particle spectra (ions 0.3 - 600 MeV, electrons 4 - 2000 MeV) and composition. Simpson et al. [1992].
DUST	Dust particles 10^{-16} to 10^{-6} g; mass, speed, flight direction, and electric charge. Grün et al. [1992].
EPAC	Energetic ion composition, flux, and anisotropy (ions 0.3 - 25 MeV/n, electrons above 0.1 MeV). Keppler et al. [1992].
GAS	Neutral He atom and UV detectors. Witte et al. [1992].
GWE	Gravitational Wave Experiment, Bertotti et al. [1992].
GRB	Solar and cosmic gamma ray burst detector (x-rays and gamma-rays, 15 to 150 kev). Hurley et al. [1992].
HI-SCALE	Low-Energy Particles (ions 50 to 5000 keV, electrons 30-300 keV). Lanzerotti et al. [1992].
SCE	Coronal Sounding Experiment. Bird et al. [1992].
SWICS	Solar Wind Ion Composition (thermal/suprathermal). Gloeckler et al. [1992].
SWOOPS	Solar Wind thermal ion and electron distributions. Bame et al. [1992].
URAP	Radio and Plasma Waves (plasma waves-0 to 60 kHz, radio-1 to 940 kHz, magnetic 10 to 500 Hz). Stone et al. [1992].
VHM/FGM	Vector magnetometer, 0.01 to 44000 nT, 2 vectors/second. Balogh et al. [1992].

Table 2.1. Ulysses science payload. Data in this work come from the instruments shown in blue.
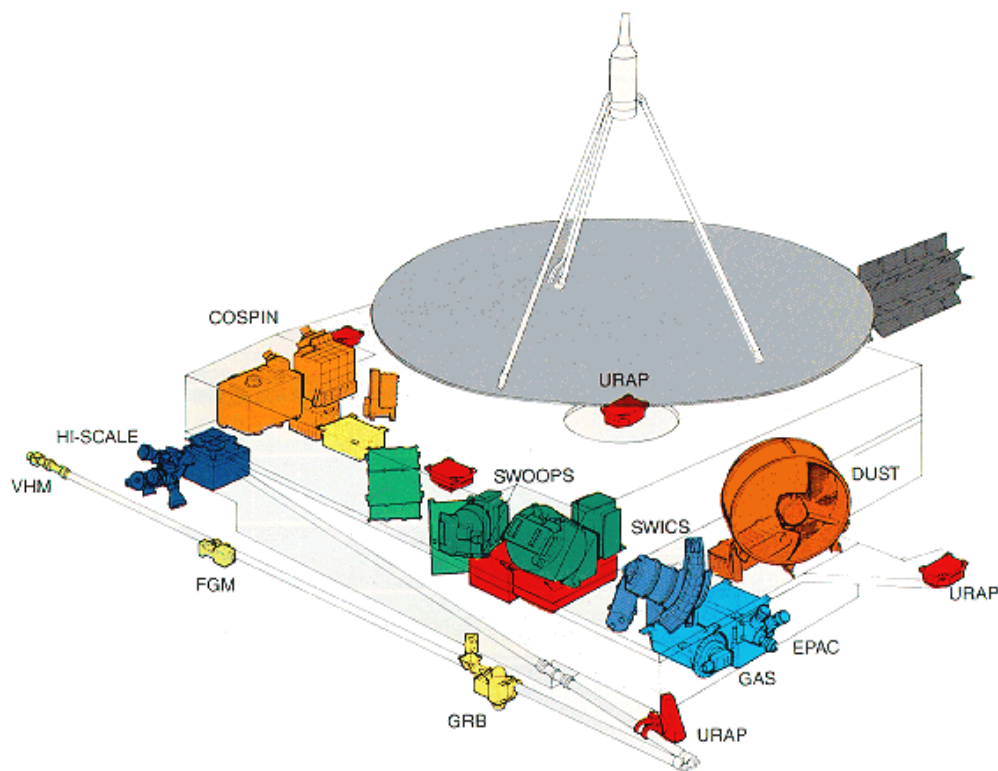
Figure 2.5. Diagram showing the scientific payload of the Ulysses spacecraft. Image from http://ulysses.jpl.nasa.gov/spacecraft/index.html.

In the following sections, the instruments which provided the data used in this work will be explained in more detail.

2.2   The Energetic Particle Composition Experiment (EPAC)

2.2.1 Design and measurement principle

The Energetic PArticles Composition instrument EPAC was designed to provide information on the flux, anisotropy and chemical composition of energetic particles with energies between 300 keV/amu and 10 MeV/amu. It comprises four telescopes, each of them with a geometric factor of about 0.08 cm²sr and a field-of-view with a full angle of 35°. The instrument is described in detail in Keppler et al. [1992]. In Figure 2.6 a sketch created to illustrate the general structure of the telescopes is shown.
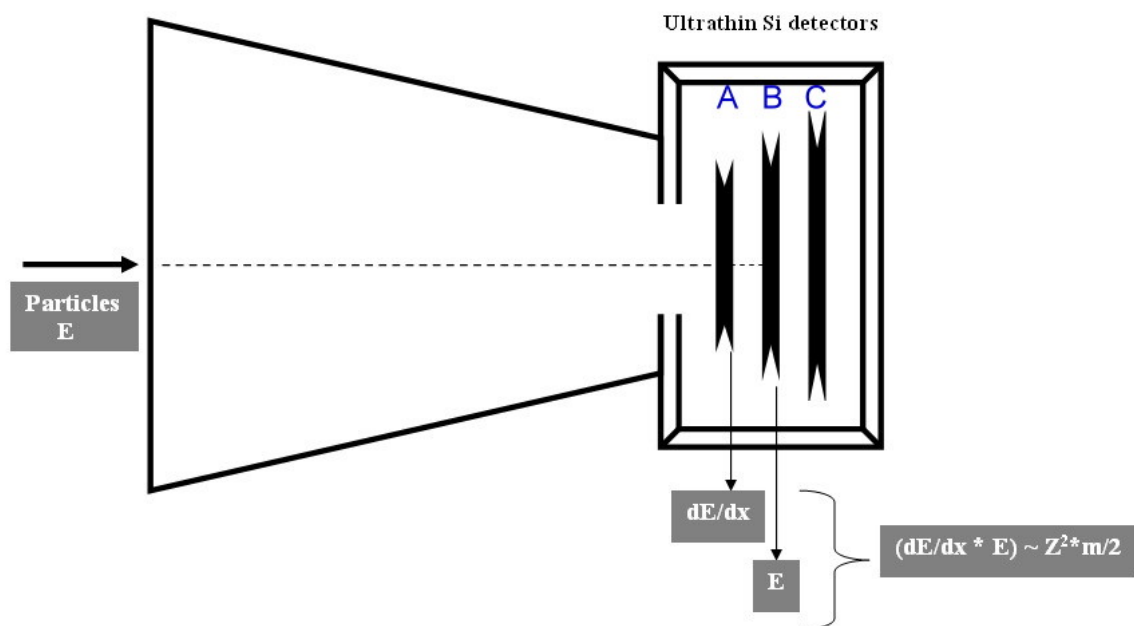
Figure 2.6. Schematics of an EPAC telescope, particles enter from the left, traverse detector A and stop in detector B. Higher energies particles go up to C. From the energy losses measured in each detector the particles can be identified.

Each of the four telescopes consists of three semiconductor detectors measuring the energy loss and total energy of incident particles. The front detector (detector A) is very

thin (5 μm), with a 25 mm² sensitive area. The energy detector B is 100 μm thick. A third detector (C) of much larger area (300 μm) provided veto signals from penetrating particles. The detector stack is surrounded by a massive platinum shield. The front detectors are protected against sunlight by 80 μg/cm² Al-layers. The telescopes based on this design allowed clear separation of hydrogen, helium and all heavier nuclei up to iron.

The "E-dE/dx" technique is used in each telescope. This technique requires a particle to traverse a very thin detector and then stop in a second, much thicker detector. Particles of higher energies traverse the first two detectors and are eliminated by a third veto detector.

The measurement principle is based on the interaction between the incoming particles and the detector itself. The energetic ions will loose energy while they penetrate the solid state detector, due to collisions with the material atoms. Energy loss due to electron collisions and due to nuclear collisions are called 'electron stopping power' S_e and 'nuclear stopping power' S_n, respectively. For the energies covered by EPAC, the energy loss that a particle would undergo could be approximated by using S_e only, in the following way:

$$S_e = -\left(\frac{dE}{dx}\right)_e = k_1 \cdot \frac{mZ^2}{E_0} \cdot f(E_0, k_2) \tag{2.1}$$

      m   particle mass,
      Z   particle atomic number,
      E_0 particle energy
      k_1, k_2 constants depending on the detector's material.

In this way, the energy loss of the incoming particle is a function of the particle energy, mass and atomic number. The thickness of the detectors determines the energy and mass range of the telescope. Due to the low mass of electrons, their energy loss is much smaller than that from the ions. Therefore ions and electrons can be differentiated.

In Figure 2.7, the energy loss in the front detector A is shown for different ions, compared with the particle incident energy E_0.

In a first approximation, the energy loss grows linearly with increasing particle energy. At very low energies, a deviation from this behavior occurs, due to the influence of nuclear collisions. There is a maximum in the curve for each ion (pinch-through energy), beyond it the energy loss decreases with increasing energy. For energies above the pinch-through energy, the particle is not stopped by the detector anymore, the particle penetrates the front detector and reaches the second. Beyond this threshold value, the energy loss used in Equation 2.1 can be obtained.
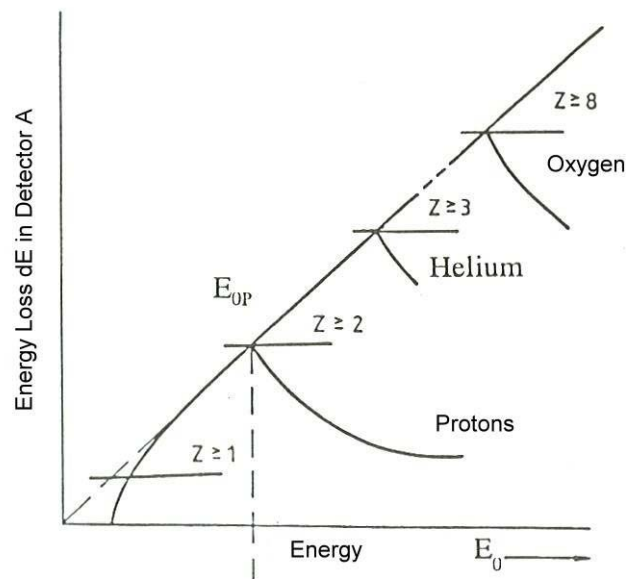
Figure 2.7. Schematic display of the energy loss curves in front detector A, for different ions. E_{0P} demarks the pinch through energy for protons.

The use of a second detector, thick enough to stop the particles penetrating the first detector, provides a measurement of the rest energy E. From the dE and E signals, the energy $E_0 = E + dE$ and the factor mZ^2 of the incoming particle can be determined. This is the principle (along with a third veto detector) that the EPAC instrument applies to identify particles. Each particle identified in this way represents one count in the EPAC measurement matrix (shown in Figure 2.8). In reality, the transmission bandwidth of 16 bit/s imposes limitations on data transmission to Earth. Therefore not every ion hitting the detectors can be directly counted. There are classification schemes onboard, which integrate the data in different categories in order to minimize the transmission size. As can be seen in Figure 2.8, plotting events in the way described generates a plot of the energy loss in the front detector A vs. the rest energy in the second detector B. The counts are aligned along tracks, and each track corresponds to one element. It is worth noticing that EPAC provides no information on the charge states of the incoming particles. The jump in the matrix (defined as the 512 x 256 array which contains the measured points) seen around B channel 256 is due to a division in low and high range to obtain higher resolution at lower energies.
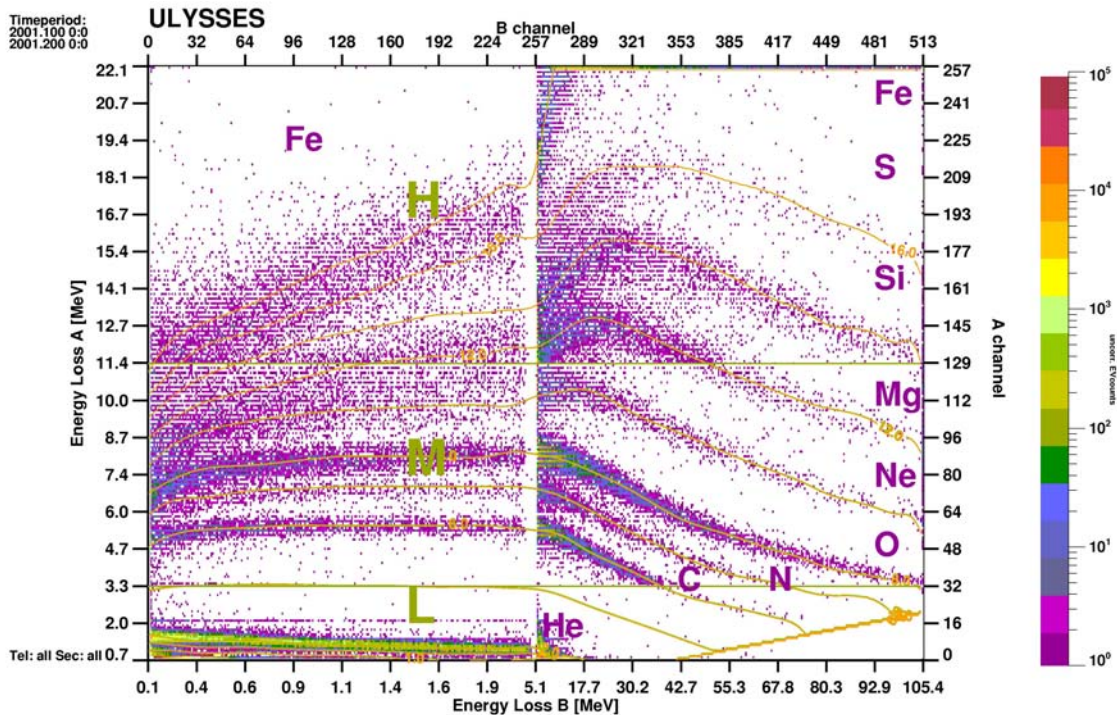
Figure 2.8. Energy loss in front detector A vs. rest energy in detector B. Each point represents a count, the ions accommodate themselves along curves which allows their identification. H, M and L represents the High, Medium and Low (respectively) divisions in the EPAC matrix. This data was accumulated during 2001, when Ulysses crossed the solar equator at 1.3 AU.

2.2.2 Directional information

The EPAC instrument comprises four identical telescopes, a diagram is shown in Figure 2.9. The telescopes are inclined at angles of 22.5°, 67.5°, 112.5° and 157.5°, with respect to the spacecraft spin axis (which points towards Earth).
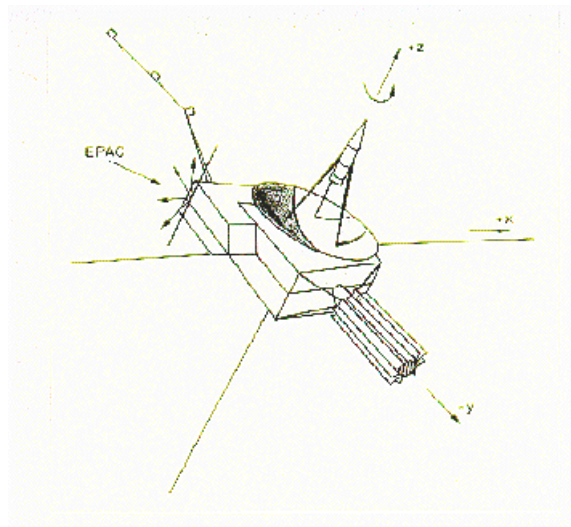
Figure 2.9. Position and orientation of the 4 EPAC telescopes (arrows). The spacecraft spin axis (Z) points towards Earth.

For certain data types (see next section) the spacecraft spin separates the EPAC data in spatial sectors defined by the orientation of the telescopes at a given time during the rotation. Telescopes, sectors, and the spacecraft spin, allow EPAC to sample 80% of the unit sphere.

2.2.3 Data and calibration

The different categories of data which are transmitted to the ground, using different time and angular resolutions are summarized in Table 2.2. The data comprises ions (from H through Fe) and electrons.

Ion	Category	Tel.	Sect.	E [MeV/amu]	Ch.	Cadence
Protons	PS	1-4	8	0.5-1.5	8	17 min
	PR	2,3	8	0.5-1.5	1	512 s
	OP	1-4	1	0.5-1.5	1	128 s
Ions Z ≥ 1	ZS	1-4	8	0.2-0.5	8	17 min
	ZR	2,3	8	0.2-0.5	1	512 s
	OZ	1	4	0.2-0.5	1	128 s
	OZ	2,3,4	1	0.2-0.5	1	64 s
Electrons	ELL	1-4	1	0.10-0.38	1	128 s
	ELH	1-4	1	≥ 0.18	1	128 s
Helium	HSS1	1-4	1-4	0.5-4.0	5	34 min
	HRS1	1-4	1	0.5-4.0	1	512 sec
CNO	HSS2	1-4	1-4	0.5-7.0	8	34 min
	HRS2	1-4	1	0.5-7.0	1	512 sec
Sulfur	HSS3	1-4	1-4	0.5-10.0	8	34 min
	HRS3	1-4	1	0.5-10.0	1	512 sec
Iron	HSS4	1-4	1-4	0.7-10.0	8	34 min
	HSS4	1-4	1	0.7-10.0	1	512 sec
He-Fe	ER	-	1	0.7-10.0	3	256 sec
Background	BRA	1-4	1	-	-	1024 sec
	BRB	1-4	1	-	-	1024 sec
	BRC	1-4	1	-	-	1024 sec
Single events	EV	1-4	4	0.5-8.0	256	32/256 sec

Table 2.2. Data categories available from the EPAC instrument. Adapted from Fränz [1994].

The different categories are separated according to their directional information, accumulation time, energy channels and other criteria defined in detail in the instrument

description by Keppler et al. [1989].

In this work the most used categories are:

- PS: Proton data, directional information.
- ELL and ELH: Electron data, channels low and high, available for 4 telescopes, no sector information.
- HS: Heavy ion data, available for 4 telescopes with directional information.
- ER: Divided in ERL (p, He), ERM (C, N, O) and ERH (Fe), contains the data corresponding to the 3 divisions in the EPAC matrix (Figure 2.8).
- EV: Direct events. This category takes directly each point (up to 32 events can be registered per data frame, due to telemetry restrictions) from the EPAC matrix, whithout further classification. Therefore it is very well suited for abundance analysis.

The tracks defined for each element in the energy loss vs. rest energy matrix varies with time. Aging of the detector, temperature variations, etc., causes the response of the detectors to shift. In order to avoid misidentification of ions, the tracks have to be calibrated regularly. There are 4 calibrations so far:

0: 1990-1992 Pre-Jupiter
1: 1992-1996 Post-Jupiter
2: 1996-2001 Post-First Fast Latitudinal Scan
3: 2001-present Post-Second Fast Latitudinal Scan

In Figure 2.10, a mission-long plot was created to show the measured intensities for helium, oxygen, protons and electrons in selected EPAC channels; in a similar manner to Figure 2.2. The Jupiter fly-by in early 1992 is clearly seen in the particle fluxes, especially in the electrons. In protons and helium, the particles accelerated by CIRs in 1993 and (to a smaller extent) in 1997 appear and provide the energetic particle fluxes with a marked structure, which resembles that of the solar wind speed. The highest fluxes are seen (except those corresponding to transient events) during solar maximum and mostly when Ulysses was immersed in slow wind streams.

Energetic particle data from EPAC are a valuable tool for discerning the structure of the magnetic field in interplanetary space. Particles of the energy range detected by the instrument can be used as tracers to discern properties of the magnetic configuration under study. Furthermore, the composition of the energetic particle population determined by EPAC measurements represents a proxy of the acceleration mechanism. Particle fluxes, composition and directional information will be analyzed in this work, in relation to Interplanetary Coronal Mass Ejections (ICMEs).
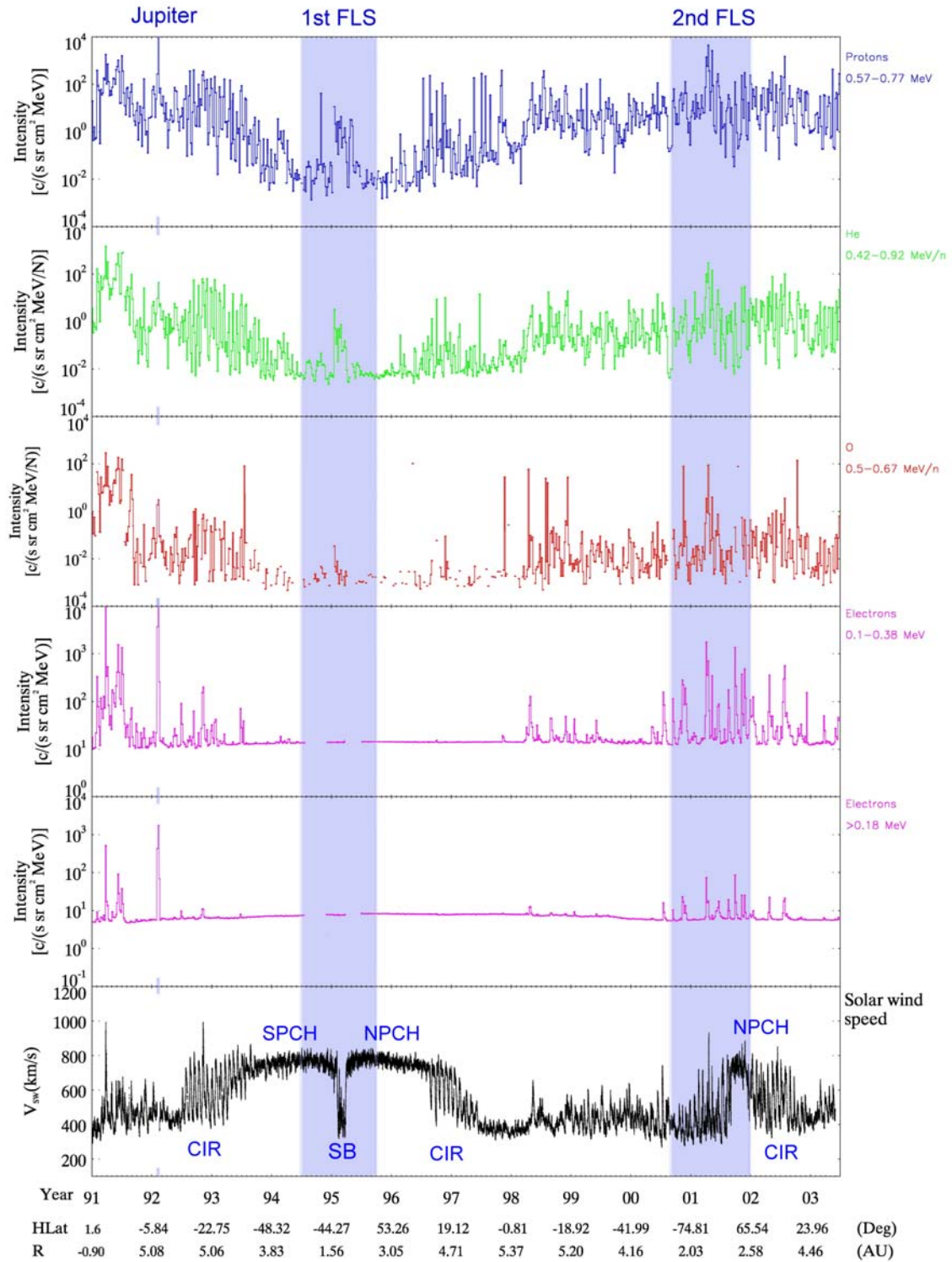
Figure 2.10. Mission plot showing EPAC data. From top to bottom the panels display protons, helium, oxygen and two electron channels. The last panel shows the solar wind speed from SWICS. The shaded blue area, marking the Jupiter encounter, has been partially deleted to allow a better observation of the energetic particles' peaks. Acronyms: CIR (corotating interaction region), NPCH (north polar coronal hole), SPCH (south polar coronal hole), SB (streamer belts).

2.3 The Solar Wind Ion Composition Spectrometer (SWICS)

The density, level of ionization, temperature and velocity of ions in the solar wind can be determined with the SWICS instrument on Ulysses. It measures elements from hydrogen to iron, in an energy range from 0.16 keV/e to 59.6 keV/e. Due to the combination of an electrostatic analyzer and a time-of-flight sensor with solid state detectors it is possible to determine the mass, charge and energy of ions. The instrument is particularly good to measure the density and level of ionization of tracer elements in the solar wind. It is described in detail by Gloeckler et al. [1992].

2.3.1 Design and measurement principle

The SWICS sensor uses a combination of electrostatic deflection, post-acceleration, time-of-flight (TOF) and energy measurement, to obtain the energy, mass and charge of solar wind ions. Figure 2.11 shows the principle of operation of the SWICS sensor and illustrates the function of the 5 basic sensor elements:

Ions of kinetic energy E, mass M and charge (ionization) state q enter the sensor through a large area, multi-slit collimator that selects proper entrance trajectories of the particles. The electrostatic deflection analyzer serves both as a UV trap and as an energy per charge (E/q) filter, allowing only ions within a given energy per charge interval, determined by a stepped deflection voltage, to enter the time-of-flight vs. energy system. TOF and residual energy measurements are required for determining the mass and charge state of an ion population. Since solid state detectors typically have a 25 to 35 keV energy threshold, ions are post-accelerated by 30 kV just before entering the TOF vs. energy system.

In the TOF system the speed of each ion is determined by measuring the travel time of the particle between the start and stop detectors separated by a distance of 10 cm. The particle identification is completed by measuring the residual energy of the ions in a conventional solid state detector.

From the measurements of the TOF, the residual energy and E/q of the incoming ion, the mass (m), charge state (q) and energy (E) of the ion can be determined (Joos, 1989):

$$m = 2\left(\frac{\tau}{d}\right)^2 \frac{E_{res}}{\alpha} \tag{2.2}$$

$$q = \frac{E_{res}/\alpha}{U_B + E'/q} \cong \frac{E_{res}/\alpha}{U_B} \tag{2.3}$$

$$E = q[E/q] \tag{2.4}$$

d: length of the TOF part
E'/q: small energy loss in the thin foil of the start-time detector (Ipavich et al., 1982)
[E/q]:   E/q obtained from the electrostatic deflection analyzer
U_B: Post-acceleration potential
α: nuclear defect in solid-state detectors (<1, Ipavich et al., 1978).
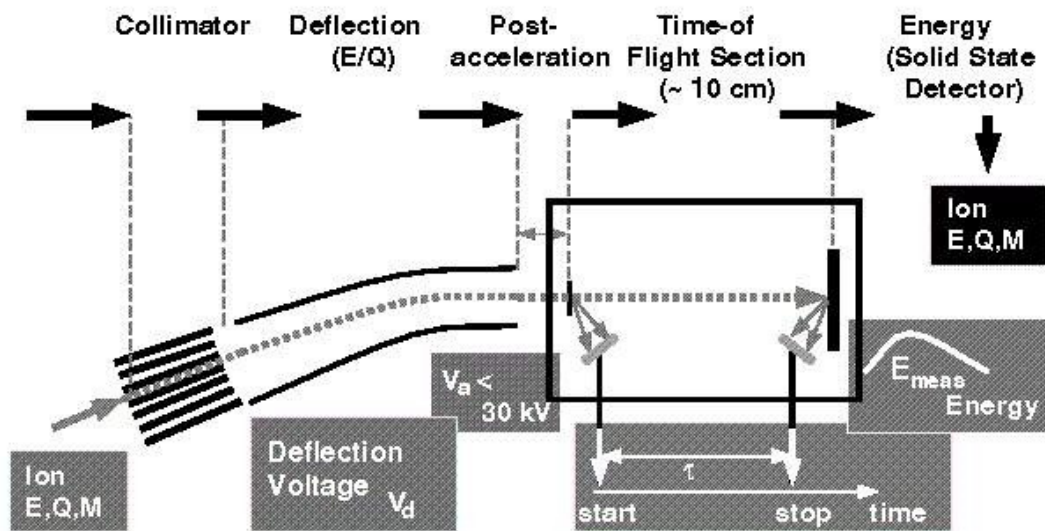
Figure 2.11. Schematic of the measurement technique used by SWICS, showing the functions of each of the five basic elements. From Gloeckler et al. [1992].

The instrument is composed by a principal and a secondary channel. The latter does not possess a TOF instrument and it is designed to work with protons only. Protons are excluded from the principal channel, to prevent saturation. Figure 2.12 shows a SWICS cross-section, where these two channels can be seen. Data are transmitted to the DPU or Digital Processing Unit, which has two basic functions:

- It controls the instrument: Work modes, voltages and general electronics.
- It controls the dataflow: Data format, selection, modes, reduction, compression and transmission.

2.3.2 Data

From the Equations 2.2 and 2.3, the values of m and m/q can be derived. These data are stored in the instrument matrix and transmitted after one instrument cycle, or 768 seconds (maximum resolution). Figure 2.13 shows a typical SWICS m vs. m/q matrix. With these data, mass and charge state distribution within a solar wind parcel can be evaluated.
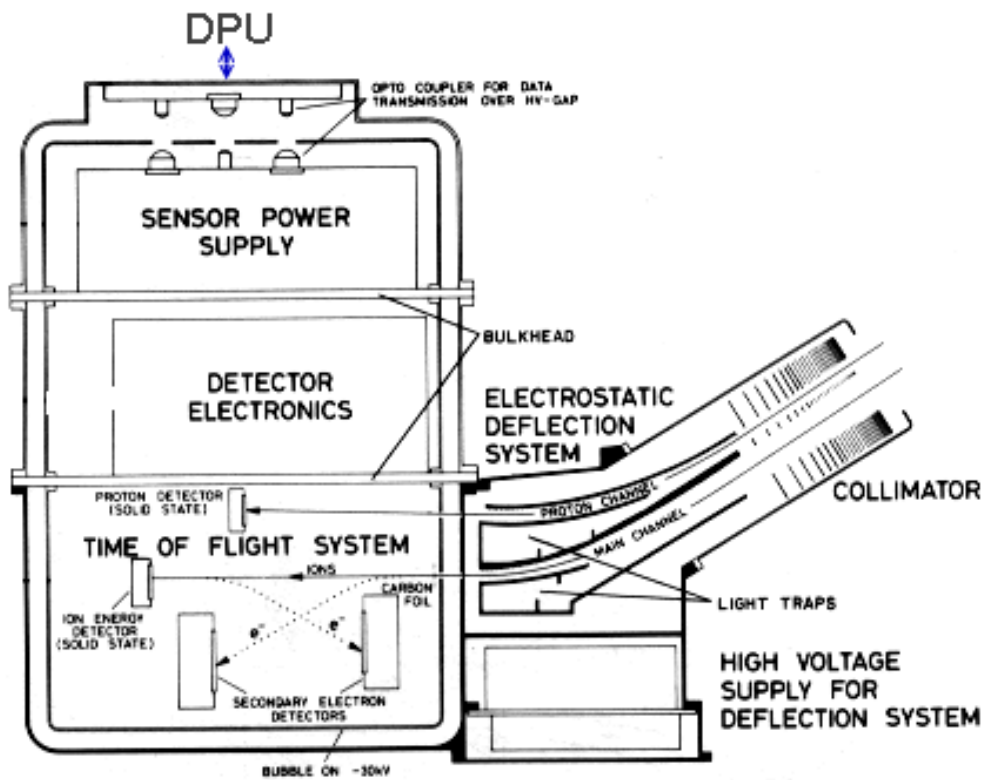
Figure 2.12. Cross-section of the SWICS instrument showing the collimator, the two-channel deflection system and its deflection power supply, the time-of-flight system, analog electronics, power supply and opto-couplers for digital data transmission. Adapted From Gloeckler et al. [1992].
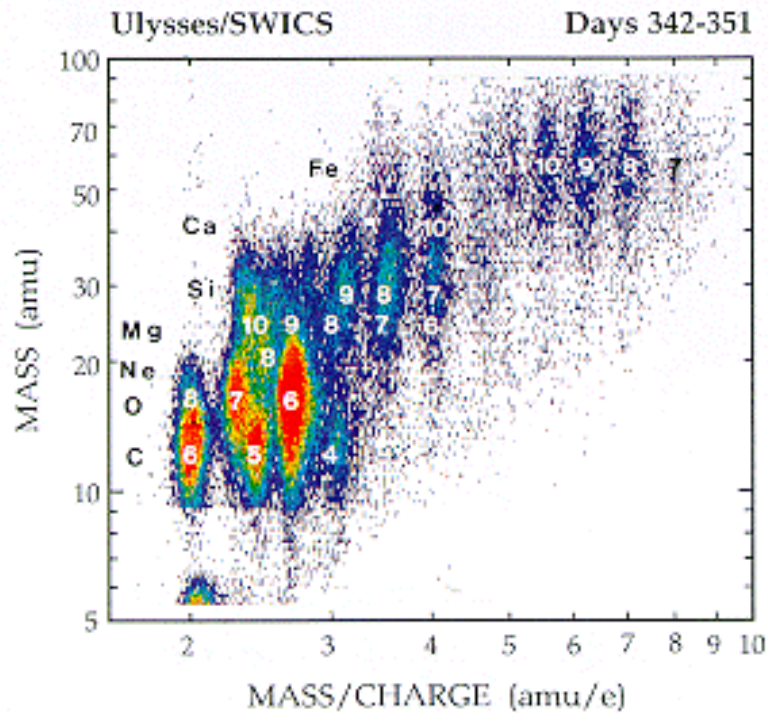
Figure 2.13. Ions detected by SWICS are plotted according to their mass and mass per charge. The color coding represents the number of measurements. From Gloeckler et al. [1992].

For this work, data from the Ulysses data system (UDS) available at http://helio.estec.esa.nl/ulysses/data_archive.html are used. These data are 3-hour averages. In Figure 2.14 a plot with the most relevant SWICS data products covering the Ulysses mission up to 2003 is displayed, using the same structure as that from Figure 2.2 and Figure 2.10. Most striking on this global scale is the anticorrelation between solar wind speed and the ionic ratios. A comparison between charge states and solar wind speed in the period of time during, and surrounding, the 1st FLS (Fast Latitudinal Scan) would clearly illustrate this anticorrelation. Charge states of solar wind ions represent a very valuable tool for identifying and characterizing different solar wind streams. This issue will be studied further in the following chapters.

SWICS data, especially the ionization levels of the different elements can be used to infer properties of the source region on the Sun from which ICMEs originate. Charge states are the only piece of in-situ data which can do so. The relation between ICMEs and charge states will be studied in depth in the following chapters.
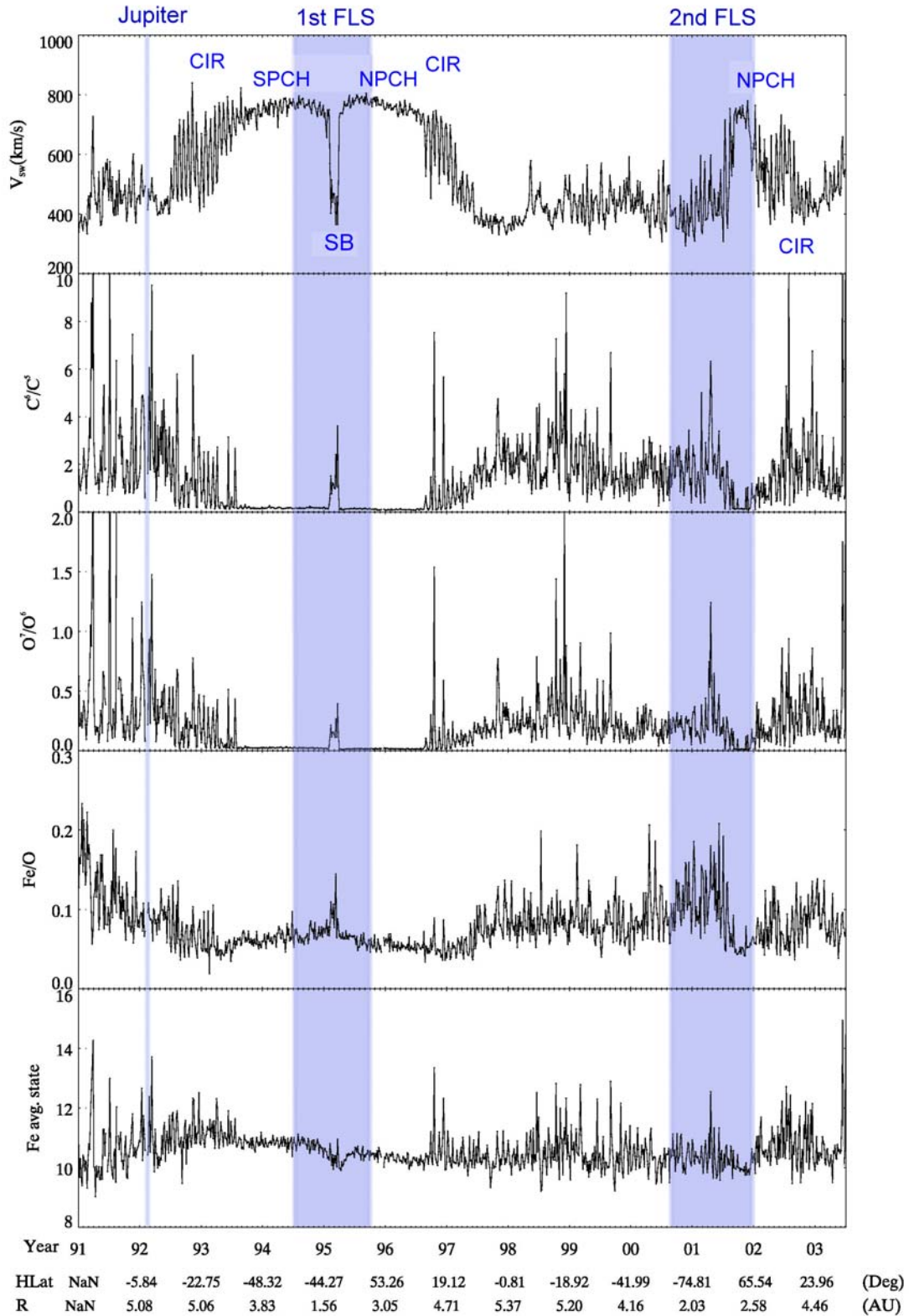
Figure 2.14. Mission plot with SWICS data. From top to bottom the panels represent: solar wind speed, ratio of C^{+6}/C^{+5}, ratio of O^{+7}/O^{+6}, iron to oxygen ratio and the average charge state of iron. Acronyms are the same used in Figure 2.10.

2.4   Other instruments

2.4.1 The Ulysses magnetometer (VHM/FGM)

The magnetometer experiment onboard Ulysses uses two sensors, a Vector Helium Magnetometer (VHM) and a Fluxgate Magnetometer (FGM). Onboard data-processing yields measurements of the magnetic field vector with a time resolution up to 2 vectors/second and a sensitivity of about 10 pT. The instrument is fully described in Balogh et al. [1992].

For this work, 1-hour averaged data of the magnetic field vector components are used. The data are accessible via the Ulysses data system at http://helio.estec.esa.nl/ulysses/data_archive.html. The magnetic field data in this thesis are given in the RTN system. This system is centered at the spacecraft and oriented with respect to the line connecting the Sun and the spacecraft. The R (radial) axis is directed radially away from the Sun through the spacecraft. The T (tangential) axis is the cross product of the Sun's spin vector (North directed) and the R axis, i.e., the T axis is parallel to the solar equatorial plane and is positive in the direction of planetary rotation around the Sun. The N (north) axis completes the right handed set.

The magnetic field data are of vital importance for the evaluation of CMEs in interplanetary space. Magnetic clouds are basically defined by these data.

2.4.2 The Ulysses Solar Wind Plasma Experiment (SWOOPS)

SWOOPS stands for "Solar Wind Observations Over the Poles of the Sun". The instrument consists of an ion spectrometer and an electron spectrometer. The ion spectrometer measures the positive ions and the electron spectrometer measures the free electrons within the solar wind. It allows the determination of temperature, density and higher order moments of the solar wind populations. Ions are detected between 255 eV/q and 34.4 keV/q, while electrons with central energies extending from 0.86 eV to 814 eV can be measured. The instrument is explained in detail in Bame et al. [1992].

For this work, 1-hour averaged data of densities and temperatures of protons, electrons and alpha particles are used. These data provide information on the state of the plasma, needed to properly characterize and differentiate solar wind parcels.

Chapter 3 Data analysis and methods

This chapter presents a description of the principal tools used in this thesis for data analysis. Starting point is the procedure for identifying and selecting the events which will be analysed further. Previously available ICME lists, eye inspection and Minimum Variance Analysis (MVA) were used as tools for the selection process. To characterize the ICMEs, various physical quantities were derived from the EPAC and SWICS data. Ratios of different solar wind ionic species were transformed into freezing-in temperatures. High-energy particles were treated by means of their intensities, composition and their incident direction. Finally, a description of the magnetic field model used for magnetic clouds will be given.

3.1 Event selection

The starting point was the Ulysses Interplanetary Coronal Mass Ejections (ICMEs) list maintained by the SWOOPS team on their webpage (http://swoops.lanl.gov/cme_list.html, henceforth called Ulysses ICME list). The events in this list had been selected by the SWOOPS team based on plasma (especially bidirectional electrons) and magnetic field measurements. The list contains 147 cases for the period considered in this study, February 1992 to August 2002.

All the events from the list were analysed, in order to identify magnetic clouds (MCs) and create the database used in this thesis. As explained in Section 1.3.3, an ICME can be considered to be a MC, when it shows a smooth rotation in **B** with low variance, low proton temperature and low plasma beta. This classification criterion was followed in this thesis.

To illustrate the differences between cloud (MC) and non-cloud ICMEs (as defined by the signatures listed in Section 1.2.2), an example of each is shown in Figure 3.1. The figure displays time profiles of relevant magnetic field and solar wind parameters. The

first event in the selected interval is a MC, while the second is not. The MC was observed at the location of Ulysses between day 283 and day 288 in 1998, at an approximate heliocentric distance of 5.3AU and at a heliographic latitude of -15°. The non-cloud ICME was observed one day later. Dashed vertical lines represent the start and end times taken from the ICME list. The shaded region contains the MC, as analysed in this work. The reason that the boundaries do not coincide will be explained in the next section.

During the cloud interval, the signatures previously mentioned are present. The MC does not drive a shock, even though there is one present between the cloud and the non-cloud ICME. The proton temperature and the plasma beta drop significantly within the MC. This low kinetic proton temperature and the difference in velocity between the rear and front part indicates a possible expansion of the magnetic cloud. The magnetic pressure is high compared to the gas pressure, clearly reflected in the low values of plasma beta.
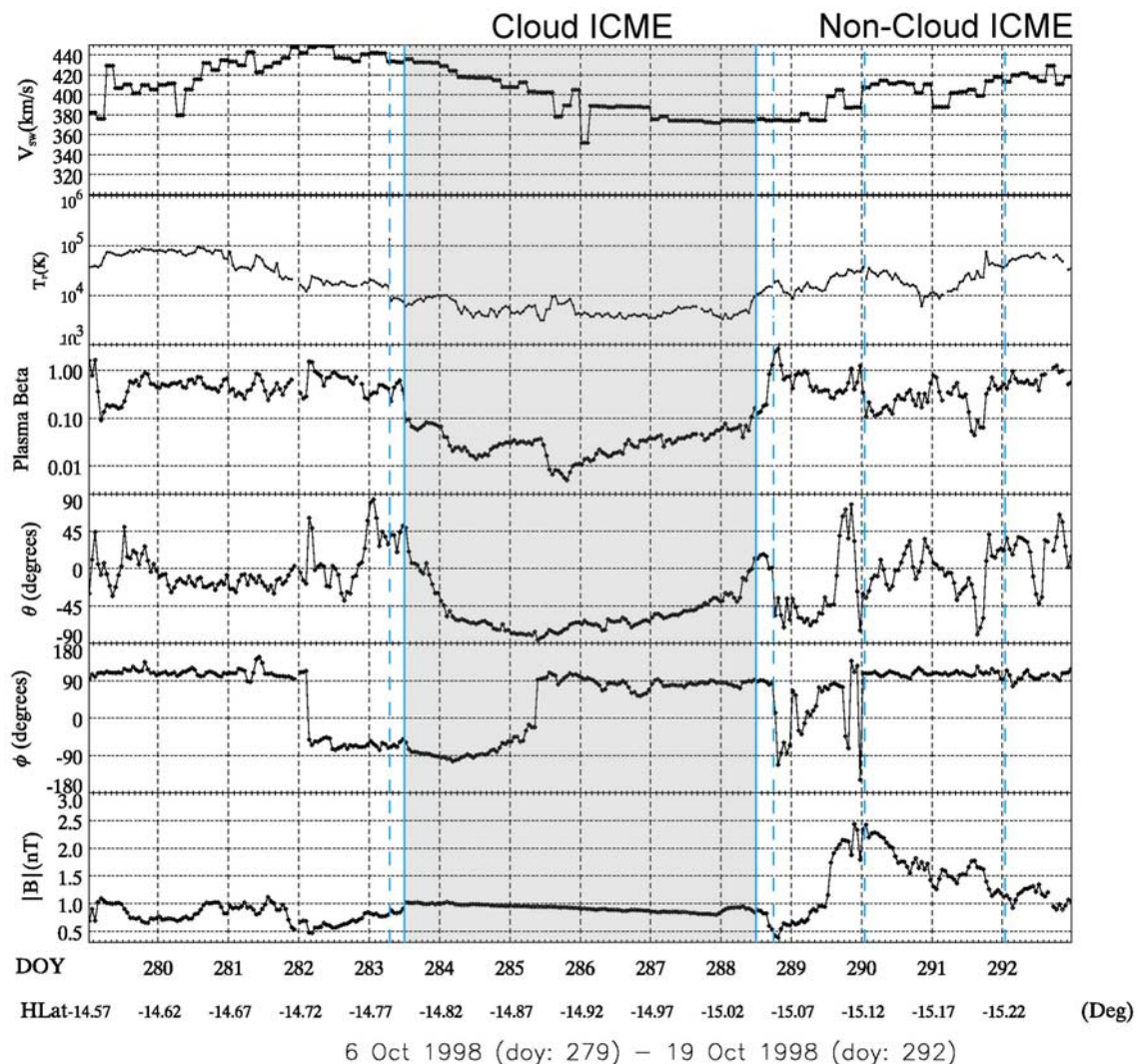
Figure 3.1. A cloud ICME and a non-cloud ICME encountered by Ulysses at 5.3 AU and 15° southern heliographic latitude. From top to bottom the panels show: solar wind speed, proton temperature, plasma beta, magnetic field elevation (θ) and azimuthal angle (Φ), magnetic field intensity. Adapted from Rodriguez et al. [2004].

The magnetic field configuration is quite particular. As it was described in Section 2.4.1, the magnetic field data are displayed in the RTN system. The rotation that the magnetic field vector describes in the NT plane can be sketched as follows:
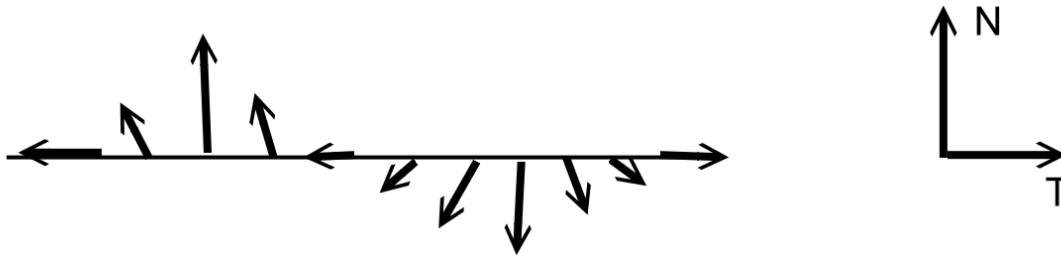
Shortly before the cloud arrival, the magnetic field points in the negative T direction and starts to rise towards high θ values. After reaching 90°, the N component diminishes and the vector moves back to low θ values, retaining the same orientation in T. After it reaches 0° in elevation, the N component turns negative and continues decreasing until it gets to -90° where it immediately commences to move towards positive elevation angles. At this point, the orientation in the T direction reverses to 90°.

The second event on Figure 3.1 (day 290 to day 292) does not follow the MC identification criteria. Even though the proton temperature and the plasma beta are locally decreased, there is no rotation discernable in the magnetic field data. A shock precedes the structure; this can be identified by the prompt increases in the magnetic field magnitude and the solar wind speed during day 289.

Table 3.1 contains the dates and some parameters of the MC events selected for this thesis. Based on the criteria described above, 40 events were classified as MCs. It represents 27% of all the ICMEs analyzed, a similar ratio to the one obtained by Gosling [1990] for the MCs to ICMEs ratio at 1 AU. It is worth noticing that the determination of the boundaries was done following a conservative approach, doubtful parts of the event were left out.

Figure 3.2 was created to provide a view of the distribution of events found throughout the Ulysses mission, ordered by latitude of detection. It is difficult to obtain a real dependence with latitude, since the latitude coverage of Ulysses is biased by the solar cycle.

YYDOY-HH	YYDOY-HH	Hel.Lat.	R	Vel.
92198-16	92201-12	−14	5.32	442.7
92319-09	92322-17	−20.3	5.2	608.9
93161-04	93163-02	−32.4	4.641	758.6
94041-01	94041-23	−52.4	3.623	747
95034-13	95035-04	−22.2	1.402	764.6
96290-03	96292-12	24.2	4.457	639.6
96345-12	96346-00	20.5	4.642	604
96347-22	96348-11	20.3	4.65	497.7
97010-07	97011-01	18.5	4.738	468.7
97147-00	97148-00	10.5	5.079	437.7
97227-17	97231-05	6.1	5.224	362
97242-04	97243-09	5.4	5.244	398.4
97317-11	97319-06	1.5	5.333	392.7
98025-17	98026-02	−2	5.385	386.1
98086-02	98087-01	−5	5.404	375.9
98100-16	98101-10	−5.7	5.405	408.1
98226-23	98227-12	−11.9	5.362	446.1
98238-05	98239-10	−12.5	5.353	399.6
98241-00	98241-20	−12.6	5.351	389.4
98251-04	98252-03	−13.1	5.342	380.9
98261-07	98262-06	−13.6	5.333	371
98283-12	98288-12	−14.8	5.308	395.7
98312-20	98313-08	−16.2	5.276	426.7
98314-04	98315-01	−16.3	5.274	414.8
99063-13	99064-06	−22.3	5.087	452.4
99166-19	99167-22	−28.2	4.843	426.8
99229-00	99229-13	−32.1	4.661	420.1
00091-13	00092-06	−50.1	3.74	408.3
00197-00	00198-01	−62.4	3.2	529.5
00223-12	00224-14	−66.1	2.998	476.8
00341-14	00342-15	−79.6	2.204	406
01101-06	01102-00	−25.9	1.422	614.1
01188-00	01188-15	39.8	1.432	293
01204-11	01205-05	50.5	1.507	395
01236-13	01237-00	67.6	1.691	524
01318-13	01319-10	75.4	2.258	624.2
02043-05	02043-19	57.8	2.866	511.5
02125-07	02126-06	46	3.363	375.6
02165-17	02169-10	41.2	3.591	650.4
02199-04	02199-14	37.9	3.754	529.3

Table 3.1. Magnetic clouds detected in the Ulysses data from February 1992 to August 2002. First column shows the starting date, the second one corresponds to the end date. The next columns represent the average heliographic latitude, distance from the Sun and solar wind speed. Adapted from Rodriguez et al. [2004].
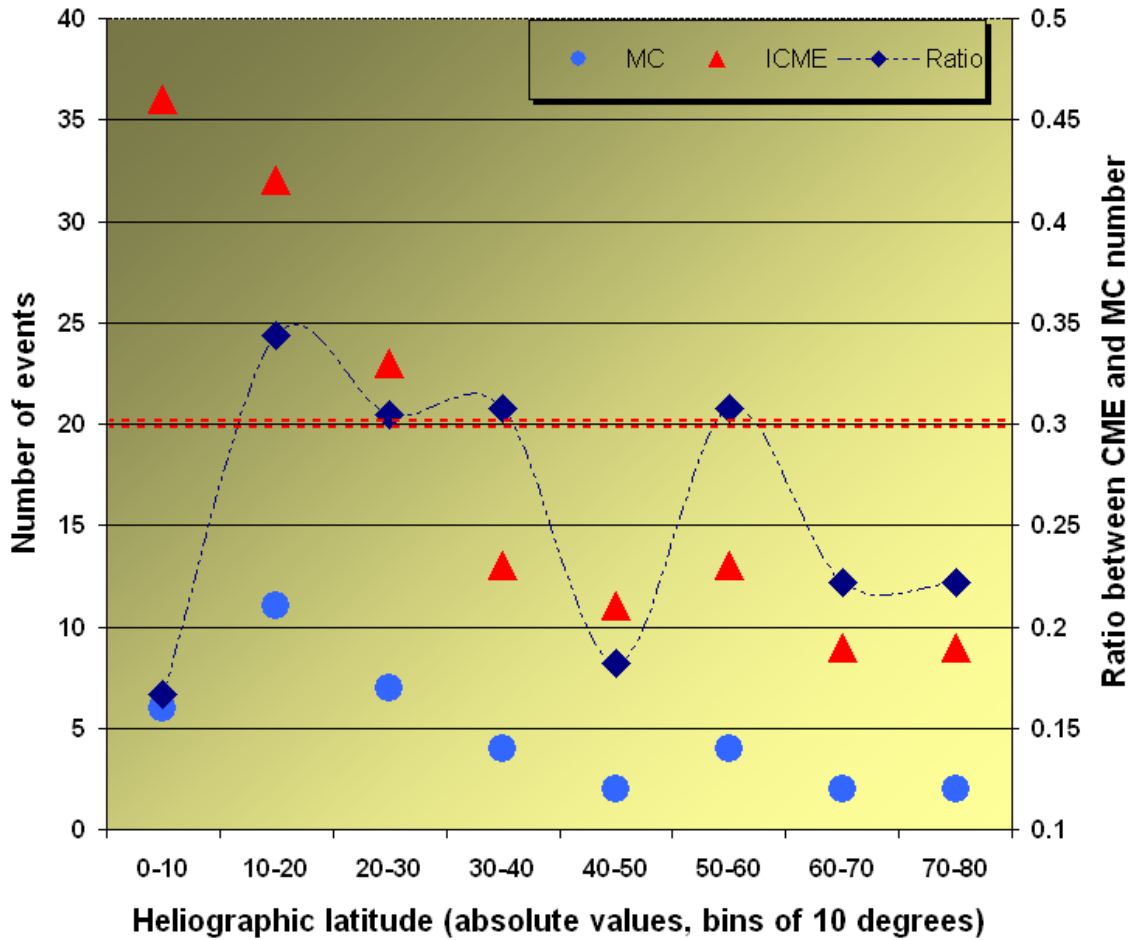
Figure 3.2. Distribution of magnetic clouds (MCs) and ICMEs as detected throughout the Ulysses mission. The events are plotted vs. heliographic latitude. The red dots represent ICMEs, the blue ones MCs and the dark blue dashed line represents the ratio between them. The double red line at 0.3 represents the ratio found by Gosling [1990] of MCs to ICMEs number at 1 AU.

3.1.1 Boundaries and Minimum Variance Analysis (MVA)

The second step in the selection process consists in applying to each of the events a MVA (Minimum Variance Analysis), used for the first time by Sonnerup and Cahill [1967]. The MVA provides a tool to identify the directions of minimum, medium and maximum variance of the magnetic field. Basically, the minimization of Equation 3.1 will provide the direction in which the variance of the field is minimum (Sonnerup and Scheible, 1998).

$$\sigma^2 = \frac{1}{N}\sum_{i=1}^{N}\left|(\mathbf{B}^i - \langle B \rangle) \cdot \mathbf{n}\right|^2 \qquad (3.1)$$

B^i individual field measurements
<B>   average value of the N field measurements

n	normal unit vector
N	number of data points

The importance of this method in relation to MC identification is closely related to the magnetic field rotation expected for these structures. The normal direction (n) in this case is the direction perpendicular to the plane of the rotation, since this is the direction of minimum variance of the field (see Figure 3.3). In this way, the MVA provides an aid to the simple eye inspection of the magnetic field data. There are certain conditions which should be fulfilled in order to consider the analysis as valid (Siscoe and Suey, 1972; Lepping and Behannon, 1980):

$$\frac{\lambda_2}{\lambda_3} \geq 2 \tag{3.2}$$

$$\not\subset (B^1, B^n) \geq 30°$$

λ_2, λ_3	eigenvalues for the medium and minimum variance directions
$\not\subset (B^1, B^n)$	angle described by the field rotation

The first condition states that the ratios of the eigenvalues corresponding to the direction of medium and minimum variance must be higher than 2. This condition implies that the ellipsoid defined by Equation 3.1 degenerates into an ellipsoid of revolution (no significance difference between the directions of minimum and medium variance). The second condition establishes a minimum value for the magnetic field rotation.

The direction of the eigenvectors corresponding to the three axes (minimum, medium and maximum variance) can be determined in the following way:.

$$\vartheta_i = \tan^{-1}\left(\frac{y_i}{x_i}\right)$$

$$\tag{3.3}$$

$$\theta_i = \tan^{-1}\left(\frac{\sqrt{x_i^2 + y_i^2}}{z_i}\right)$$

i	0 to 2, representing the 3 possible directions
φ, θ	azimuthal and elevation angle of the axis
x_i, y_i, z_i	components of the i-th eigenvector

Of special importance is the medium variance direction, since it corresponds to the axis of the flux rope (Figure 3.3).
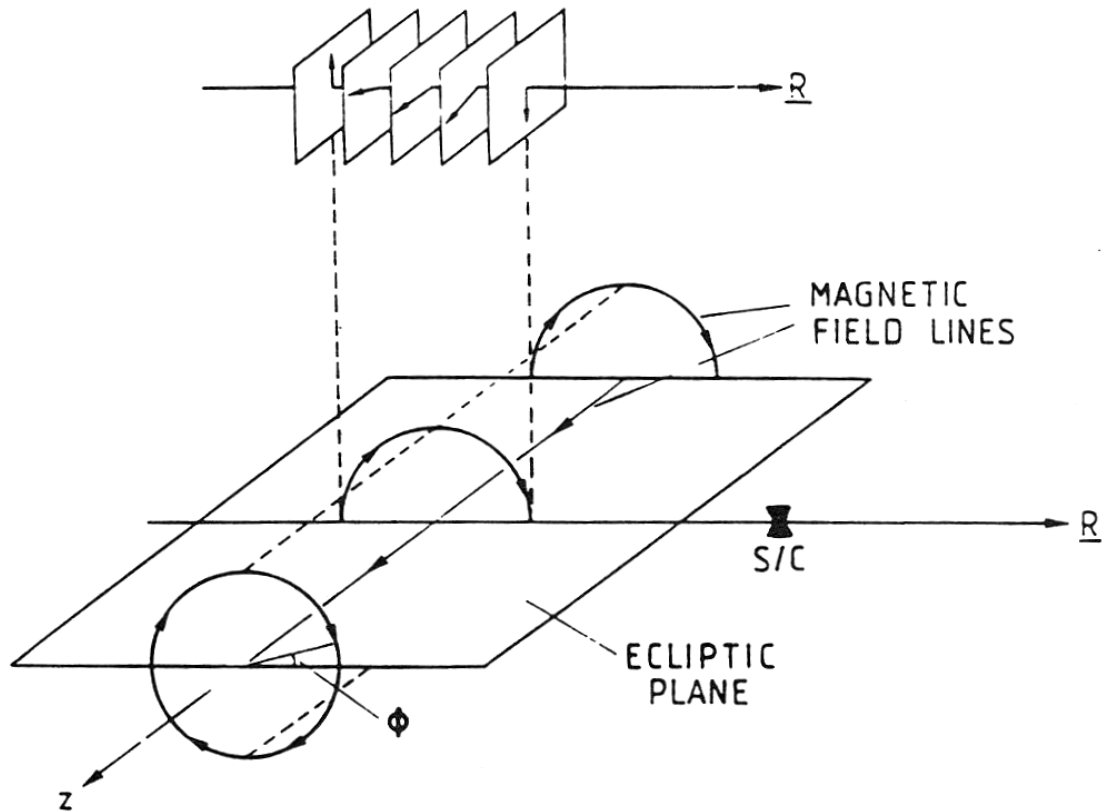
Figure 3.3. Schematics of a cylindrical interplanetary flux rope, with its axis in the ecliptic plane. The Sun is to the left. The magnetic field is parallel to the axis at the center and is increasingly poloidal near the outer edge. The direction of maximum variance is the one perpendicular to R and to the ecliptic plane. R is the direction of minimum variance. The medium variation is seen parallel to the flux rope axis. From Goldstein [1983].

This method was applied to all the selected MCs to discard doubtful cases. The visualization is obtained via hodograms (or magnetic hodographs). These are curves constructed by drawing vectors from the measured set B^i and then connecting those vectors by line segments, in the corresponding time sequence. This kind of representation allows a clear visualization of the magnetic field rotation, when present. Two examples are shown in Figure 3.4, a magnetic cloud and a non-cloud ICME (the events from Figure 3.1). From this representation, created after applying the MVA, a rotation of the field is present in the first case and not in the second one.

The determination of the boundaries (i.e., start and end of the MC interval) is not an easy task to perform, mostly due to the fact that the different signatures do not, in general, correlate in time exactly with each other. Therefore, the boundaries of each event were placed in order to contain only the period in which a flux rope-like structure is clearly seen. This is why a difference appears between the timing of the events in the Ulysses ICME list and in the magnetic cloud list from Table 3.1. The occurrence of bidirectional electrons (BDEs), which is one of the most important signatures used for the events defined in the Ulysses ICME list, may not correlate with the magnetic field rotation and low plasma beta. Furthermore, this signature is known to be quite 'patchy' (e.g. Crooker

et al., 1990), usually not present during the complete duration of the event. It is by these considerations that each author determines the start and end time of an ICME according to a specific signature. For this work, the timings are given by the magnetic field rotation and the low plasma beta, i.e., flux rope signatures. They usually confines better the MC time interval compared to other less constraining criteria.
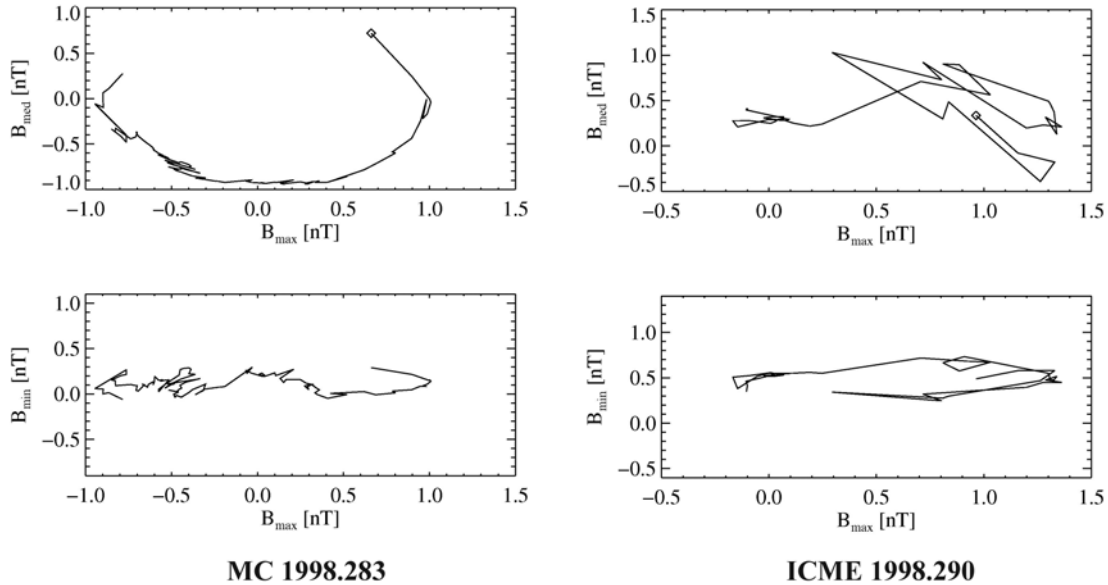
Figure 3.4. Magnetic hodographs for the two events in Figure 3.1. The one on the left corresponds to the MC, as evidenced by a clear rotation. The case shown on the right corresponds to the non-cloud ICME occurring two days after the MC. Here the rotation is not present. These two examples are the same events shown in Figure 3.1. The elevation angle of the flux rope axis (Equation 3.3) has a value of ~50°, with respect to the RT plane.

3.2 Solar wind ions

3.2.1 SWICS data analysis

The SWICS data used in this work have been processed as described in von Steiger et al. [2000]. Each event (comprising E/q, time-of-flight τ and energy ε; Section 2.3) is assigned to an ion species by analysing the τ vs. ε matrix for a specific E/q. This is shown in Figure 3.5. As a second step, the events are prioritized in order to transmit as many of the heavy ion events as possible. Finally different corrections and error checking schemes are applied to the count rates.
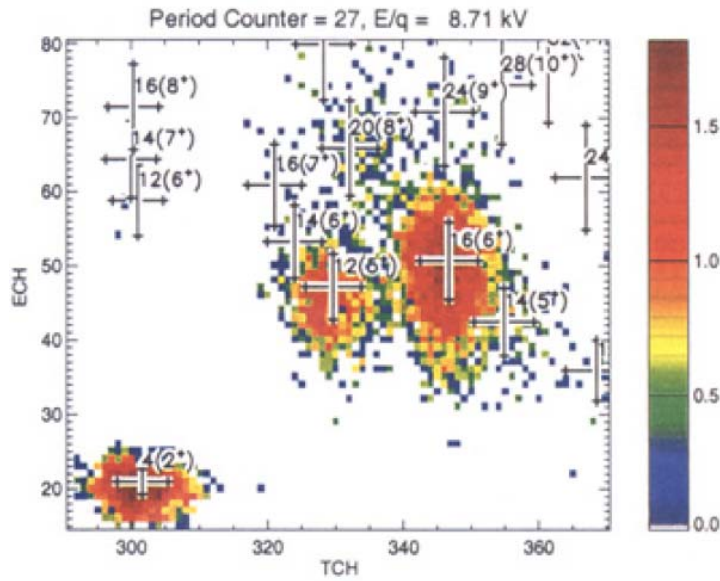
Figure 3.5. Ion counts accumulated over 10 days, for an E/q=8.71kV/e, and classified by time-of-flight (TCH) and detector energy (ECH). The color coding indicates the number of measurements. The labels include the ion mass and charge state in parentheses. From von Steiger et al. [2000].

With the count rates of each ion species as a function of energy per charge, the differential flux can be calculated:

$$dj_i(E/q) = \frac{C_i(E/q)}{t_{ac} g \eta_i(E/q, \alpha)} \tag{3.4}$$

i	species
$dj_i(E/q)$	differential flux for the species i
$C_i(E/q)$	count rate for the species i
t_{ac}	accumulation time
g	geometric factor
$\eta(E/q, \alpha)$	detector efficiency
α	sun-detector aspect angle

Differential flux is then transformed into phase space density to obtain the distribution function:

$$f_i(E/q) = \frac{1}{2\delta} \left(\frac{m/q}{E/q}\right)^2 dj_i(E/q) \tag{3.5}$$

$f_i(E/q)$	distribution function
δ	electrostatic analyzer constant

Finally, density, velocity and thermal speed can be obtained from the moments of the distribution.

3.2.2 Ionization states and the freezing-in principle

The solar wind is a collisionless plasma consisting mostly of protons (~95%), double ionized helium (or alpha particles, ~4%), and trace amounts of heavy ions. The heavy elements, even though rare, provide extremely important information about the origin of the solar wind and about transient processes occurring in the heliosphere. Early observations of minor ions in the solar wind showed the existence of several charge states of oxygen (e.g. Bame et al., 1968; Hundhausen, 1968). These measurements opened an active field in the investigation of coronal characteristics by means of in-situ interplanetary data.

The ionic composition of the different elements provides a direct measurement of the plasma properties below a few solar radii (e.g. ~1.5 R_s for oxygen). It is influenced by the electron density, the flow speed of the different ions and by the electron temperature. If one considers ionization equilibrium, i.e., a balance between ionization and recombination factors with respect to the ambient temperature, then the freezing-in principle introduced by Hundhausen in 1968 allows the estimation of the electron temperature in the source region. The processes by which the ion X^{+i} is affected are:

$$X^{+i} + e \rightarrow X^{+i+1} + e + e \qquad \text{Collisional ionization}$$

$$X^{+i} + e \rightarrow X^{+i-1} + h\nu \qquad \text{Radiative and dielectronic recombination}$$
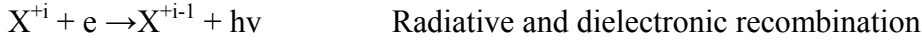
The inverse processes, three-body recombination (inverse to collisional ionization) and photoionization (inverse to radiative recombination) are negligible in the corona (Billings [1966], p. 129). The conservation equation for ionization state i of element X is then:

$$\nabla \cdot (n_i \mathbf{u}_i) = n_e [n_{i-1} C_{i-1} - n_i (C_i + R_i) + n_{i+1} R_{i+1}] \qquad (3.6)$$

$i = 0 \ldots Z$

n   particle number density
u   flow velocity
C   ionization coefficient (cm^3 s^{-1})
R   recombination coefficient (cm^3 s^{-1})

Equation 3.6 represents the rate of production of the X^{+i} ion, due to the contribution from neighbouring charge states (X^{+i-1} and X^{+i+1}) and destruction due to ionization and

recombination of X^{+i} ions. For the case of two neighbouring charge states (for example O^{+7} and O^{+6}), Equation 3.6 simplifies to:

$$\nabla \cdot (n_i \mathbf{u}_i) = n_e [-n_i C_i + n_{i+1} R_{i+1}] \tag{3.7}$$

Two extreme cases will be evaluated:
1) At the base of the corona, one can assume u_i approaching 0 and solve Equation 3.7 in the following way:

$$\frac{n_i}{n_{i+1}} = \frac{R_{i+1}}{C_i} \tag{3.8}$$

The charge states will adjust themselves according to the corresponding recombination and ionization coefficients only. The ions are in ionization equilibrium with the environment.

2) Further out in the corona the electron density drops, $n_e \rightarrow 0$, and it can be considered:

$$\nabla \cdot (n_i \mathbf{u}_i) = 0 \tag{3.9}$$

The ionization states of the ions do not change any further. They are frozen-in.

The ionization states of ions will follow Case 1 or Case 2 depending on certain time scales. One of them is related to the atomic processes (ionization and recombination time scale), defined as

$$\tau_{i \leftrightarrow i+1} = \frac{1}{n_e (R_{i+1} + C_i)} \tag{3.10}$$

The second one considers the expansion timescale of the corona in the following way:

$$\tau_{exp} = \left| \frac{H}{\mathbf{u}_i} \right| = \left| \frac{\mathbf{u}_i}{n_e} \frac{\partial n_e}{\partial r} \right|^{-1} \tag{3.11}$$

In Figure 3.6 these time scales are shown for the case of O^{+7} and O^{+6}.
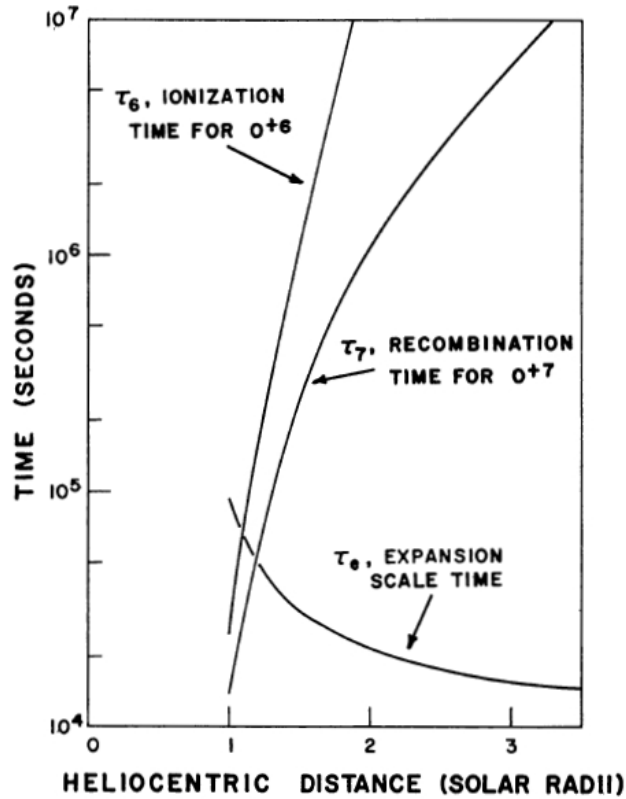
Figure 3.6. Ionization, recombination (for O^{+7} and O^{+6}) and coronal expansion timescales with respect to heliocentric distance. From Hundhausen et al. [1968].

Close to its source region, the ions in the solar wind with low speed interact with the medium. The atomic timescales are smaller than those for coronal expansion. Ions interchange energy, ionization and recombination act to balance the internal energy to the external temperature and density. This is the region described by Case 1. It represents ionization equilibrium. As the solar wind expands outwards, the coronal electron density decreases to the extent that the time scale of coronal expansion is short compared to the ionization and recombination timescale. At this height in the corona (a few solar radii), the relative ionization states become constant, they 'freeze-in' (Case 2), reflecting the conditions at this altitude. At any further distance in space, the measurement of charge states can be used to infer properties at the freezing-in altitude, providing a link between interplanetary and coronal conditions. Charge states represent in this way an imprint of the solar wind source, in contrast to other plasma parameters such as density, velocity and temperature, which undergo changes throughout the heliosphere.

According to Equation 3.8, information obtained in interplanetary space -using ionic ratios as an input- is related completely to the recombination and ionization coefficients. These are, therefore, very important and defined by Arnaud and Rothenflug [1985] as:

$$C_i = \frac{6.69 \cdot 10^{-7}}{(kT_e)^{3/2}} \sum_j \frac{e^{-x_j}}{x_j} F(x_j) \qquad (3.12)$$

C_i collisional ionization coefficient
T_e electron temperature
j   subshell number
x_j function of the ionization potential and T
A_j, B_j, C_j, D_j parameters (tabulated)
$F(x_j)$ function of x_j, A_j, B_j, C_j, D_j, $f_1(x_j)$ and $f_2(x_j)$

$$R_{rad} = A_{rad}\left(\frac{T}{10^4\,K}\right)^{-\eta} \tag{3.13}$$

R_{rad} radiative recombination coefficient
A_{rad} parameters (tabulated)

$$R_d = ADI \cdot T^{-3/2} \cdot e^{-T0/T}[1 + BDI \cdot e^{-T1/T}] \tag{3.14}$$

R_d dielectronic recombination coefficient
ADI, BDI, T0, T1   parameters (tabulated)

$$R = R_d + R_{rad} \tag{3.15}$$

R   total recombination coefficient

Ionization potentials, the parameters and numerical procedures for computing $f_1(x_j)$ and $f_2(x_j)$ are given in the above mentioned publication. Using them to solve the set of equations given, one can obtain the electron temperature (T_e) at few solar radii height in the corona. Basically, the measurement of charge states in interplanetary space allows the estimation of the electron temperature at the freezing-in radius. This temperature is called X freezing-in temperature, where X represents the element used for the calculation.

In this work this procedure has been used, with the O^{+7}/O^{+6} and C^{+6}/C^{+5} ratios (a similar process was used also with Fe charge states) obtained by the SWICS instrument. As an example of these calculations, the behavior of the oxygen freezing-in temperature (OFT) in typical slow and fast wind streams is shown in Figure 3.7.
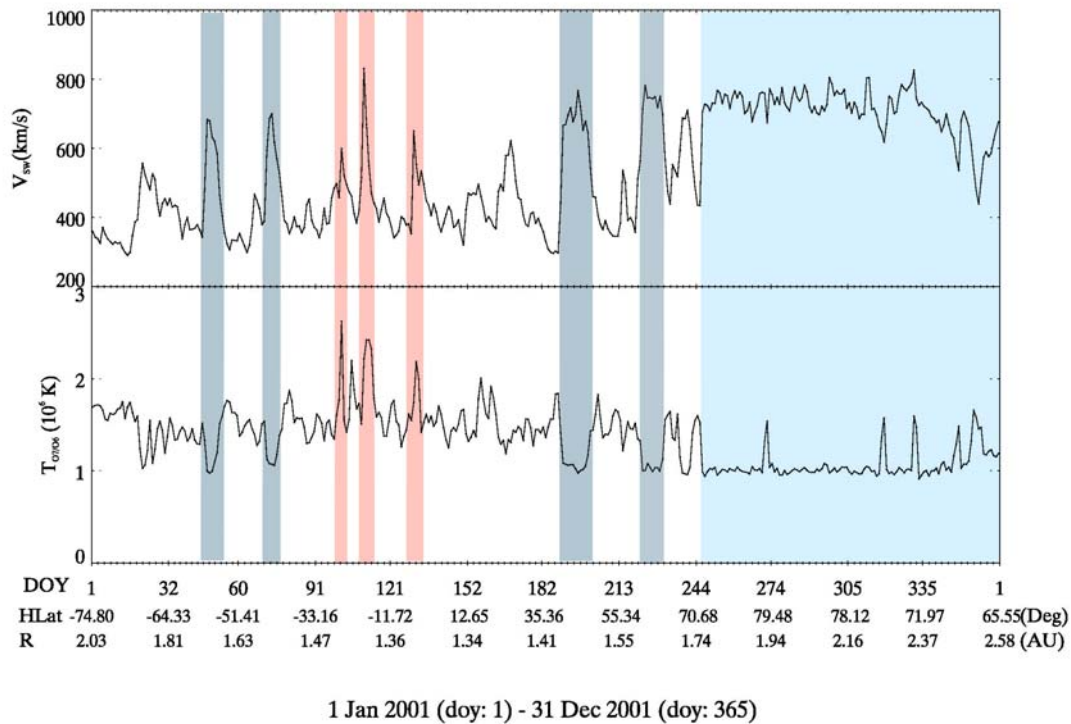
Figure 3.7. Solar wind speed and oxygen freezing-in temperature calculated using the procedure detailed in the text, for the year 2001, when Ulysses reached aphelion while flying from the south to the north pole of the Sun. The northern polar coronal hole is marked in light blue, coronal holes in grey and selected ICMEs in red.

During the year 2001, Ulysses undertook its second Fast Latitudinal Scan (FLS) in which it crossed the solar equatorial plane from south to north. The 2nd FLS encountered predominantly solar maximum conditions (until day ~250), as it can be seen by the solar wind speed of ~400 km/s perturbed by many transient events, typical in periods of high solar activity (red shaded). Throughout this interval, the OFT maintained an average value close to 1.5 MK, which is a normal value for slow solar wind. After August 2001, when Ulysses was at very high latitudes (>70°) a very interesting phenomenon occurred: the northern polar coronal hole started to form, associated with the commencement of the declining phase of solar cycle 23, seen in the solar wind speed, which grows up to 800km/s and in the OFT which lowers its average value to 1 MK, typical for fast solar wind (marked in light blue). The anticorrelation between solar wind speed and OFT is clear, particularly for the solar wind emanating from coronal holes (after day 250 in Figure 3.7). Nevertheless, as it will be shown later, the anticorrelation breaks down for transient events (see red ICME areas). Within ICMEs, OFT is markedly increased (see Chapter 4), even for events travelling at high speeds. In this way, the OFT (and the charge states ratios it represents) can be used as identifiers of the solar wind type (e.g. Von Steiger et al., 2000). A detailed explanation of this important relation will be given in the next chapter.

3.3   Energetic particles

Energetic particles in interplanetary space can be used as a tool to investigate transport processes, acceleration mechanisms and elemental abundances.

3.3.1 Particle flux

The particle flux is calculated from the measured count rate in the following way:

$$j(E,\vartheta) = \frac{CS}{G \cdot \Delta E} \tag{3.16}$$

  j   particle flux [(MeV/n)$^{-1}$ cm^{-2} s^{-1} sr^{-1}]
  CS counts per second [s^{-1}]
  G   geometric factor [cm^2 str] = 0.08 cm^2 sr (for EPAC)
  ΔE energy range [MeV/n]

Equation 3.16 describes a differential flux which considers the number of particles per unit time (CS) entering a detector with a geometric factor G and within energy between E and E + ΔE (ΔE represents the width of the specific energy channel used). The geometric factor G is the relation between area and solid angle of acceptance of the detector. It is a measure of the sensitivity of the sensor. Higher G leads to a larger counting rate of particles. Figure 2.10 is an example of how the fluxes of the measured energetic particles look throughout the Ulysses mission.

3.3.2 Elemental composition

Information on the relative abundances of the elements from He to Fe can be obtained with EPAC for energies above 300 keV/nuc. Each element represents a track in the EPAC matrix (described in Chapter 2, Figure 2.8). Due to their different energy loss in the detectors all measured counts from one species fall on the same track as shown in Figure 3.9. Using Equation 2.1, from Chapter 2, the tracks of the various ions can be identified. Three data categories of the EPAC instrument provide this information from which the relative ion abundances can be obtained. The category EV is storing the full information in 32 selected events for one instrument cycle. ER separates the matrix in 3 segments L, M, H and gives the total number of events in each segment. Finally the HS data category separates in boxes along various element tracks.

In order to obtain the composition of the particle population under study in this work, the procedure defined in Fränz [1994] is used.

Starting point is the data category EV (see Table 2.2). In the procedure all the points in the matrix which correspond to the same element are summed up. The maxima of the

tracks for different elements define the element number n_E. The results of this analysis are displayed in Figure 3.8, in which the abundances of selected elements (the atomic number is displayed on the X axis) relative to oxygen is shown.
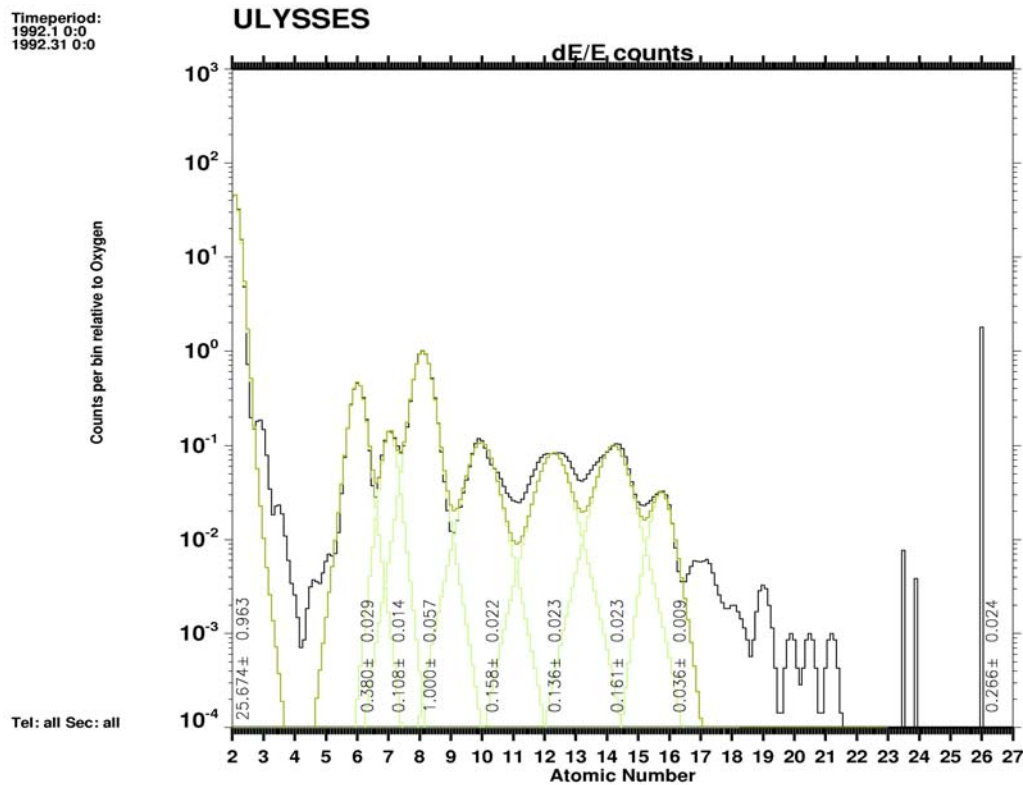
Figure 3.8. Element abundances, with respect to oxygen for January 1992. The green curves represent a Gaussian fit to the data.

The relative abundances of the different elements are obtained from the integral over the Gaussian curves, where the full width at half maximum is taken as the limit. The errors included are mostly statistical and due to overlapping of neighbouring elements. Instrumental effects known have been removed.

In certain occasions, especially when the density of energetic particles is extremely low, this analysis may lead to high statistical error levels. A more general approach consists in the use of the data category ER. The low category (L) contains mostly protons and helium. In the medium one (M) the prevailing element is oxygen whereas iron is the predominant species in the high (H) range. In this work, use has also been made of the category HS, which is created by dividing the matrix in boxes and counting the particles inside each of them. In Figure 3.9 this division is visible for the settings which were implemented in 1998. For example, in Figure 2.10 where helium and oxygen are displayed, they were obtained by using data from the HS category. There are four HS types (or species), divided in eight energy channels, giving a total of 32 boxes in the matrix for various elements. The boxes are changeable by sending commands to the spacecraft. Throughout the mission there have been four different settings, summarized in Table 3.2. Helium, oxygen and iron were defined in species 1,2 and 4 respectively. Species 3 was set to sulphur during the Jupiter encounter. In interplanetary cruise,

carbon was used instead.
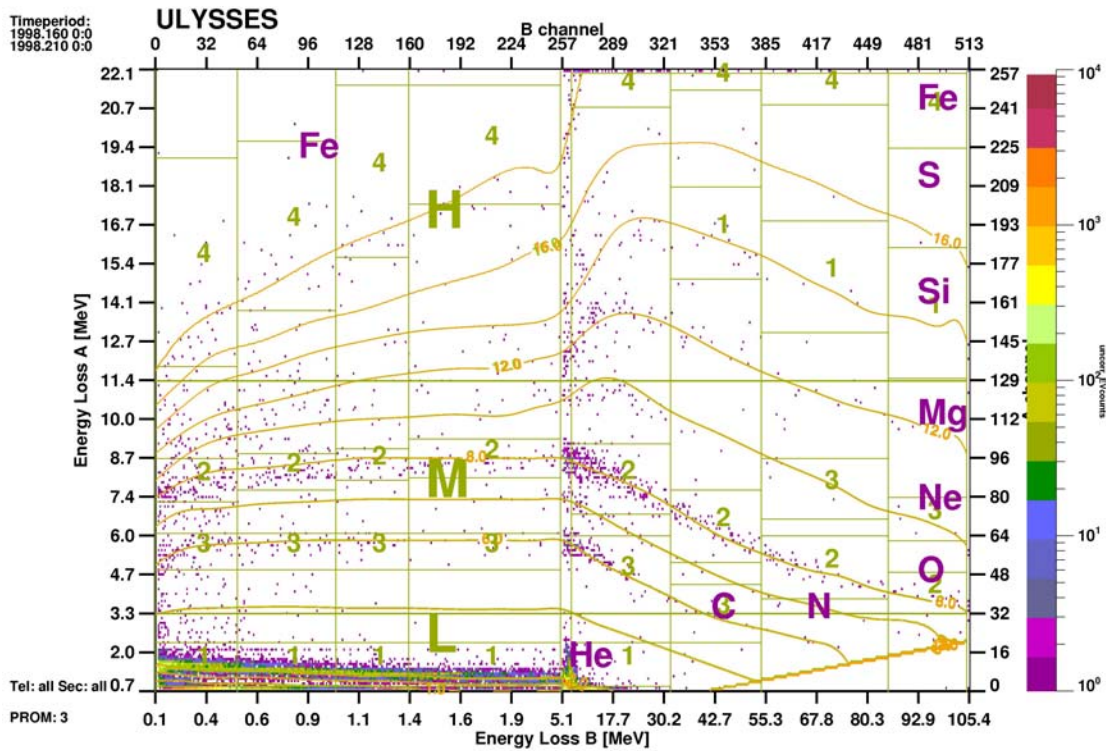
Figure 3.9. EPAC matrix with element tracks and boxes for the HS data category.

	Ch. HS	1	2	3	4	5	6	7	8
1 launch - 09/09/91	1	He	He	He	He	He	Si	Si	Si
	2	O	O	O	O	O	O	O	O
	3	S	S	S	S	S	S	S	S
	4	Fe	Fe	Fe	Fe	Fe	Fe	Fe	Fe
2 09/09/91 - 10/01/94	1	He	He	He	He	He	Si	Si	Si
	2	O	O	O	O	O	O	O	O
	3	C	C	C	C	C	C	Ne	Ne
	4	Fe	Fe	Fe	Fe	Fe	Fe	Fe	Fe
3 10/01/94 - 01/11/99	1	He	He	He	He	Si	Si	Si	Si
	2	O	O	O	O	O	O	O	O
	3	C	C	C	C	C	C	Ne	Ne
	4	Fe	Fe	Fe	Fe	Fe	Fe	Fe	Fe
4 01/11/99 - present	1	He	He	He	He	Si	Si	Si	Si
	2	O	O	O	O	O	O	O	O
	3	C	C	C	C	C	C	Ne	Ne
	4	Fe	Fe	Fe	Fe	Fe	Fe	Fe	Fe

Table 3.2. The 4 different settings of the HS allocation boxes. The first column on the left corresponds to the intervals containing each configuration. The next column shows the 4 HS species for each configuration. On the top row the 8 energy channels are specified. The table is completed with the element measured by the corresponding channel, setting and species

3.3.3 Directional anisotropies

Due to its four telescopes and sectorisation (see Section 2.2.2), EPAC is especially well suited for directional anisotropy analysis of ions. In this thesis, directional information from protons in the PS data category will be used. Each telescope is divided in eight sectors. In this way, the 32 measurements allow a decomposition of the particle intensity $j(\theta, \Phi)$ in spherical harmonics, using the method from Sanderson et al. [1985]:

$$j(\theta,\phi) = \sum_n j_n(\theta,\phi) \tag{3.17}$$

$$j_n = \sum_{m=-n}^{n} A_{nm} \cdot Y_{nm}(\theta,\phi) \tag{3.18}$$

$$Y_{nm} = P_{n|m|}[\cos(\theta)] \cdot \sin(|m| \cdot \phi) \rightarrow m < 0$$

$$\tag{3.19}$$

$$Y_{nm} = P_{n|m|}[\cos(\theta)] \cdot \cos(|m| \cdot \phi) \rightarrow m > 0$$

$$\int_{-1}^{1} P_{nm}^{2}(x) \cdot dx = \frac{1}{2n+1} \tag{3.20}$$

$j(\theta, \Phi)$	particle intensity
Y_{nm}	spherical harmonics
A_{nm}	spherical harmonics coefficients
P_{nm}	Legendre polynomials in Schmidt's normalization
n	order of the expansion

The adaptation of this method to EPAC data is described in Fränz and Krupp [1993], Fränz [1994] and Krupp et al. [1994]: The full set of 32 data points is acquired in about 16 minutes. The values of the spherical harmonics Y_{nm} are calculated and from them, the coefficients A_{nm} can be obtained by least squares fitting with the data points. There are 2n+1 coefficients, where n is the order of the expansion, which is maximal three for EPAC (the step in φ and θ directions is $\pi/4$, making 3 the maximum order attainable). In Table 3.3 each parameter up to 2nd order is displayed schematically and information on the angular distribution is given.
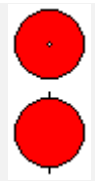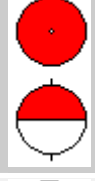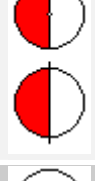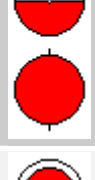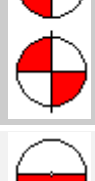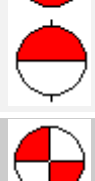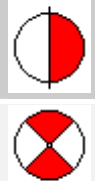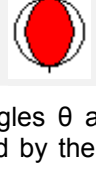
Coefficient	Description	θ	Φ	Representation
A_{00}	Isotropic	--	--	
A_{10}	Unidirectional	0	--	
A_{11}	Unidirectional	90	0	
A_{1-1}	Unidirectional	90	90	
A_{20}	Bidirectional ($A_{20}>0$) Ring at $\theta=90°$ ($A_{20}<0$)	0	--	($A_{20}>0$)
A_{21}	Bidirectional	45	0	
A_{2-1}	Bidirectional	45	90	
A_{22}	Bidirectional	90	0	
A_{2-2}	Bidirectional	90	45	

Table 3.3. Description of the harmonic coefficients up to 2nd order. The angles θ and Φ are defined with respect to the expansion pole, normally in this work represented by the magnetic field. Adapted partially from Krupp et al. [1994].

In Figure 3.10, anisotropies of protons in the energy range 0.63-0.77 MeV are shown, for a period of time in which Ulysses detected a magnetic cloud. The first panel depicts the pitch angle of the particle distribution with respect to the magnetic field. In the rest of the panels the harmonic coefficients of up to 2nd order are plotted. The harmonic expansion is done with the magnetic field as the expansion pole. In this example, the predominant flux of protons is along the magnetic field. Therefore when the fluxes are high for pitch angles of 0° and 180° in relation to those seen at 90°, A_{20} is increased. A_{10} significantly deviates from zero during short intervals, symbolising monodirectional field-aligned population. The properties of energetic particles in MCs will be extensively discussed in the following chapters and shall not be discussed deeper here.
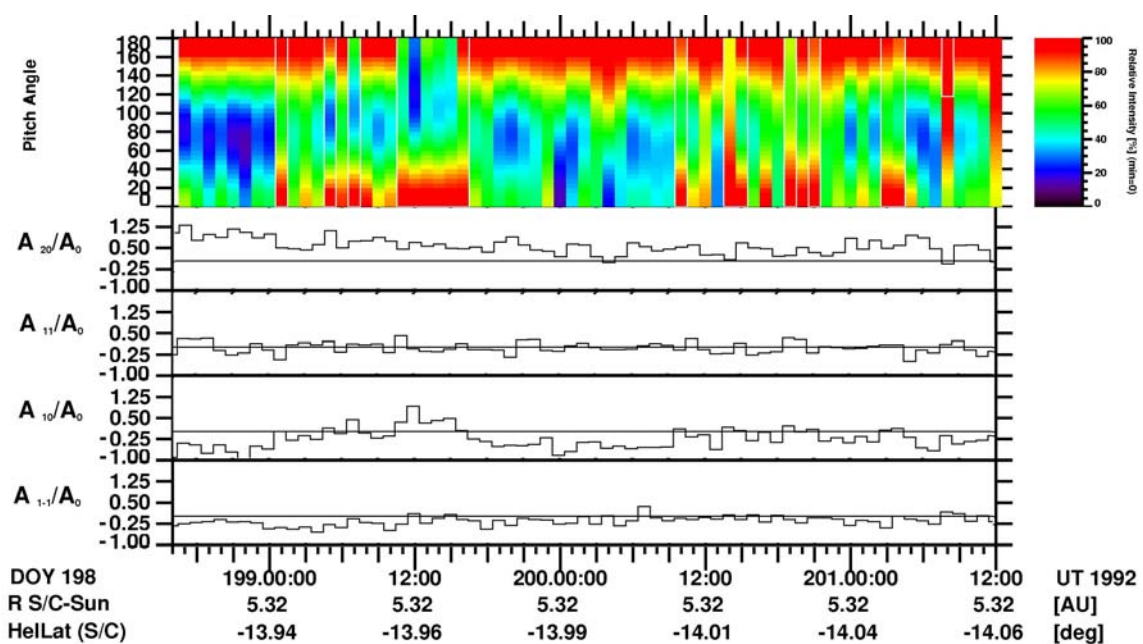
Figure 3.10. Pitch angle (top panel) and selected harmonic coefficients of 1st and 2nd order. This period corresponds to a magnetic cloud passage, detected by Ulysses on its way to the south pole of the Sun. The magnetic field is used as the expansion pole for the harmonic expansion.

3.4 Modeling the magnetic field in MCs

Due to their characteristic internal magnetic field configuration, magnetic clouds have been modelled extensively. Although magnetic clouds are three-dimensional objects, the magnetic field vector cannot be measured at any desired point inside this structure. Experimental data are limited to the line that corresponds to the trajectory of a spacecraft inside the cloud as it propagates away from the Sun. In this scenario, the models have to take into account not only the magnetic field topology, but also the position inside the magnetic cloud where those experimental data were obtained. Minimum Variance

Analysis (MVA, Section 3.1.1) has been used in the past as a first approach to unveil the magnetic field configuration in MCs. For example, Bothmer and Schwenn [1998] applied a MVA to study magnetic clouds detected by the Helios spacecraft. Assuming that the X, Y and Z axes of a flux rope are near the minimum, maximum and medium direction of variance, they used the MVA to find the orientation of the flux rope axis with respect to the ecliptic plane. As with all the other methods described here, the determination of these angles (and the rest of the parameters) becomes more uncertain as the closest approach of the spacecraft to the cloud axis increases. A scheme, like the one shown in Table 3.4 has been later applied to obtain a first approximation of the magnetic field configuration in MCs.

MC Type Magnetic helicity Number of MCs during 1974–1981	Variation of magnetic field vector	Direction of magnetic field on flux tube axis	Rotation of magnetic field vector in Bz-By-plane (Bx^*-By^*-plane)
SEN Left-handed 17	South ($-Bz$)→north ($+Bz$)	East ($+By$)	
SWN Right-handed 17	South ($-Bz$)→north ($+Bz$)	West ($-By$)	
NES Right-handed 6	North ($+Bz$)→south ($-Bz$)	East ($+By$)	
NWS Left-handed 6	North ($+Bz$)→south ($-Bz$)	West ($-By$)	
Orientations for high inclinations to the ecliptic SEN, NWS, SWN, NES	East ($+By$)→west ($-By$) West($-By$)→east($+By$)	North ($+Bz$)→south ($-Bz$) South ($-Bz$)→north ($+Bz$)	Rotations in By-Bz- (By^*-Bx^*-) plane

Table 3.4. Scheme of MC classification according to their magnetic field orientation and rotation. From Bothmer and Schwenn [1998].

Numerical models have been originally applied considering that a MC is described by a force-free field configuration with cylindrical geometries (applying the solution provided by Lundquist, 1950), comparable with the ones shown in the first column of Table 3.4. Force-free means that the current density and the magnetic field vector are parallel, and thus the electromagnetic force vanishes. These models are constructed assuming that:

$$\nabla \times \mathbf{B} = \mathbf{J} = \alpha \mathbf{B} \tag{3.21}$$

Introduced by Goldstein [1983] using a variable α, this model was used later by Marubashi [1986] to fit experimental data. Burlaga et al. [1988] proposed the use of a constant α, providing the following solution:

$$\nabla \times (\nabla \times \mathbf{B}) = \alpha(\nabla \times \mathbf{B}) = \alpha^2 \mathbf{B} \tag{3.22}$$

$$\nabla^2 \mathbf{B} = -\alpha^2 \mathbf{B} \tag{3.23}$$

The solution of Equation 3.23 was given by Lundquist [1950] in cylindrical coordinates and in terms of Bessel functions. In this way, the axial (B_a), tangential (B_t) and radial (B_r) components of the magnetic field are defined by:

$$
\begin{aligned}
B_a &= B_0 J_0(\alpha r) \\
B_t &= B_0 H J_1(\alpha r) \\
B_r &= 0
\end{aligned}
\tag{3.24}
$$

B_0	magnetic field at the cloud's axis
J_0, J_1	zeroth and first order Bessel functions
H	handedness of the field, or helicity sign
r	distance to the cloud's axis

Lepping et al. [1990] developed an algorithm to fit magnetic field data to these solutions. The algorithm has several steps. First, a MVA is made, to obtain an initial coordinate system. Then, a least squares minimization is applied between the data and the Lundquist solution. An additional fit is carried out for the estimated field strength at the axis of the cloud. The free parameters in this method are the local orientation of the cloud axis (given by elevation, or latitudinal angle θ and by azimuth or longitudinal angle Φ) normally with respect to the ecliptic plane and to the Sun-spacecraft line; the closest distance of the spacecraft trajectory to the cloud's axis (the "impact parameter" y_0); the time to closest approach (t_0); the sign of the cloud's helicity (H); the amplitude of the magnetic field at the cloud's axis (B_0) and the parameter α (related to the size of the cloud). The Lepping model usually reproduces correctly the magnetic field direction but generally is unable to fit the field magnitude with high accuracy. Figure 3.11 shows an

example of a magnetic cloud fitted with this model, data from other satellites are used in this case.

Toroidal force-free structures have been used by Vandas and Romashets [2003] (and references therein) in order to approximate possible effects of curvature of the magnetic field configuration. Recently, supported on the possibility of an active role of the plasma pressure, which is observed in experimental data, non force-free models have been applied to MCs (e.g. Hidalgo et al., 2002a, 2002b; Mulligan and Russel, 2001). In this work, the models by Hidalgo et al. [2002a, 2002b] are used to fit the Ulysses magnetic field data. Therefore they will be described in more detail in the next sections. The choice of this model was based on better comparative results with respect to force-free models (Hidalgo et al., 2002a) and due to its simpler application.
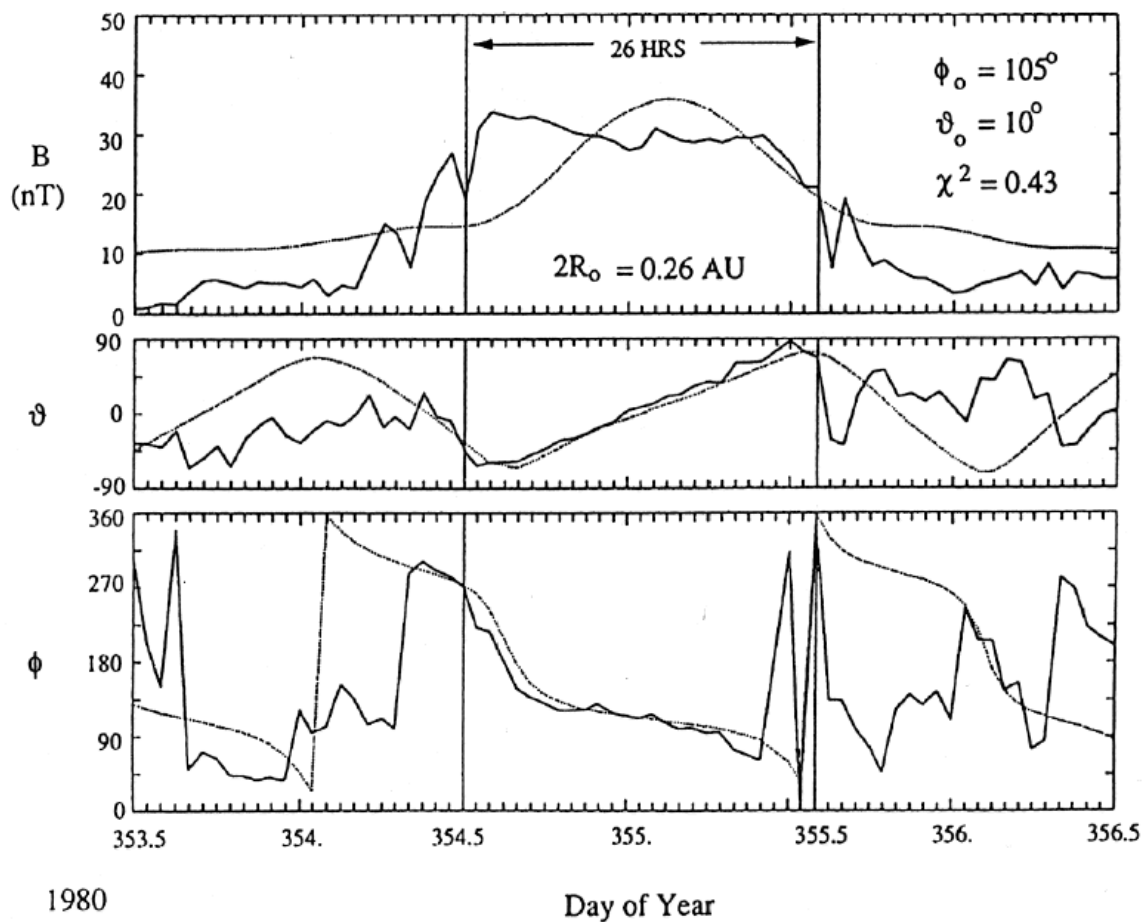
Figure 3.11. Force-free fit (overlaid line) to a magnetic cloud observed in September 18 1980 by the IMP 8 and ISEE 3 spacecrafts (solid line). Φ_0 and θ_0 represent the attitude of the cloud's axis obtained from the fit and $2R_0$ is an estimate of the cloud's diameter. From Lepping et al.[1990].

3.4.1 A non-force free model for magnetic clouds

The initial model is described in Cid [2000] and Hidalgo et al. [2002a]. Although in these papers the authors consider as starting point the geometry of a magnetic torus, they

only model the local structure, assuming then a cylindrical geometry with local configuration similar to the ones shown in the first column of Table 3.4. Therefore, the geometry is represented by a cylinder with circular cross section. The field has an axial component (B_a) and a poloidal component (B_p). The radial component is assumed to be zero ($B_r=0$), as in the force-free model. In this way, the current density vector will be given by $\mathbf{j}=(0,j_p,j_a)$, where the components are considered to be constant. For this configuration and under the given constraints, the solutions of the Maxwell equations are:

$$B_p{}^{MC} = \frac{\mu_0}{2} j_a r$$

$$B_a{}^{MC} = \mu_0 j_p (R - r)$$

(3.25)

μ_0 vacuum permittivity
r   distance to the cloud's axis
R   cloud's radius

In this way, the poloidal component of the magnetic field is created by the axial current density and vice versa. $B_p{}^{MC}$ is zero at the cloud's axis and increases with distance from it, to reach its maximum value at the outer surface of the flux rope (where its pitch angle is 90°), again, the opposite applies for $B_a{}^{MC}$.

The next step consists in transforming the values between the reference system used by the model and the corresponding coordinate system in which the data are measured. Equation 3.25 describes the magnetic field in what is called the magnetic cloud (therefore the MC superscript) reference system. These expressions are evaluated point by point using the solar wind speed (measured by the SWICS instrument) and several geometric considerations detailed in Hidalgo et al. [2002a]. These geometric calculations provide the position of the spacecraft inside the MC as a function of time, needed to calculate the magnetic field according to Equation 3.25. In Figure 3.12 a schematics providing a geometrical reference frame for the model is given.
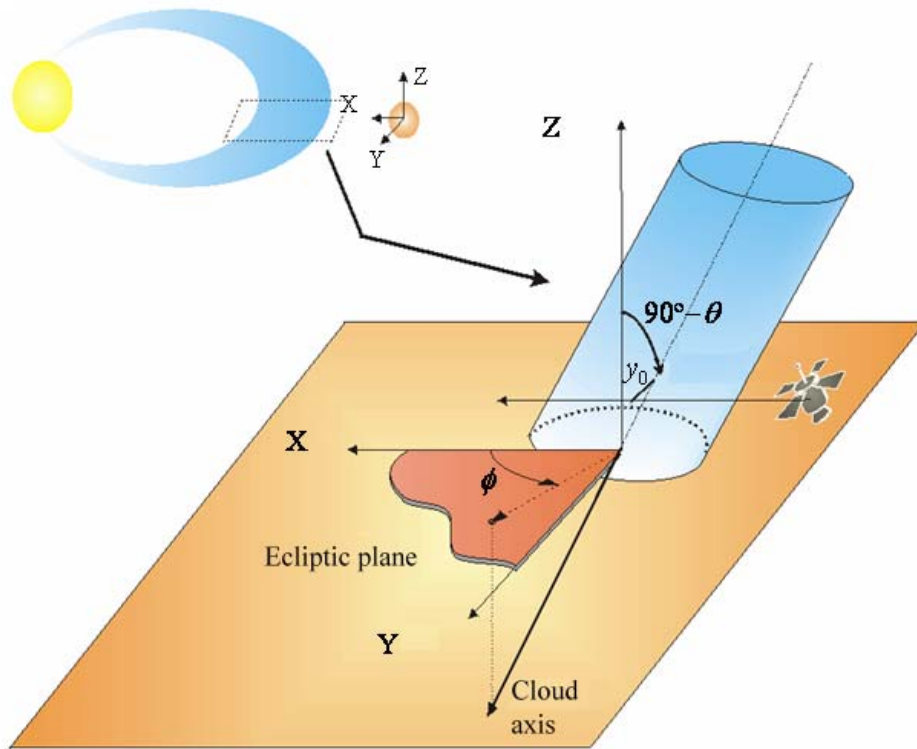
Figure 3.12. Sketch showing the attitude angles (θ and Φ) and the reference system in which the model is developed. Adapted from Cid [2000].

The values calculated using the Maxwell equations for the magnetic field vector, are least squares fitted against the values of the magnetic field measured by Ulysses. In order to enable this comparison, both sets of data points and calculated points should be in the same reference system. Therefore the calculated values have to be transformed from the local magnetic cloud reference system into the system in which the data are measured (RTN for Ulysses). After the fitting, the code iterates by modification of the free parameters, until the error (χ^2) is minimized by modification of the free parameters.

The free parameters included in this model are the axial and poloidal components of the current density; the angles θ and Φ; y_0 (impact parameter) and the current density components. The radius of the cloud R is obtained directly by geometric calculation and it is not a free parameter. The sign of the helicity is obtained from the sign of the axial component of the current density j_a. Therefore two parameters less are needed for this model, with respect to the Lepping model.

As an example, in Figure 3.13 a fit to a MC from Table 3.1 (day 242, 1997) using this model with Ulysses data is shown. The model fits the data qualitatively well ($\chi^2 = 0.02$). This modelling approach is less confident for the magnetic field magnitude than with the separated components. A better approach will be introduced in the next section.
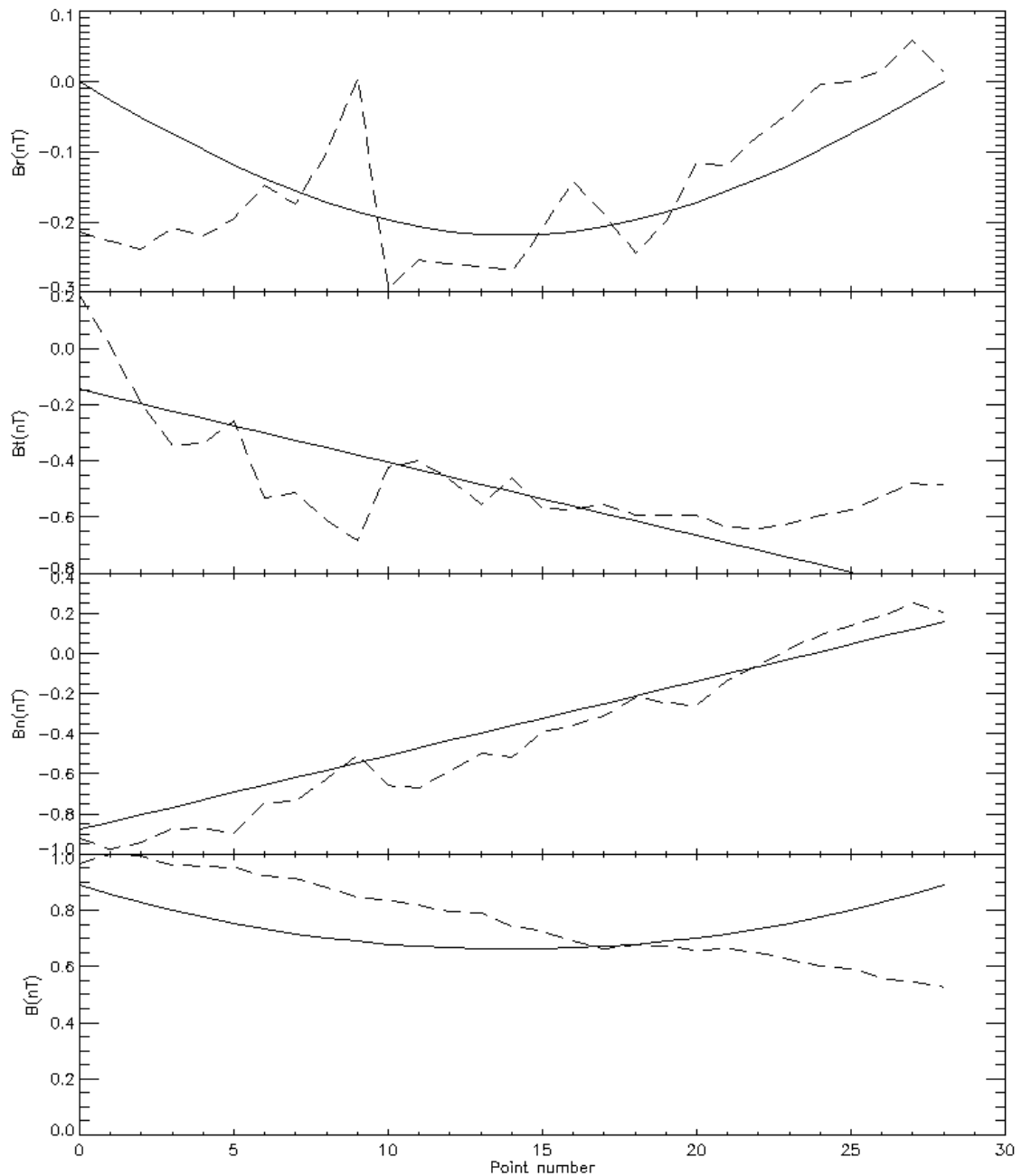
Figure 3.13. Fit to a MC detected in 1997, day of year 242. Dashed lines are the real data, in RTN system, from the Ulysses magnetometer. Solid lines represent the model fit to the data.

3.4.2 A non-force free model for magnetic clouds with elliptical cross section

Hidalgo et al. [2002b] developed an advanced non force-free model in which the cross-section of the magnetic cloud needs not to be circular. An elliptical cross-section is considered as the first step to approximate the deformation of magnetic clouds due to propagation in the heliosphere. With this new geometry, the solution becomes:

$$B_t = B_t^0 + \frac{\mu_0 j_r r \sqrt{\sin^2 \varphi} \cosh \eta}{tg\varphi}$$

(3.26)

$$B_p = -\frac{\mu_0 j_y^0 r \cosh \eta}{(\cosh^2 \eta - \cos^2 \varphi)^{1/2}}$$

with $\cosh \eta = 1/\varepsilon$.

φ	angular coordinate of the cloud's section
ε	eccentricity of the ellipse
B_t^0	axial magnetic field at the cloud's axis
j_r, j_y^0	radial current density, current density on the cloud's axis

With the use of η, the model can adapt to a circular (large values of η) or elliptic cross section (η close to 0).

Here, a second change introduced by Hidalgo [2003] has also been incorporated into the model. Namely the expansion of the cloud as it travels past the spacecraft is considered by using non-constant current densities. The current densities will now depend on time in the following way:

$$j_y^0 = \lambda(t_0 - t)$$
$$j_r = \alpha(t_0 - t)$$

(3.27)

λ, α	constants
t_0	time factor (related to the cloud's expansion)

This represents three more free parameters for the model. Finally, in the transformation from the cloud reference system into the one provided by the magnetic field dataset (GSE, RTN, etc) there will be one parameter more which represents the inclination of the ellipse, ζ. This parameter was not needed in the circular model, due to its rotation symmetry. In this way, the elliptical model including expansion effects will make use of nine parameters: θ and φ (attitude of the cloud's axis), λ and α (factors of the current density), η (eccentricity factor), t_0 (characteristic expansion time), ζ (orientation of the cloud's cross section), B_y^0 (magnetic field of the cloud axis), y_0 (closest approach distance of the spacecraft to the cloud axis).
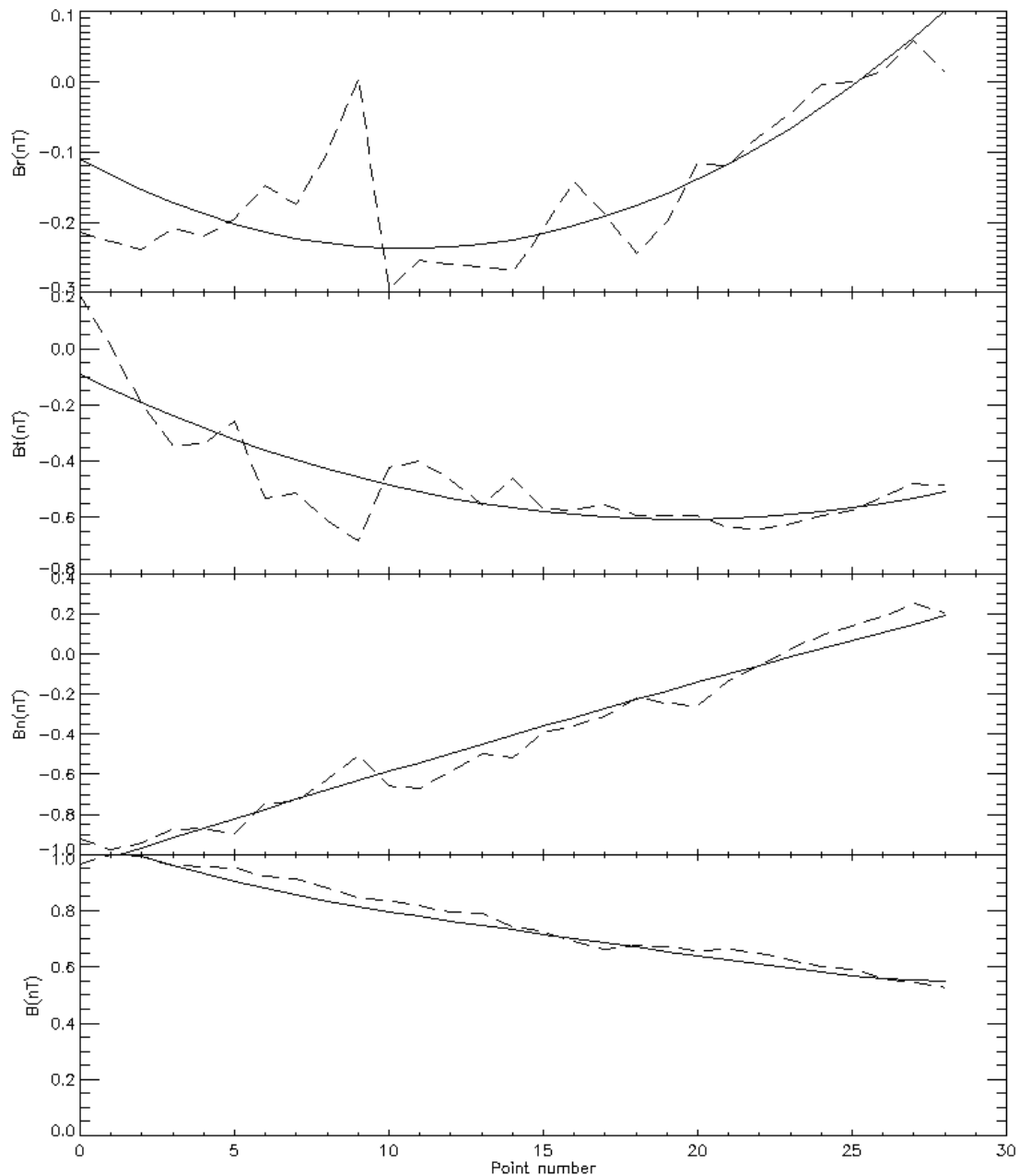
Figure 3.14. Fit using the elliptical model to the same MC as the one used in Figure 3.13. The improvement is clearly visualized.

In Figure 3.14 the model is fitted to the data from the event shown in Figure 3.13. Now, the magnitude is correctly fitted by the model, χ^2 reduces from 0.02 to 0.006. The improvement introduced by the use of the new model is easily noticeable, specially in the T component and magnitude. The use of a radial current density in the elliptic model allows non-symmetric magnetic field configurations to be better fitted. This model will be used in the following chapters to fit magnetic cloud data and obtain important characteristics about them. In order to facilitate its implementation, a previously inexistent, completely automated IDL code for this model with its different implementations (circular and elliptic) have been developed during the course of this work.

Chapter 4 Solar wind ions and ICMEs

Charge state distributions and abundances of ions heavier than helium are at present among the most powerful tools to investigate the solar wind. They have been studied since they were discovered in the 1960's. Nevertheless only recently, with modern space instrumentation like the SWICS instrument on Ulysses and ACE, it has been possible to gain a powerful insight into their physical meaning. Specifically variations of charge state distributions in relation with ICMEs are of particular interest, since they represent an imprint of the source temperature. In this chapter, charge states will be used to sample the internal structure of ICMEs and Magnetic Clouds (MCs).

4.1 Introduction

The first relation between charge state variations and ICMEs was establish when high ionization states of oxygen and iron were detected following interplanetary shocks. Bame et al. [1979] explained these enhancements as plasma being heated by flares, an explanation recently revisited by Lepri and Zurbuchen [2004]. Different types of solar wind flows were related to their ionization states by Fenimore [1980]. This author found that periods with highest ionization levels were those connected to ICME signatures.

Nevertheless, high ionization levels and thus high freezing-in temperatures were not present in every ICME-related period. The improved composition data available nowadays confirms this picture, the periods with highest freezing-in temperatures correspond to ICMEs, but not all ICMEs exhibit high charge states. Only a subset of all the CMEs seems to have conditions favourable for ionizing the internal plasma up to levels clearly higher than those for normal quiet solar wind.

Increases in the O^{7+} to O^{6+} ratio inside a few ICMEs were reported by Galvin et al. [1993], for events detected during the in-ecliptic phase of the Ulysses orbit. In 1997, Galvin reported on ICMEs which show nominal, i.e., ambient solar wind, charge states. Again, this resembles the results by Fenimore [1980], in the sense that apparently not every ICME is related to high ionization levels. Finally, Henke et al. [1998] resolved the ambiguity and demonstrated that the O^{7+} to O^{6+} ratio is clearly increased if the ICME has a magnetic cloud structure. This result will be further explored in this work. Using other ions, Lepri et al. [2001] studied periods with unusually high iron charge states detected by the ACE spacecraft and found that they were, almost entirely, associated with ICMEs, from which many were magnetic clouds.

In very rare occasions, ICMEs with unusually low charge states have been found by Schwenn et al. [1980] and Gosling et al. [1980]. These authors found singly ionized helium in the driver gas following an interplanetary shock. The explanation provided for such low temperatures was the presence of cold prominence material, of chromospheric origin. These and other periods of abnormally low charge states were analysed by Zwickl et al. [1982]. In the frame of the mentioned study, even periods with both high and low ionization states were detected, indicating mixing of the plasma and spatial inhomogeneity within these events.

By using a larger statistical dataset than the one of Henke et al. [1998], covering more than one solar cycle and using the full range of latitudes provided by the Ulysses orbit, the variation of the freezing-in temperature as deduced from the O^{7+} to O^{6+} during magnetic cloud passage will be studied. A more rigorous classification criteria is used here, only periods which fulfils the points detailed in Section 3.1 are included in the analysis. Furthermore, in this work, the considerations based on the O^{+7}/O^{+6} ratio are extended to carbon and iron ions. In this way, a more global view of the phenomena occurring in relation with magnetic clouds and non-cloud ICMEs can be obtained. As will be shown, this is particularly important with respect to the internal structure of MCs. In addition, the charge state distributions seen by Ulysses will provide information on the processes occurring during the early stages of the solar eruption.

4.2   Oxygen freezing-in temperatures (OFT)

As already introduced in Section 3.2, from all the physical parameters which can be measured in-situ by a spacecraft in interplanetary space, there is one which is not affected by the development of the solar wind as it travels through the heliosphere. This parameter is the ionization state of the solar wind ions, which due to the low densities prevailing already at a few solar radii from the Sun, remains unchanged as the solar wind propagates outwards. By measuring charge states of solar wind ions, properties present in the source region of the solar wind, can be analysed at any distance in the heliosphere. Charge states represent in this way an imprint of the solar wind source, in contrast to other plasma parameters such as density, velocity and temperature, which vary significantly between the corona and interplanetary space. The freezing-in temperature of oxygen was calculated in the manner described in Section 3.2. Oxygen is preferentially chosen because it is most abundant in the solar wind and thus provides the best statistics, even on relatively short time scales, necessary for investigation of transient events.

4.2.1 OFT and magnetic clouds

With the described procedure, each data point of O^{+7} / O^{+6} was assigned an oxygen freezing-in temperature. In Figure 4.1, a magnetic cloud (MC) detected by Ulysses at low latitudes and close to aphelion is shown. The rotation in the magnetic field occurs from south to north, while the intensity of the field is greatly increased during the first part of the event. A low plasma beta and proton temperature complements the signatures which characterize an MC. The new feature included for the classification is given by the oxygen freezing-in temperature. The OFT shows a distinctive behavior inside the cloud. It is persistently enhanced throughout the event, reaching values of 2 MK, more than 0.5 MK higher than the slow solar wind in which it is embedded. Notice that the OFT values are not increased during the sheath period preceding the cloud. The sheath region comprises turbulent, piled up solar wind.
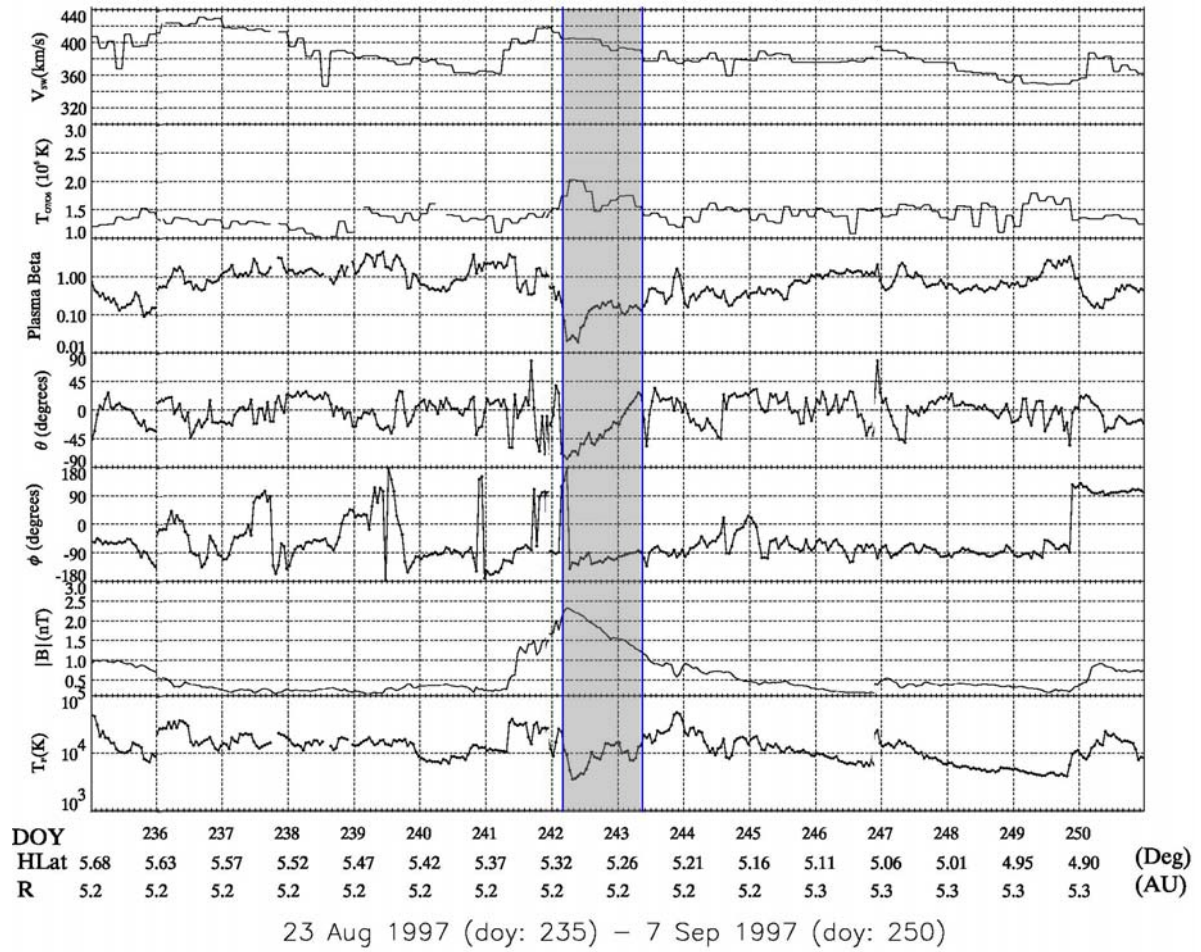
Figure 4.1. MC detected by Ulysses at 5 AU from the Sun. The MC is marked by the shaded region. From top to bottom the parameters displayed are: Solar wind speed, Oxygen freezing-in temperature, plasma beta, elevation and azimuthal magnetic field angles, magnetic field magnitude and proton temperature.

The next step consisted in the calculation of a characteristic freezing-in temperature for all identified cloud events (Table 3.1) and, in order to establish a comparison, a characteristic temperature for the surrounding solar wind. For each cloud, the average value of OFT is found using every data point inside the MC. To consider the ambient solar wind outside the cloud, a 20-day OFT running average value, centered on the cloud, was used.

Next, a calculation of the temperature difference between a magnetic cloud and the surrounding ambient solar wind was carried out in the following way:

$$T_{diff} = \frac{100 \cdot (T_{in} - T_{out})}{T_{out}}$$

(4.1)

T_{diff} OFT difference between magnetic cloud and surrounding ambient solar wind
T_{in} OFT inside MC
T_{out} OFT in the surrounding ambient solar wind

In this way, an analysis over the whole dataset of 40 magnetic clouds, comprising all latitudes and phases of the solar cycle was undertaken for the first time. Two events were left out of the analysis, due to data gaps. The statistical results of this procedure are displayed in Figure 4.2. In more than 90% of the cases the temperature was significantly increased. The average increase amounts to 26%. For only two events the OFT is essentially stable within the accuracy of the measurements.
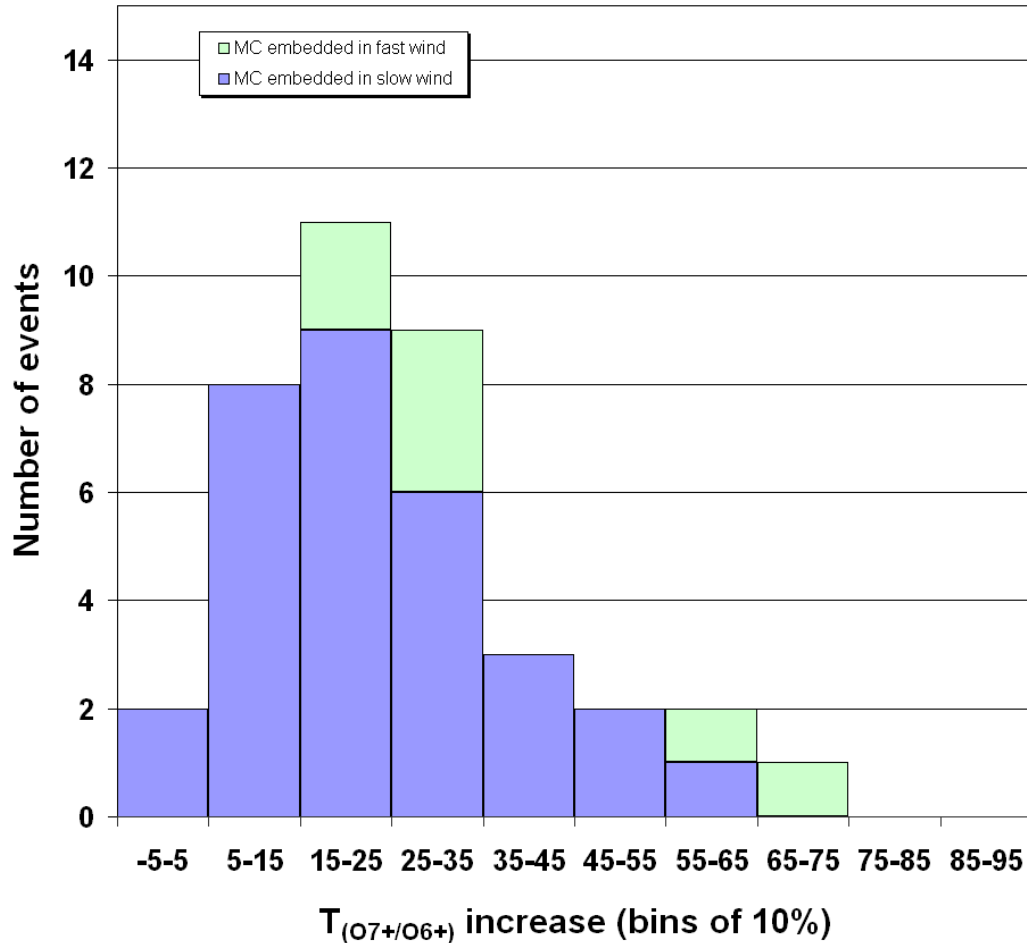
Figure 4.2. Increase in OFT between magnetic clouds and the ambient solar wind. From Rodriguez et al. [2004].

A differentiation was made on whether the cloud was immersed in fast (17% of the events, green color in Figure 4.2) or slow solar wind (blue in the figure). For classifying the surrounding solar wind not only its speed was used, since this might be confusing in the presence of transient events. As it was seen before (Section 3.2.2), the freezing-in temperature is a good tool to distinguish between fast flows (from coronal holes) and slow flows (from the streamer belt). Therefore, the 20-day running average of the freezing-in temperature surrounding each event was used, complemented by the speed of the ambient wind. This represents a new method that provides a more robust identification criterion. Both solar wind types were then separated in the following way:

- Slow wind: the average OFT should be higher than 1.35 MK
- Fast wind: the average OFT should be lower than 1.3 MK. Or if the average OFT is between 1.3 MK and 1.35 MK, then the solar wind speed must be higher than 500 km/s.

These conditions were established by analysing the correlation between solar wind speed and oxygen freezing-in temperature during long periods of time. The division was made in order to investigate a possible impact of the different conditions in which the MCs are immersed on their internal properties. Normally, MCs embedded in fast solar wind will show significant increases in freezing-in temperature. These increases are clearly more pronounced in fast solar wind (since it has lower freezing-in temperatures) than when the events are surrounded by slow solar wind, which originates in closed magnetic field regions in the low corona and presents higher freezing-in temperatures.

4.2.2 Latitudinal and Solar Cycle variations

The extended lifetime and unique orbit of Ulysses allow the investigation of a possible dependence of magnetic clouds with heliographic latitude and solar cycle. Unfortunately, the overlapping of solar cycle variations with different heliographic latitudes makes it complicated to disentangle possible dependences on either parameter.

Using bins of 10 degrees of absolute heliographic latitude, all the MCs present inside each bin have been computed and a characteristic OFT value per bin is obtained. In this way Figure 4.3 was created. The same procedure was carried out with the temperatures outside each cloud (using again the 20-day running average). This is displayed as the dots in Figure 4.3. Inside magnetic clouds the oxygen freezing-in temperature is clearly increased with respect to the ambient solar wind at all latitudes, as expected from Figure 4.2.
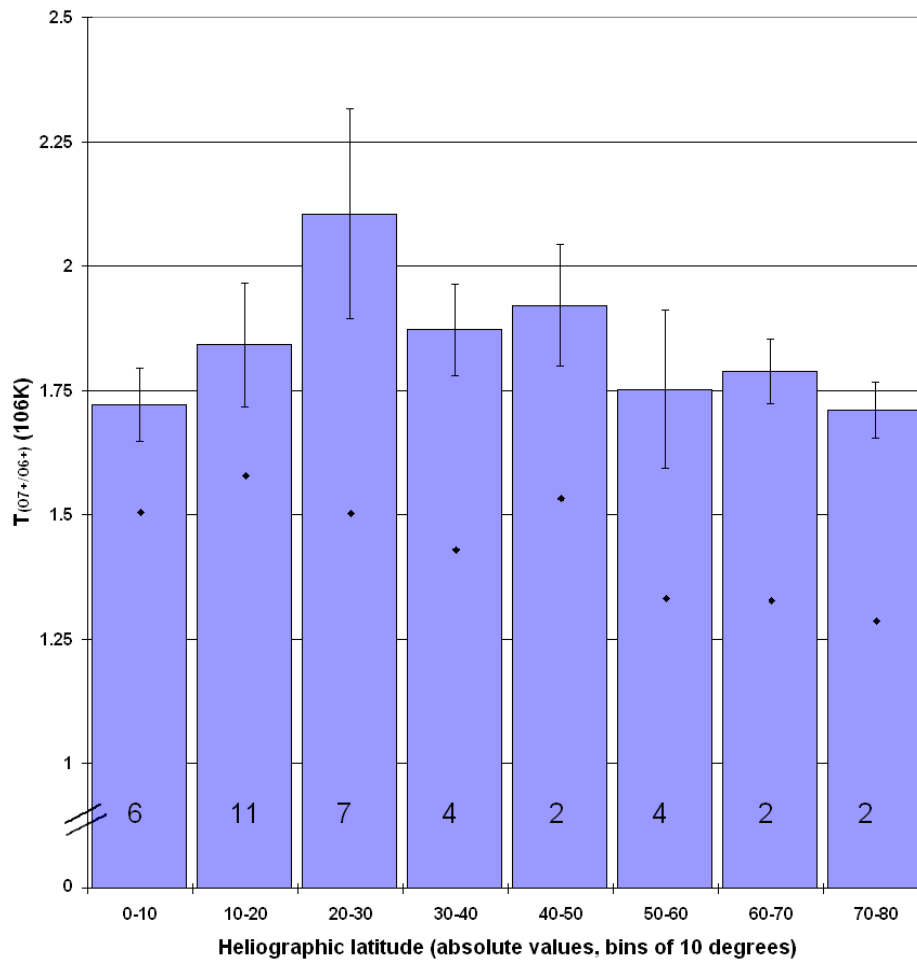
Figure 4.3. Distribution of freezing-in temperatures inside MCs and in the neighbouring solar wind (dots) vs. heliographic latitude. The numbers in each bar represent the number of MCs used for its calculation. Adapted from Rodriguez et al. [2004].

The ambient OFT appears fairly constant, except for high latitudes, where it decreases due to the influence of solar wind streams originating in the polar coronal holes. Nevertheless, this decrease in the ambient temperature, is not reflected in the OFT within MCs, which remains increased at a stable level. In this way, and as it was stated before, high differences between the internal and external OFT are seen at high latitudes due to the low freezing-in temperatures of the fast solar wind. Probably the only exception for the constant OFT within magnetic clouds is seen in the 20°-30° bin which shows the highest absolute values and the highest difference between internal and external MC temperature. A possible explanation for this behavior might be that within this latitudinal range on the Sun the most active regions are located. Therefore this region represents the preferential zone from where most CMEs are ejected (Figure 4.4). Furthermore, at these latitudes they are generally associated with active regions.

SR Latitude Frequency
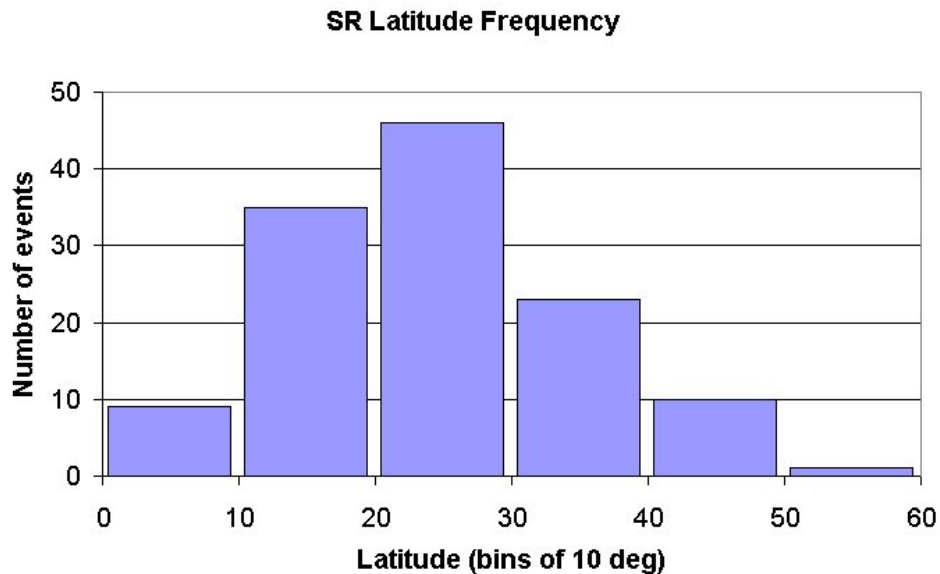
Figure 4.4. Source region (SR) location of 124 structured CME events analysed by Cremades and Bothmer [2004]. Image courtesy H. Cremades.

In order to analyze a possible solar cycle dependence of the oxygen freezing-in temperature, in Figure 4.5 the temperature inside magnetic clouds with respect to sunspot number is shown. The sunspot number taken for each event represents the averaged monthly value of the month in which the magnetic cloud was detected (sunspot data courtesy SIDC, RWC Belgium, World Data Center for the Sunspot Index, Royal Observatory of Belgium). Figure 4.5 shows that the high temperatures inside magnetic clouds appear at all phases of the solar cycle. There seems to be no apparent dependence of the OFT level with solar activity.

However, as stated above, clear dependences between temperatures and solar cycle phase are difficult to confirm, mainly due to the bias imposed by the Ulysses orbit.

The error bars in the figures denote only the standard deviation as a measure of the statistical error, the instrumental error is not considered. For a detailed analysis on systematic measurement errors for the SWICS instrument, the reader should consult von Steiger et al. [2000].
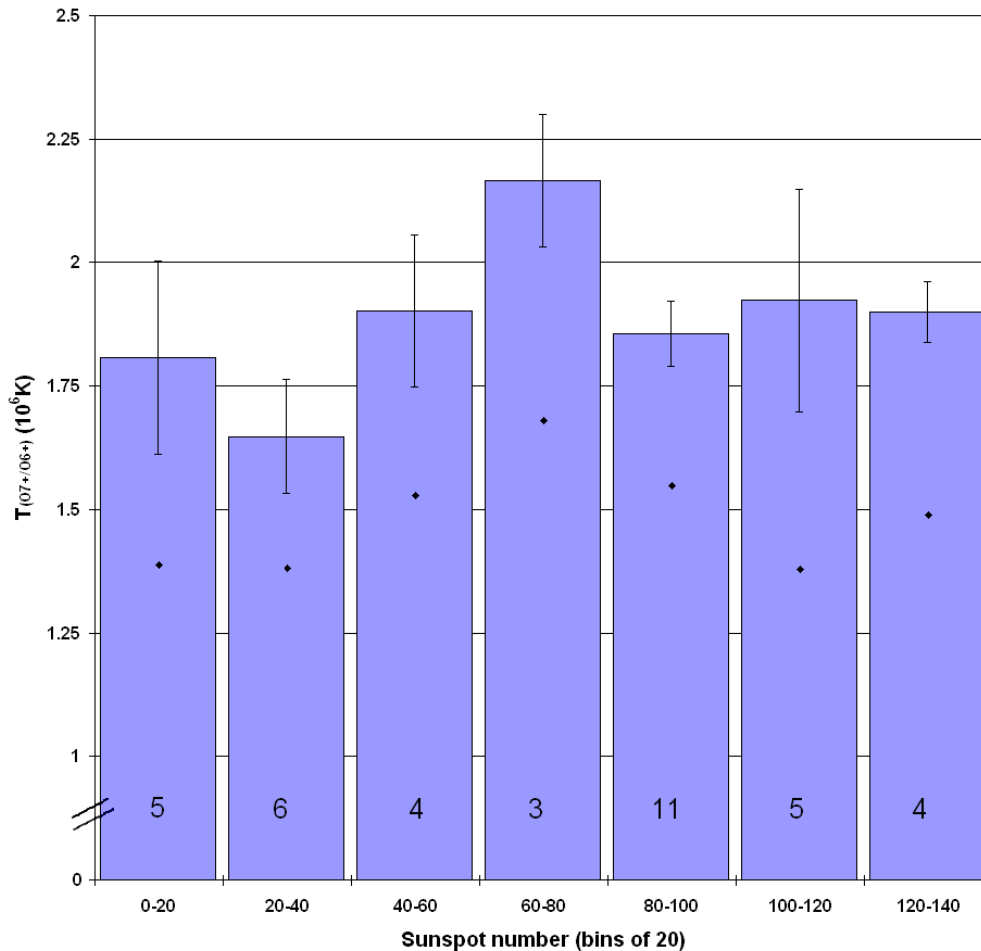
Figure 4.5. Distribution of freezing-in temperatures inside MCs and in the neighbouring solar wind (dots) vs. sunspot number. The numbers in each bar represent the number of MCs used for its calculation. From Rodriguez et al. [2004].

4.2.3 OFT as a solar wind type identifier

Following the results from Fenimore [1980], von Steiger et al. [2000] analysed different types of solar wind flows in relation to their freezing-in temperatures (or charge states) distributions of heavy ions. They concluded that charge states represent a very good indicator of the solar wind type, providing a robust tool for differentiating fast wind (from coronal holes), slow wind (associated with streamers) and transient-related solar wind. In this section a direct comparison will be provided.

Figure 4.6 was created to show the distribution of OFT for slow and fast solar wind, non-cloud ICMEs and MCs. A Gaussian fit is applied to each curve. For comparison, the fit corresponding to the slow solar wind is repeated in the other panels. The magnetic clouds are the events listed in Table 3.1. Non-cloud ICMEs are all the events obtained from the Ulysses ICME list, maintained by the SWOOPS instrument team, excluding the MC events of Table 3.1. The solar wind samples were selected from several periods in

different years of the Ulysses mission. Special care was taken in order to include only periods in which no transient events were present.
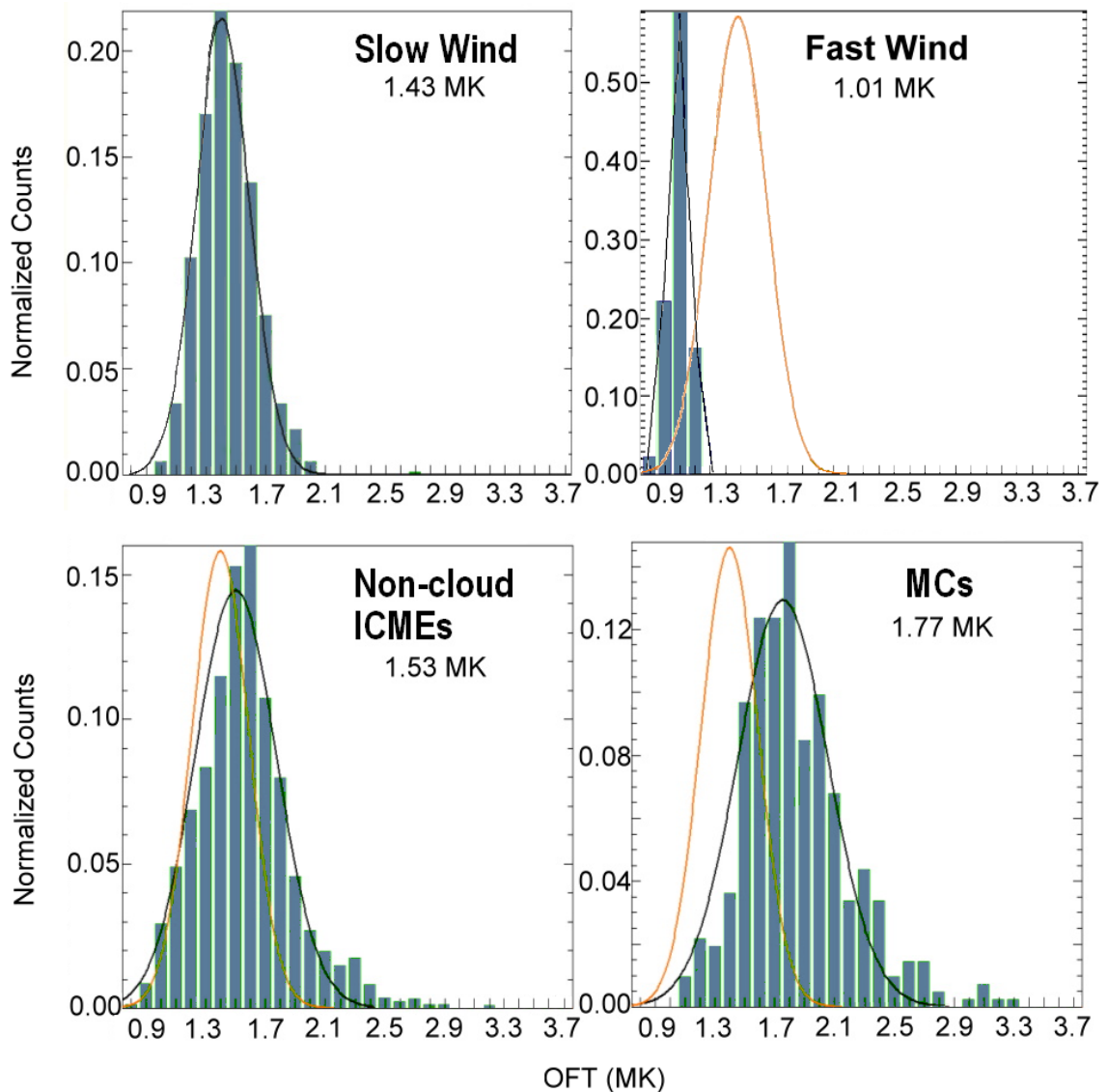
Figure 4.6. Histograms of oxygen freezing-in temperatures (OFT) for slow, and fast solar wind, MCs and non-cloud ICMEs. In black, a Gaussian fit to the individual distributions is shown. In orange, the scaled Gaussian fit to the slow wind is repeated for comparison.

The values of the oxygen freezing-in temperature (OFT) shown in the plot are those obtained as the center of the Gaussian. Between slow wind and MCs there is a difference of 0.34 MK (approximately 2 times the standard deviation, σ, of the slow wind, σ_{sw} = 0.18), whereas between slow wind and non-cloud ICMEs this difference reduces to 0.1 MK (less than one σ_{sw}).

Whether all ICMEs have elevated charge states or whether there are increases in some singular cases has been discussed recently. Galvin et al. [1997] found only a fraction of all investigated CMEs as containing high freezing-in temperatures. Henke et al. [1998] found that in low latitude MCs, high charge states are normally found. The result

presented in Figure 4.6, provides a direct comparison between ionization states in MCs and ICMEs detected at all latitudes and phases of the solar cycle. Probably the most important conclusion to be drawn from this analysis is that the difference with respect to the slow wind is three times higher in flux rope type ICMEs compared to the difference in those without magnetic cloud signatures. This statistical comparison clarifies that the enhancement in freezing-in temperatures is significant for MCs (approximately 2 σ_{sw}). The OFT in non-cloud ICMEs is possibly enhanced but to a much less extent (less than one σ_{sw}).

With the results presented here, it can be stated that charge states for each particular case, provide a complementary in-situ tool to differentiate MCs from non-cloud ICMEs and quiet solar wind.

4.3   Relation between oxygen and other ions

Using the same procedure as described in Section 3.2, the freezing-in temperature for carbon (CFT) was calculated, based on the ratio of C^{+5}/C^{+4}. For iron a different approach was undertaken, primarily because the SWICS dataset used here does not provide measurements for different iron ions. The iron data are represented by a single average charge state value. Based on this information, the iron freezing-in temperatures can be obtained according to Table 5 from Arnaud and Rothenflug [1985], which contains the corresponding freezing-in temperatures for a given average charge state of iron.

In general, magnetic clouds show increased iron and carbon freezing-in temperatures. Increased Fe charge states had been already reported by Lepri et al. [2001] and Lepri and Zurbuchen [2004]. By comparison with the oxygen results as provided in the previous section, the analysis of the individual events shows that the profiles corresponding to the different ions do not correlate exactly. Furthermore there are cases in which only one of them is enhanced. As an example, in Figure 4.7 a MC recognized by the clear rotation in the magnetic field elevation angle (θ) and a low plasma beta is shown. In this case, the profiles corresponding to C^{+6}/C^{+5}, O^{+7}/O^{+6} and the average charge state of iron are displayed. It is clear from the figure that the various ions behave differently, the temperatures inside the MC have been pointed out for comparison. While oxygen increases in the center of the structure and reaches 2.3 MK, carbon enhancements are not clearly seen until the end of the event, and they remain close to 1.5 MK. Iron, on the other hand, does not show a particular enhancement and there are no clear differences from the surrounding solar wind. The differences seen for this example are also seen in many of the remaining events. They are most probably due to the fact that different elements freeze-in at different altitudes. Therefore the profiles of O, C and Fe indicate that the internal structure of the CME has evolved significantly only in a few solar radii from its origin.
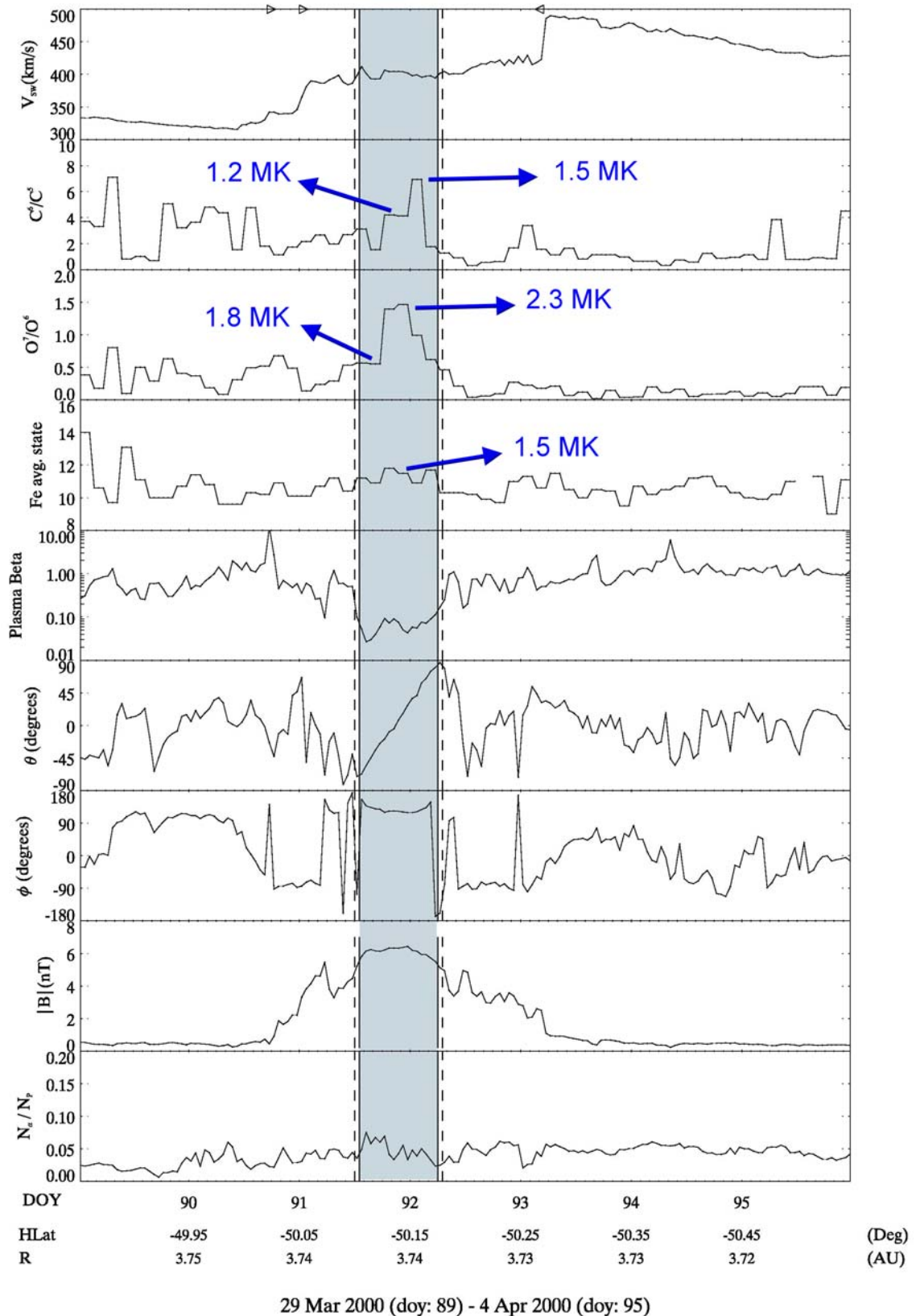
Figure 4.7. A MC detected at 50° southern latitudes. The remarkable rotation in the magnetic field is accompanied by a non-homogeneous behavior of the ionization ratios of O^{+7}/O^{+6}, C^{+6}/C^{+5} and the average charge state of iron. The arrows on top mark the passage of forward (right directed arrows) and reverse (left directed arrow) shocks.

Mainly two points will be investigated further:

- The behavior of the different ions in MCs and possible relations between them.
- The relation between the solar wind preceding the cloud, in the cloud, and that following the cloud.

Each MC, including the surrounding solar wind was divided in 5 periods, in the following way:
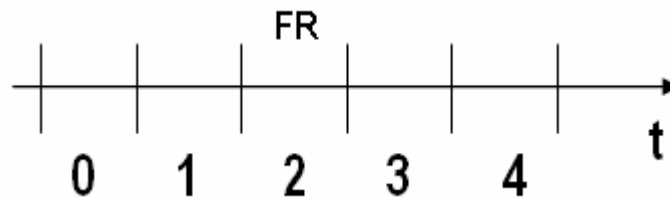
0: solar wind before the MC

1: solar wind immediately before the MC

2: MC itself (FR = flux rope)

3: solar wind immediately after the MC

4: solar wind after the MC

Each of the five periods is determined separately for every event of Table 3.1. The starting point is Period 2, its boundaries correspond to the magnetic cloud itself. Period number 0 commences with a certain separation with respect to the flux rope interval (Period 2). This separation is calculated in order to include what might be the leading edge of the CME, as seen in coronagraph images (Figure 1.7). There is no precise information available on how the different parts of a CME, evolve as they travel through the heliosphere. Therefore for this work, the beginning of Period 0 was calculated allowing a solar wind speed difference of 150 km/s with respect to the average speed inside the flux rope. In this way, using the distance from the Sun at which the MC was detected and the two speeds (the first as the average corresponding to the flux rope and the second one 150 km/s faster), the time at which Period 0 starts is calculated. According to Srivastava et al. [1999], a value of 150 km/s appears to be a good proxy of the speed difference between leading edge and kernel of the CME. The flux rope is normally believed to be accommodated between these two structures (Plunkett et al., 2000). The interval between the start of Period 0 and start of Period 2 is divided into two intervals, the first corresponds to Period 0 and the second is Period 1. Period 3 and 4 are obtained by simply mirroring periods 1 and 2 on the other side of the MC. In summary, there are 5 periods, 2 in the upstream solar wind region, 2 in the downstream region and 1 that includes only the MC.

The scatter plots in Figure 4.8 compare freezing-in temperatures of oxygen (OFT) and iron (FeFT) for each period. Here, not all events from Table 3.1 are included, but only those which are immersed in slow solar wind. Since the analysis comprises solar wind

from outside the MC period, it is important not to mix fast with slow wind (see Section 4.2.1). The OFT outside the MC (i.e., plots number 0,1,3,4) are concentrated around 1.5 MK, in agreement with Figure 4.6. In the flux rope period (plot 2), the points spread towards much higher temperatures. Iron represents in every plot lower temperatures than oxygen.
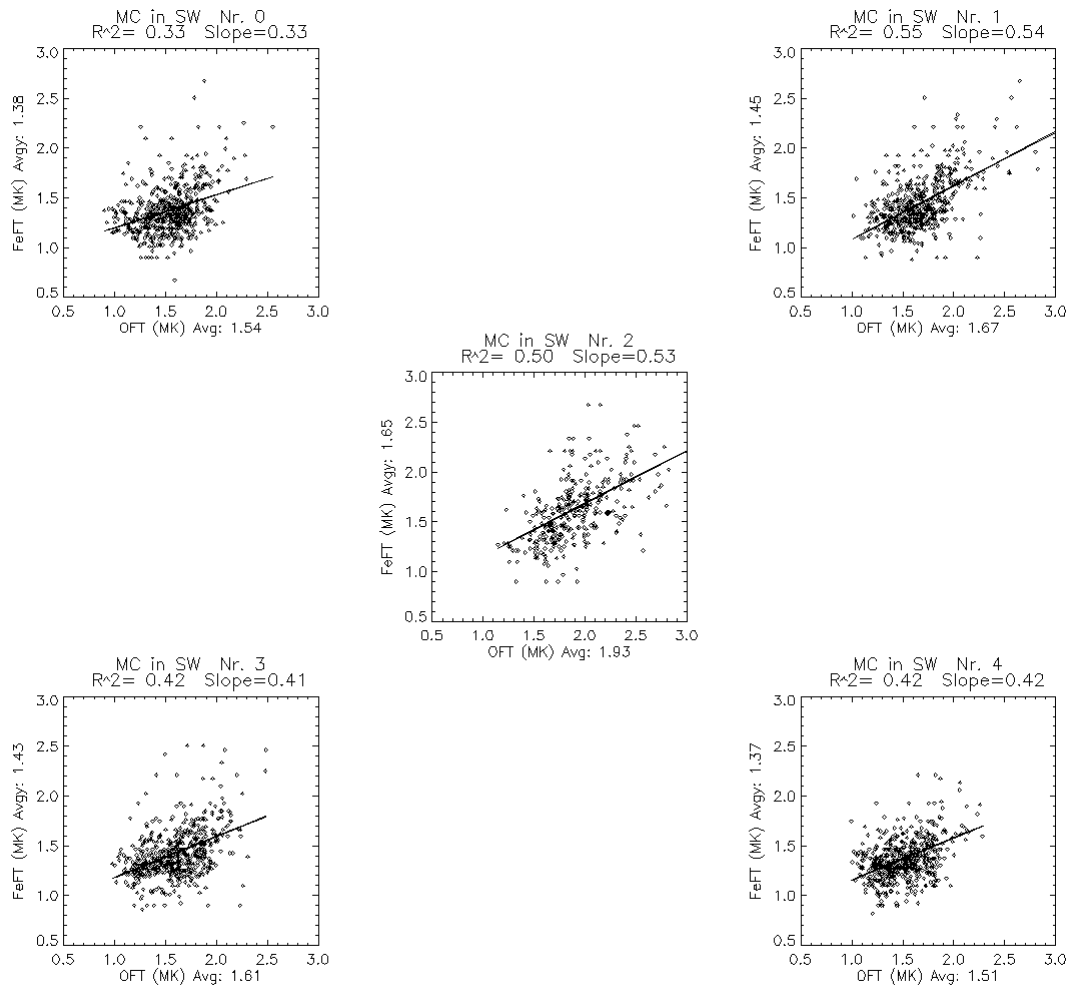
Figure 4.8. Scatter plots of iron vs. oxygen freezing-in temperatures. The 2 plots on top, number 0 and 1, show periods before the MC. Plots 3 and 4 represent periods after the flux rope. Plots 0,1,3 and 4 are equally divided. Plot number 2 is sampled directly inside the MCs. Each point in the plots represents a SWICS measurement, averaged over 3 hours. The line is a linear fit to the data. R^2 is the correlation coefficient.

The data used for plot 0 were taken in front of the flux rope, those in plot 4 at a similar distance behind the flux rope. They are comparable, regarding average temperatures and distribution of the points. On the other hand, plots 1 and 3, which are also symmetric with respect to the flux rope, show different features. Plot 1 is more comparable with plot 2, the high temperatures seem to leak out of the MC region towards the leading part. The lower temperature range (around 1.5 MK in OFT) is similar for plots 1 and 3, only in the high temperature range is where they differ.
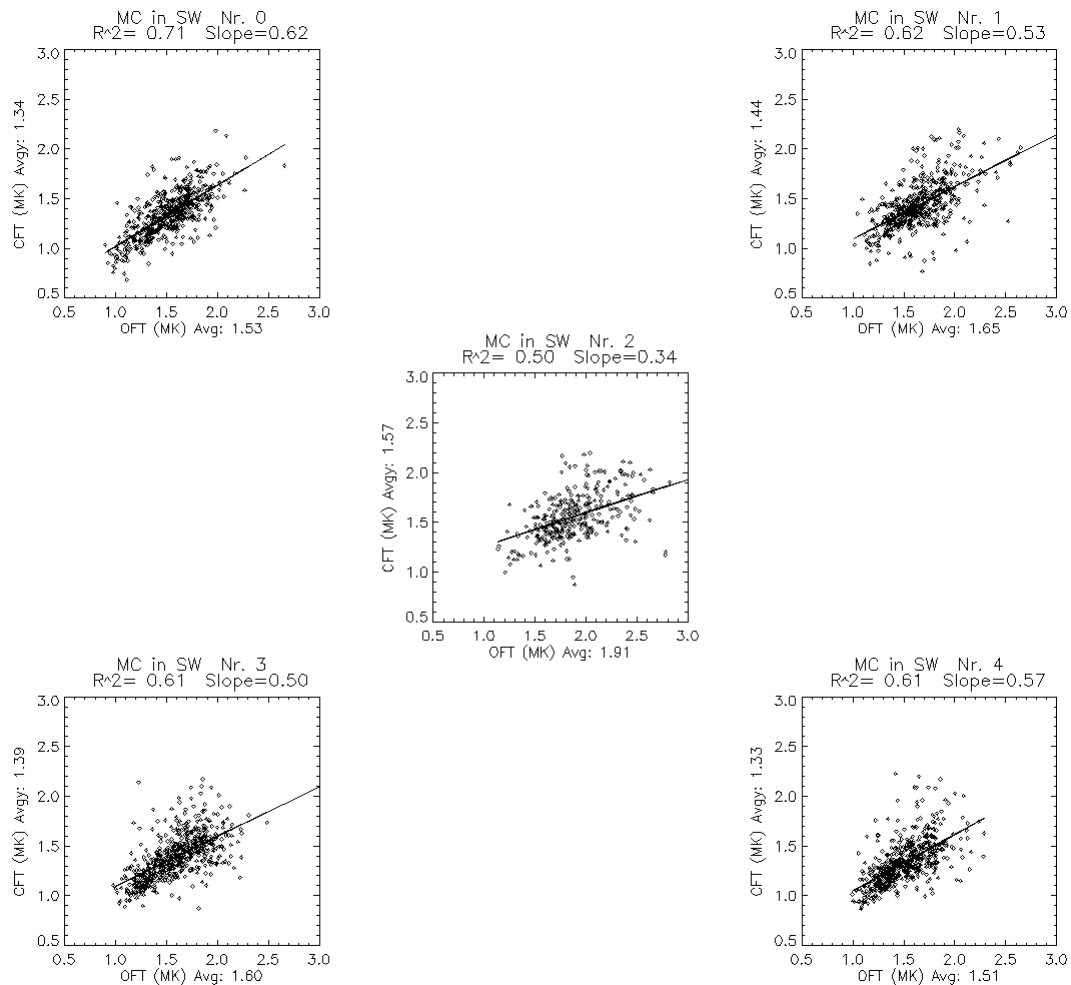
Figure 4.9. Same as Figure 4.8, but for carbon vs. oxygen.

In Figure 4.9 a similar analysis, but comparing carbon freezing-in temperatures (CFT) with OFT, has been carried out. Oxygen freezing-in temperatures in the X-axis should be the same for each period in both Figure 4.8 and Figure 4.9, the small differences arise due to bad data occurring at different times in iron and carbon, which doesn't allow exactly the same points to be used in both figures.

Outside MCs, the correlation between these two elements appears to be better than between oxygen and iron. It is worth noticing that the correlation and the slopes are always higher outside of the flux rope region (i.e., plots 0, 1, 3, 4) than inside. Furthermore, the slope of the linear regression is higher in plots 4 and 0, the furthest away from the MC region. These findings point toward a break in the correlation between oxygen and carbon for high temperatures. In any case, for carbon the increases in freezing-in temperature in the flux rope region are again present.

By comparing the results before with those after the flux rope, one can address the possibility that a 3-part structure persists in interplanetary space (see Section 1.2.1). If such structures were to be detected in charge state distributions then one would expect to see populations before and after the flux rope which deviate from the normal trend. For example a clustering of low charge states seen before the flux rope passage and not

reappearing afterwards may be a good indication. Nevertheless, in the results showed here there is no indication of such behavior. In a different approach, a case study was undertaken in order to identify possible individual events which were unnoticed in the previous statistical analysis. Again the visual investigation of the single events resulted in zero positive cases. There are no distinctive structures detected at one side of the flux rope which did not appear on the other side. The presence of different solar wind structures on both extremes and inside the flux rope can definitively not be inferred. No signs of a 3-part structure have been found for interplanetary CMEs. Nevertheless, the leading part seems to present higher temperatures than the trailing part. Since neither in this study nor in previous, a 3-part structure was identified in interplanetary space it can be concluded that the this is a feature most probable lost close to the Sun. The different parts may be moving with respect to each other and finally merge.

With Figure 4.8 and Figure 4.9 it has been shown here that for the three ions studied (C, O and Fe) the freezing-in temperatures are increased within the central period containing the flux rope. Oxygen, with an average increase of 0.38 MK (between period 0 and period 2), is the one which experiences the highest differences (iron 0.27 MK and carbon 0.23 MK).

4.4   Freezing-in temperature maps

It was established in Section 4.2 that increases in oxygen freezing-in temperature (OFT) occurred in more than 90% of the magnetic clouds encountered by Ulysses, with a 26% average increase between OFT inside the clouds and the surrounding solar wind. Figure 4.6 shows that this is a characteristic behavior for MCs but not for non-cloud ICMEs. When the cloud structure is not present, the increases tend to be lower. Since OFT is a characteristic quantity which is defined at a few solar radii from the solar source, its relation to the magnetic structure is non trivial. The ionization levels of the different ions depends heavily on the magnetic field structure present in the source region (see e.g. Zurbuchen et al., 2002), plasma within closed magnetic loops will be heated to higher temperatures than that which moves along open field lines. The change in OFT between slow and fast wind (Figure 4.6) could be compared with the difference in cloud and non-cloud ICMEs, in the sense that this difference arises from a difference in the magnetic configuration in the source region of the corresponding solar wind. Since the freezing-in temperature does not change in interplanetary space and MCs show in general higher freezing-in temperatures than non-cloud ICMEs, then a difference in the source magnetic structure rather than interactions occurring further out would be the most plausible explanation.

One should not rule out a second possibility, involving a geometrical consideration. A flux rope may always be present in ICMEs, but it is only detected when the spacecraft samples the ICME close to the center. To explore this possibility the optimum approach

would be a statistical study of multipoint measurements, providing a grid of data points allowing a reconstruction of the actual global structure of single ICMEs. Since this possibility is not viable at present, the observer has to find a way to reproduce the geometric shape of an ICME, created from a 1-D cut through the structure, i.e., from one satellite in-situ measurements. Several models that approximate the topology of the magnetic field from the measured values have been used for this purpose (Section 3.4). It is worth noticing, though, that these models are based on the analysis of the magnetic field configuration in a flux rope. Therefore, only MCs can be modelled in this way. Non-cloud ICMEs posses no characteristic magnetic field configuration (i.e., no rotation in the magnetic field angles, no twisted helical field lines) and cannot be modelled in a similar way.

In this work, a modified version of the elliptical model from Hidalgo et al. [2002b], described in Section 3.4, is used. One of the parameters obtained after fitting the data with this model is the angle between the spacecraft path inside the MC and the flux rope axis (henceforth in this section, called attitude angle). The meaning of this angle with respect to the spacecraft path through the cloud is enlightened in Figure 4.10, for the cases of 0° and 90°. Probably one of the major limitations in using this kind of models is that the parameters they provide are local. For example the straightforward interpretation of a 0º attitude angle is the one shown in Figure 4.10, a cut through the flank of the flux rope. An attitude angle of 0º may also mean that the MC is traversed at any other place different from the flank, but there are deformations in the local magnetic field which let, locally, the axis be oriented parallel to the spacecraft path.
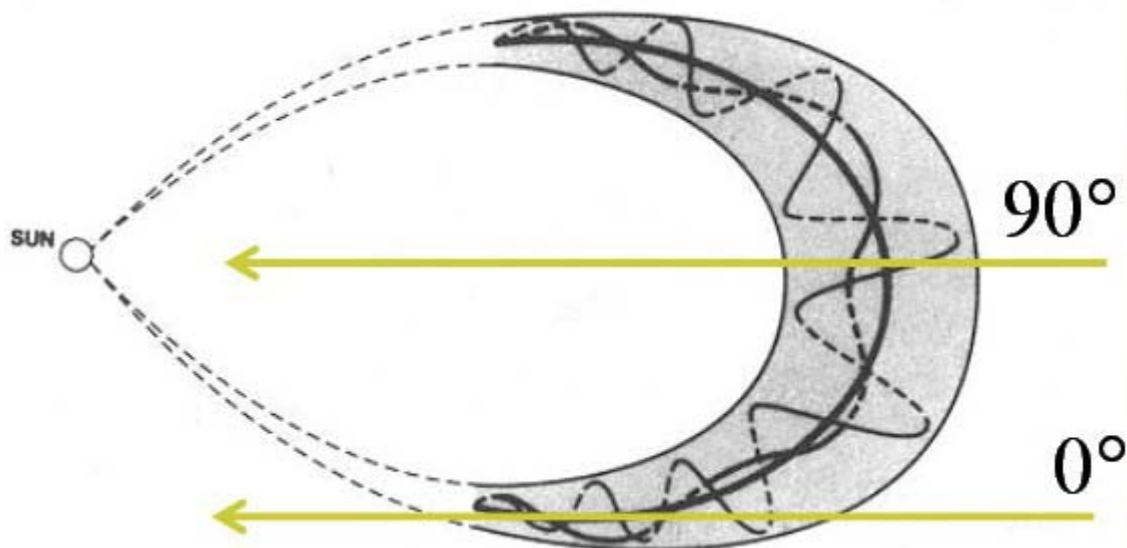
Figure 4.10 Attitude angle between the spacecraft path in the MC and the flux rope axis. Base image adapted from Burlaga et al. [1990].

The MC events from Table 3.1 have been fitted with the model described. Next, the events have been classified according to the obtained attitude angle. Two events have been left out due to missing data. In Figure 4.11, each MC has been ordered in the Y-

axis according to its attitude angle, mirrored when necessary to the first quadrant, i.e., an angle of 110º is used as 70º. This change is justified since the interesting point is to study any dependence on the actual attitude angle from a 0º or a 90º cut. The variable termed 'time' on the X-axis corresponds in principle to SWICS measurements of oxygen charge states, with a data cadence of 3 hours. Therefore each horizontal line in the plot represents a single MC. Of course not every attitude angle was obtained from the model. To obtain a complete surface, first the data were triangulated (Delaunay triangulation) and then interpolated. Not all the MCs have the same duration: in the plot the dashed lines represent the average MC duration. Then each event has been resampled by linear interpolation of the values (only in X-direction), in order to accommodate to the average size. Time to the left of the flux rope limits means leading solar wind and time to the right contains trailing solar wind. The boundaries have been selected for the calculation in the X-direction allowing a 150 km/s speed difference from the flux rope averaged velocity (forward and backwards, as it was explained in Section 4.3). In contrast to the previous section, the period of time has not been divided into 5 regions, but only into 3. One period for the flux rope itself, one before and one after it. Hence, regions 0-1 and regions 3-4 from Section 4.3 have been merged. Finally, an average duration for each period has been calculated, among all the events, and each event is scaled to this average. In this way, a comprehensive view of the internal profile of different ions in MCs can be given.
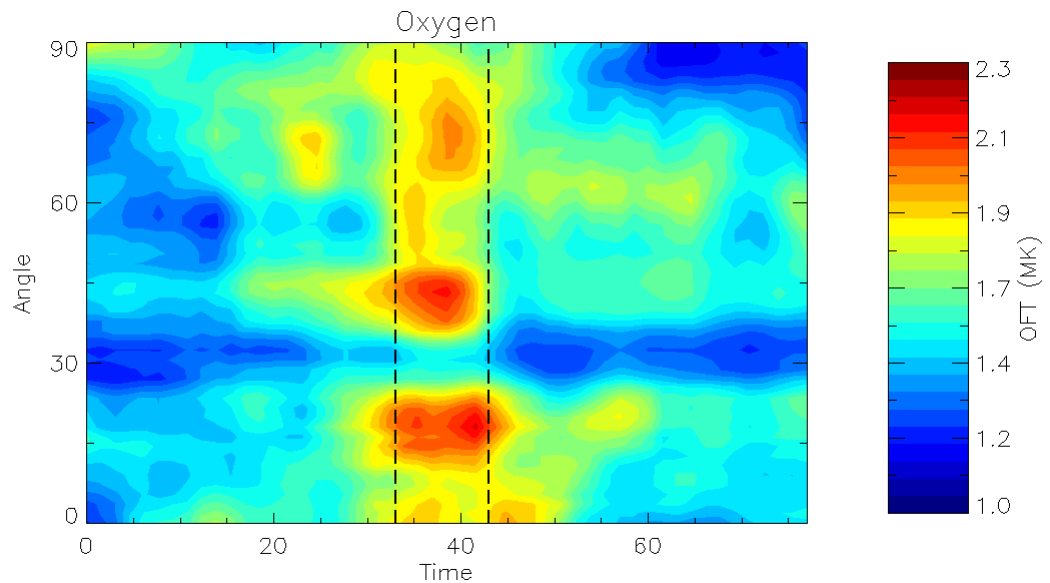
Figure 4.11. Filled contour plot showing MCs from Table 3.1; ordered by attitude angle (see text) in the Y-axis and 'normalized' time in the X-axis. Color represents oxygen freezing-in temperature. The dashed lines represent the average flux rope size.

Figure 4.11 again corroborates the results exposed in the previous sections: elevated temperatures are highly confined to the flux rope region. On the other hand, there is no clustering of high temperatures close to 90º as it would have been expected, high temperatures are also detected at the flanks. If one believes that ICMEs would retain

their fairly symmetric shape (Figure 1.7) seen in coronagraph images, then the core of the CME would be at its center (attitude angle of 90°) and there is where the highest temperatures would then be seen. However, this is not the case. At low angles, the high temperatures appear more spread and not as well confined as at higher angles, but they are definitely present. This represents another indication that ICMEs undergo significant deformation as they travel through space.

In Figure 4.12, the location of the OFT peaks within the flux rope region are shown. To create this plot, the position and duration of the maxima in OFT for each event were determined. Then each event was visually analysed in order to check for relevance (duration, repetition) of the values previously found. The position is given by the time elapsed from the beginning of the event in % of the total duration. Thus, the start of the cloud is denoted by 0%, while 100% marks the end of it. The total length of the interval corresponds to the period within the dashed lines in Figure 4.11.
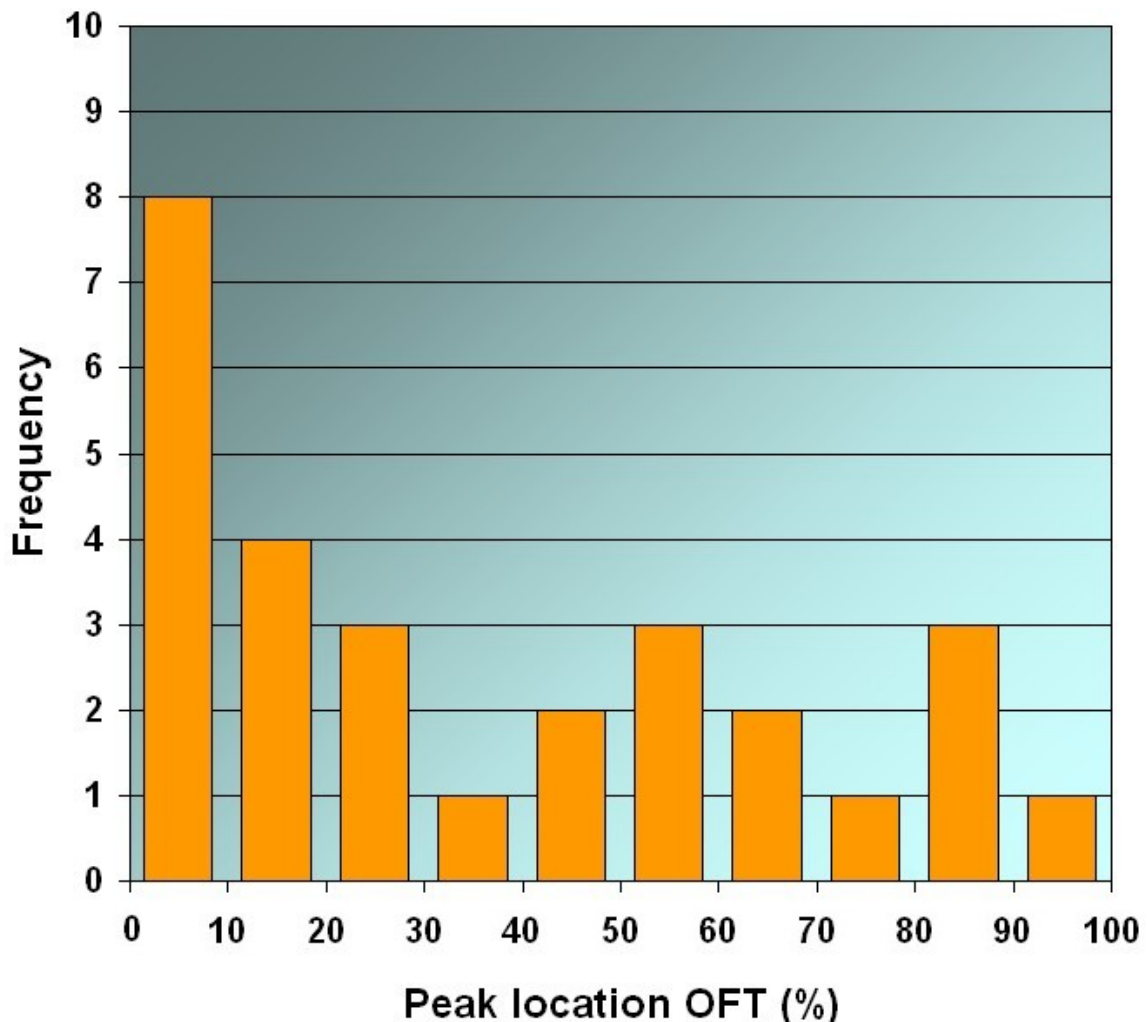
Figure 4.12. Location of peaks in OFT, inside MCs. 0% is the leading part of the cloud, 100% is the end of it.

The maxima in OFT are occurring most frequently close to the commencement of the flux rope and not close to its end. These results hold independent of the attitude angle

between spacecraft trajectory and flux rope axis.

If one considers the ideal cases from Figure 4.10, ICMEs containing flux ropes can also be identified when the structure is sampled only through a flank. Since there is no way of applying a similar analysis to non-cloud ICMEs (due to the absence of a flux rope), the same cannot be said for them. Therefore there is no sufficient evidence to favour any of the explanations for the flux rope presence in ICMEs. The geometric problem cannot be ruled out, due to the lack of geometrical information on non-cloud ICMEs. Whether the flux rope presence is determined in the source region or in interplanetary space is again difficult to prove since it is obvious that ICMEs undergo large deformations in space. These changes would not affect the ionization state of the individual solar wind ions, since they are frozen-in. Nevertheless the solar wind parcel may deform to such extent that the ions will be highly scattered and spread. Clusters of high temperature might be smeared out by these processes.

In Figure 4.13 a schematic illustration of the OFT distribution from Figure 4.11 is displayed within a highly idealized flux rope representation.
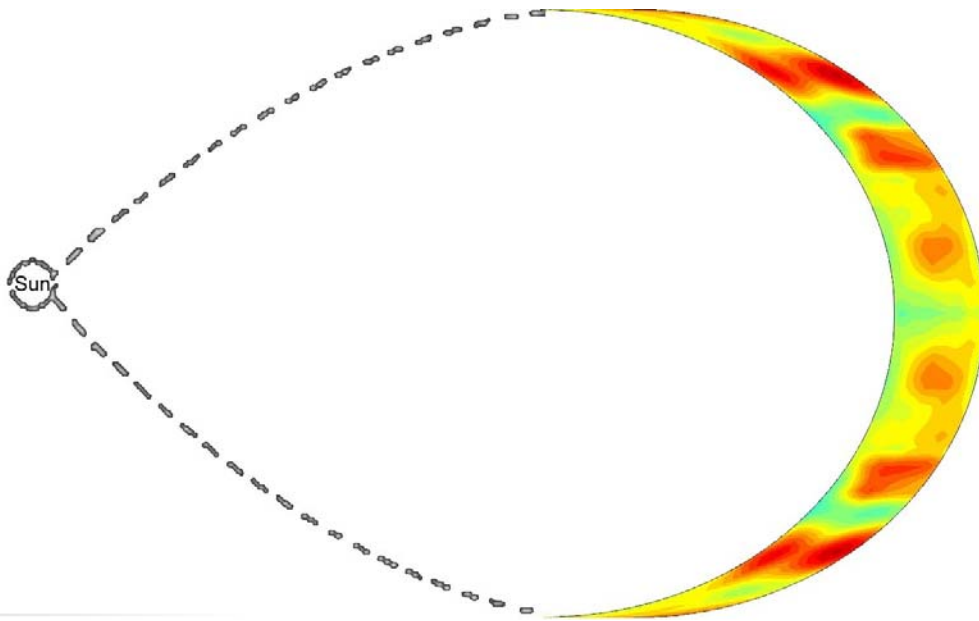
Figure 4.13. Temperature map of an idealized ICME, made by overlaying the flux rope region of Figure 4.11 in the schematic representation of Figure 4.10.

Figure 4.13 was constructed from many different events, using local parameters provided by the flux rope model and the shape is a highly idealized one. Therefore it should only be considered as a means of illustration. Notice that the values for the second half of the structure have been mirrored from the first one.

Different elements freeze-in at different heights in the corona. This separation in height allows to study at which height the heating experienced by the plasma is larger. Figure 4.14 contours temperature profiles, such as the oxygen one from Figure 4.11, for iron and carbon. In order to facilitate a comparison, the same color scale for all these elements has been used. Thus the colorbar is optimized for the OFT range, and therefore

variations in CFT and FeFT appear less striking. The absolute values for iron should be considered with care, since the SWICS instrument onboard Ulysses measures iron charge states only up to 16.
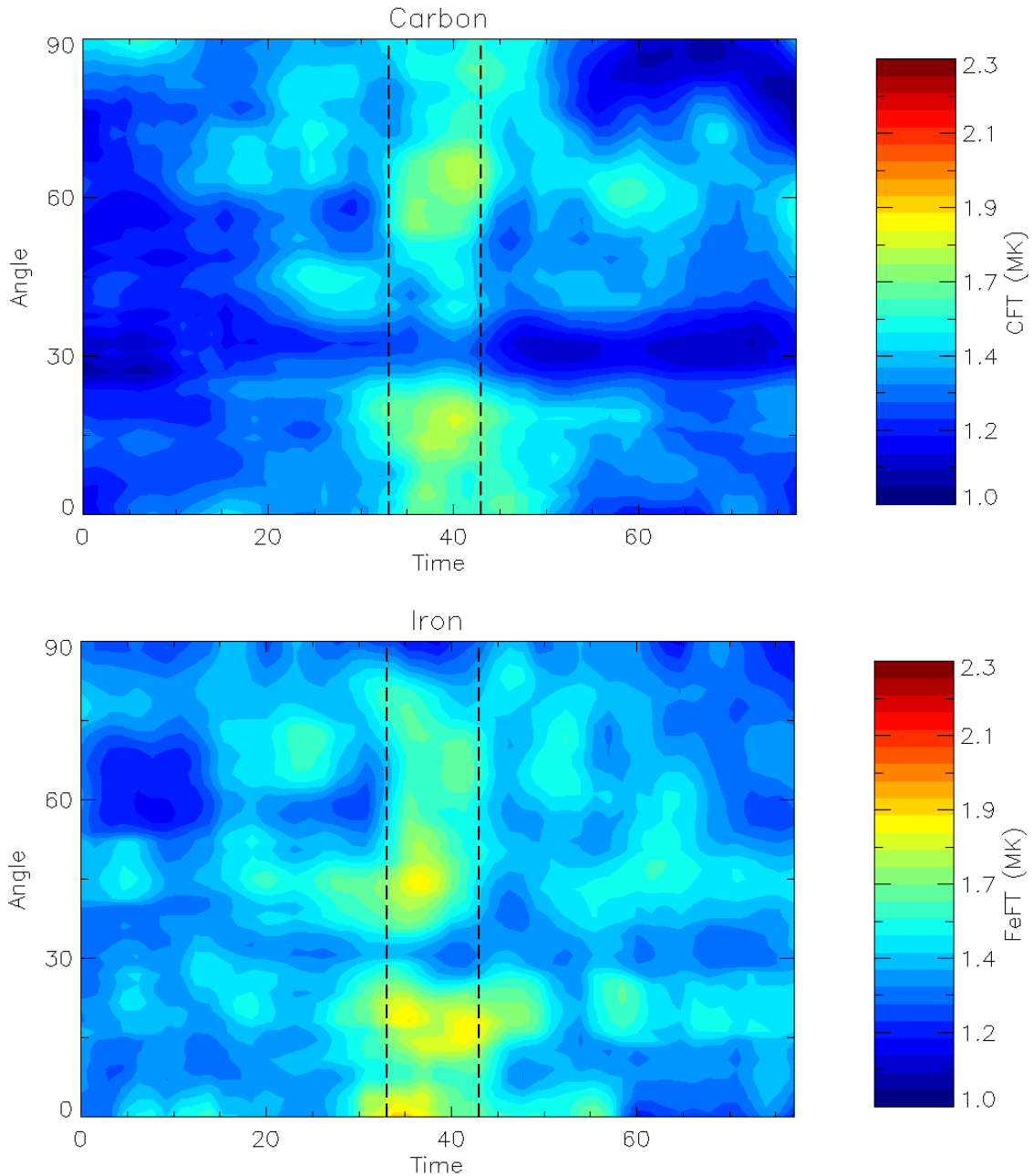
Figure 4.14. Same as Figure 4.11, but using carbon (top) and iron (bottom). The same color scale from Figure 4.11 has been used, for comparison.

High temperatures deduced from carbon and iron show a similar confinement to the flux rope region, as the one seen for oxygen. Differences in the profiles are present, pointing towards a distinctive temperature history of MCs in the low corona. The processes heating the plasma seem to act differently as the CME rises. The profile for oxygen shows larger differences with the surrounding solar wind when compared with carbon

and iron (as stated in the previous Section). The oxygen freezing-in temperature is the one that marks best the presence of a magnetic cloud when compared to iron and carbon. Therefore it can be deduced that it is at the oxygen freezing-in height (~1.5 R_s) where the CME plasma is most efficiently heated.

Chapter 5   Energetic particles and ICMEs

Energetic particles can be used to enlighten different points regarding ICME topology, internal structure and connectivity. They represent another useful parameter to characterize MCs in interplanetary space. By analysing the particle fluxes, conclusions can be drawn on the processes acting on them. Their elemental abundances provide information on the origin of the particles. Each acceleration mechanism favours certain elements. Directional information can be used, among other topics, to infer magnetic topology. These tools will be applied in this chapter to magnetic clouds.

5.1 Introduction

The magnetic structure of ICMEs normally acts as an obstacle for galactic cosmic rays (GCR). GCR fluxes are usually depleted during the passage of ICMEs (Barouch and Burlaga, 1975). At lower particle energies, the picture emerging from the observations is less clear. Kahler and Reames [1991] found several cases of enhancements in MeV ions and electrons produced by solar energetic particle events (SEP events) within magnetic clouds observed with the ISEE 3 spacecraft. On the other hand, Bothmer et al. [1996] found a magnetic cloud observed by Ulysses in which a strong decrease in the 1-3 MeV ion flux was observed. A loss of magnetic connection to the Sun was proposed as an explanation for this case. A comprehensive study of energetic ions in the energy range below 1 MeV was performed by Mazur et al. [1998]. In that study 13 magnetic clouds were studied with the Wind spacecraft, finding impulsive flare ions within 4 of them and depleted or constant energetic particle fluxes for the rest. The energetic particle intensity characteristics of the 40 magnetic clouds from Table 3.1 will be investigated in Section 5.2.

Early observations (Morrison, 1954; Gold, 1959) suggested the possibility that the footpoints of ICMEs are still connected back to the Sun as they expand and propagate in interplanetary space. More recently an explanation for such connection has been pursued

with in-situ data on bidirectional suprathermal electron flows (BDEs, e.g. Crooker et al., 1990), implying that this counterstreaming particles originate in the footpoints of the ICME still anchored back at the Sun. At higher energies, bidirectional fluxes similar to the ones seen for ~100 eV electrons were first reported by Rao et al. [1967] and have been more recently investigated by several authors (e.g. Marsden et al., 1987). For explanation of such behavior, again the presence of magnetic fields loops connected to the Sun is suggested. Other possible explanation for bidirectional flows, which cannot be completely ruled out, represents the presence of a locally closed structure (a plasmoid, see Figure 1.8 from Chapter 1).

Studies carried out for suprathermal electrons, at 1 AU have quantified the degree of bidirectionality within magnetic clouds. Shodhan et al. [2000] found BDE intervals covering 0% to 100% of the total duration of magnetic clouds, with 59% as average value. Less degree of counterstreaming fluxes was detected around solar minimum and the percentage declined with decreasing cloud size. A similar result (69% average of BDE intervals) was found by Riley et al. [2004]. By using a rich set of events, in Section 5.3 the degree of bidirectionality of MCs in the heliosphere will be estimated. Furthermore, the results obtained by other authors using suprathermal electrons will be compared with those obtained here based on near relativistic particles inside MCs.

Elemental composition in relation to ICMEs has been studied before (e.g. Tylka et al, 1999; Mazur et al., 1998). The composition of the energetic particles measured inside single events was used to derive the sources of the particles for the individual ICMEs. In this thesis, the dataset of 40 MCs will be used to compute a population of energetic particles which characterizes the events. In this way conclusions can be drawn on the dominant mechanisms by which particles in magnetic clouds are accelerated.

5.2 Intensity variations

The MCs events from Table 3.1 were analysed in search for differences in the energetic particle flux within MCs compared to fluxes present before and after cloud passage. Fluxes of helium (0.42-0.92 MeV/N), protons (0.57-0.77 MeV) and electrons (0.1-0.38 MeV, >0.18 MeV) were used.

The ion fluxes show markedly different responses from one case to the other. In general the variations in intensity have been divided into three cases (increases, decreases or no difference) by comparing the values found within magnetic clouds and in the surrounding solar wind. A variation in intensity is considered to be present only when the flux levels are modified by values higher than the statistical variation of the background. In the next three figures, an example of each case considering helium and proton fluxes will be shown. The electrons, in the majority of the cases, remained unaltered.

The first event, Figure 5.1, corresponds to a magnetic cloud encountered at 50°

heliographic latitude. Ulysses was travelling towards the north pole of the Sun, during its second fast latitudinal scan.

Figure 5.1. Increases in intensities of helium and protons during MC passage (top panels). The next panels show the solar wind speed, the plasma beta, the magnetic fields angles, its magnitude, and the proton temperature.

The cloud is, as usual, marked by the solid vertical lines. It can be identified by the rotation in the magnetic field angles, the depleted proton temperature and plasma beta. A marked increase in the proton and helium intensities is seen for this event, coinciding

very well with the MC boundaries. Since 1996, Ulysses had been immersed in slow wind streams. At these high latitudes, the formation of the northern polar coronal hole brought again high speed streams to Ulysses, alternating with the still prevailing slow wind. The background in which Ulysses was immersed was governed by changing conditions, with perturbances seen in the magnetic field data. Two shocks (arrows on the top panel of Figure 5.1) were identified in the vicinity of the event.

The second event, in which there is no apparent variation in the particle intensities, is shown in Figure 5.2.

Figure 5.2. No variations in the intensities of helium and protons during MC passage (top panels). The next panels show the solar wind speed, the plasma beta, the magnetic fields angles, its magnitude, and the proton temperature.

The MC in Figure 5.2 was detected at Ulysses when it was close to its orbit aphelion, at 5.3 AU from the Sun and close to the ecliptic plane (13° south). The rotation takes place from south to north (negative to positive θ angle), the magnetic field magnitude is moderate and stable. The plasma beta and proton temperature are not markedly depleted, for this case plasma and magnetic pressure were low. The cloud was travelling with the same speed of the solar wind and solely by its plasma characteristics it would have been difficult to identify. The magnetic field data and the elevated charge states (not shown here) provide the final signatures. In contrast to the previous case studied, the intensities of energetic helium and protons remained completely unaware of the cloud appearance, within statistical margins. Additionally to the low latitude of detection, the solar cycle was in its rising phase. Ulysses was completely immersed in a stream of slow solar wind with a high amount of ICMEs and MCs being encountered (see Table 3.1). As a consequence, the energetic particle background surrounding the event in Figure 5.2 was approximately one order of magnitude higher than the one present in Figure 5.1. The intensity of the particles associated with the cloud was probably not sufficient in this case to be seen on top of the already high particle background. Different background conditions, arising to latitude and solar cycle variations were proposed previously by Bothmer et al. [1995] to explain a similar situation.

Finally, a case with a decrease in energetic particle intensities is presented in Figure 5.3. The MC was detected in April 2001 by Ulysses during its second fast latitude scan at 25° south of the ecliptic. Streams of slow and fast solar wind are interacting in this region of the inner heliosphere, creating CIRs. The magnetic cloud, delimited by the solid lines, is clearly identified by the rotation of the magnetic field vector. Worth mentioning for this last case are the plasma signatures. The alpha to proton ratio (bottom panel) is extremely increased, indicating the presence of the solar ejecta. The iron charge states reach values close to 16, the maximum level that can be detected by SWICS. The oxygen freezing-in temperature is above 3 MK. This is the hottest magnetic cloud among all the events used in this work. The MC occurs in the fast wind region trailing a CIR, the shock seen in front of it is most probably not driven by the ICME but by the speed difference between the fast and slow wind producing the interaction region. The signatures of this MC are, regardless of the CIR presence, clearly discernable. Before the MC arrival, the energetic particle background at Ulysses was enhanced, most probably due to the passage of several shocks, shown as arrows in Figure 5.3. During the MC passage, the energetic particle helium and proton fluxes (top 2 panels) decrease, showing the lowest values in more than 20 days. There seems to be a two-step decrease, especially in the protons. The first decrease occurred shortly after shock arrival at Ulysses and it corresponds exactly with the commencement of the structure identified in the Ulysses ICME list. The second decrease correlates with the start of the rotation in the magnetic field, which was defined in Table 3.1 as the beginning of the MC. This last decrease seems to be better correlated with the arrival of the interplanetary flux rope. There is a clear differentiation between the period inside the cloud and the rest of the surrounding energetic particle background. The high energetic particle background (the highest among the 3 cases shown here)

surrounding Ulysses seems to be locally blocked by the cloud passage. This event, due to its magnetic field, plasma and energetic particle characteristics is an exceptional one and it will be further analysed in this chapter.
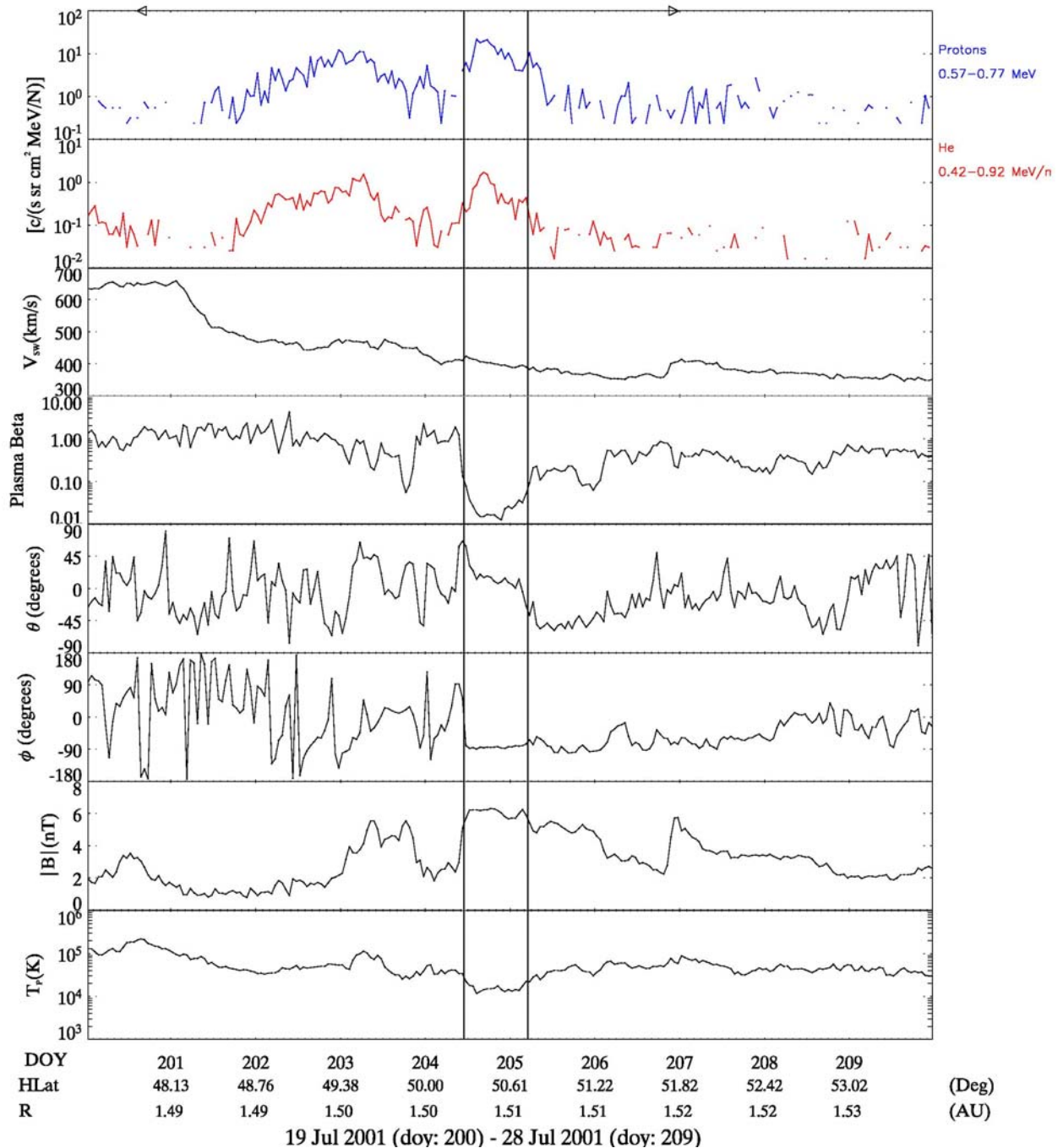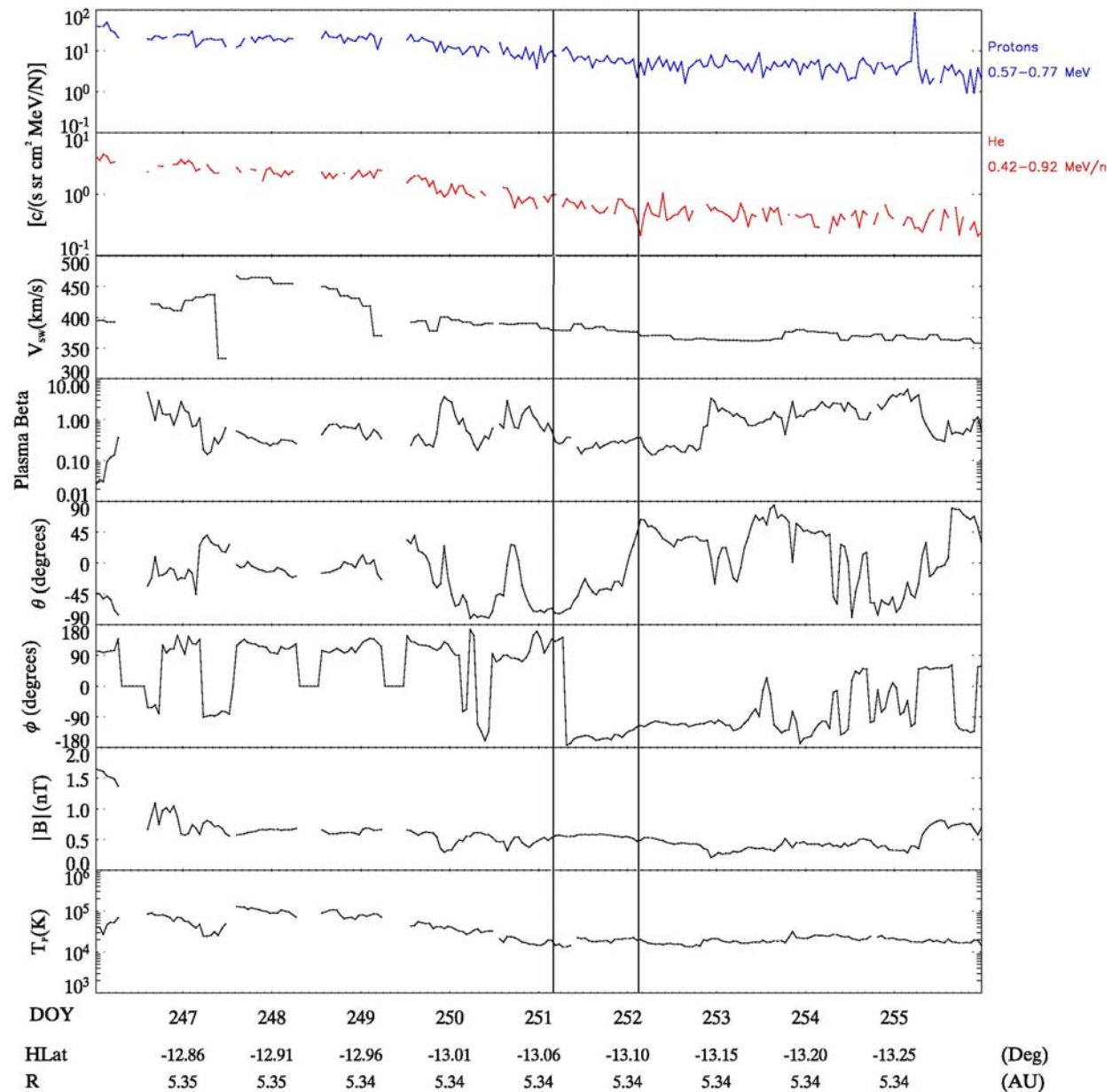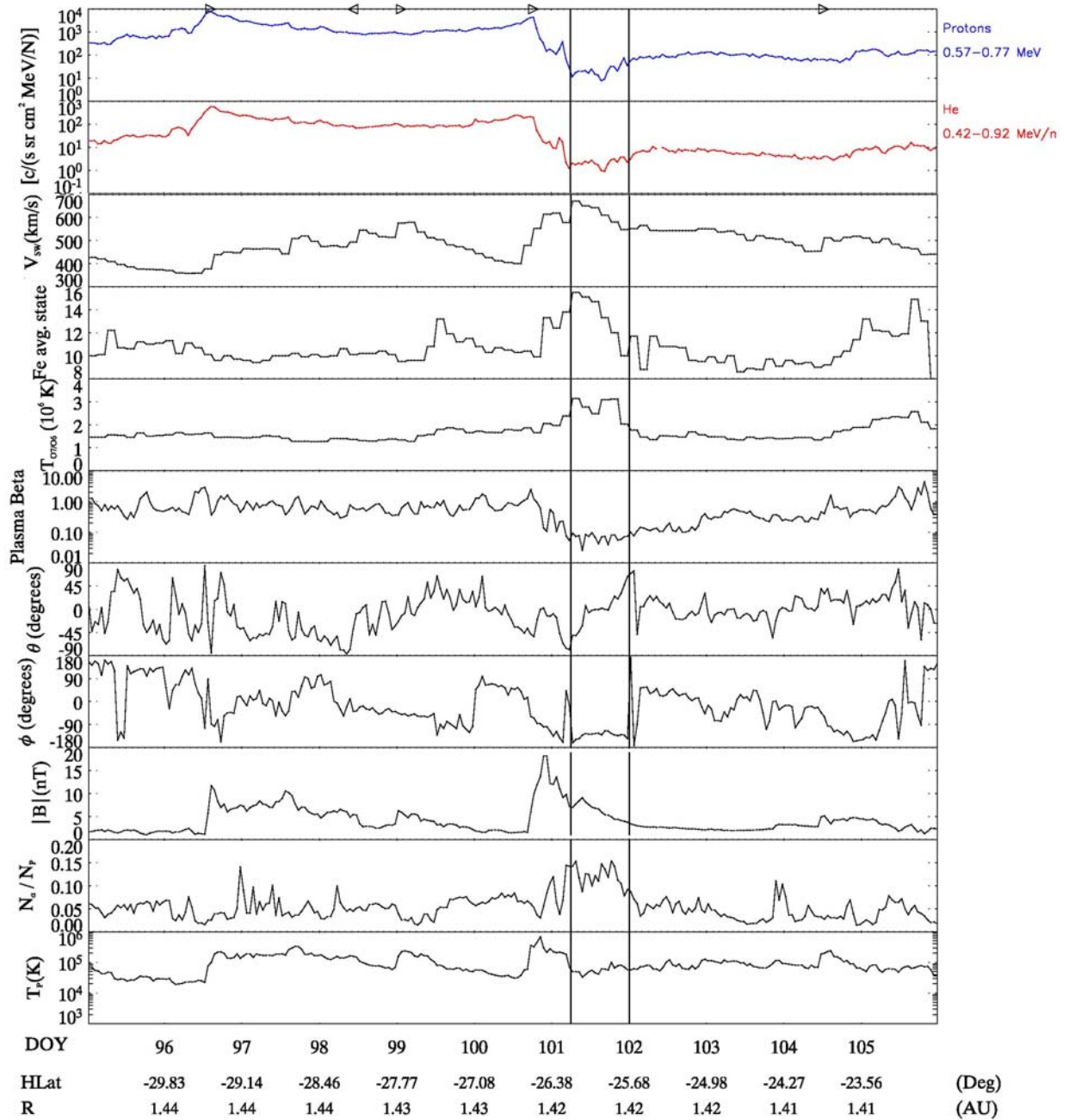

Figure 5.3. Decreases in the intensities of helium and protons during MC passage (top panels). The next panels show the solar wind speed, the average iron charge state, the oxygen freezing-in temperature, the plasma beta, the magnetic fields angles, its magnitude, the alpha to proton ratio and the proton temperature.

There exists no single behavior of the intensity of energetic particles in relation with magnetic clouds. Obviously it depends heavily on the conditions in which each event is immersed. In the majority of the events, for both species, the flux level remained approximately constant. Increases and decreases were less often observed. Figure 5.4 resumes these results. It is worth noticing that in only a few cases, the variation in flux intensity was higher than one order of magnitude.

	Decrease	Increase	No difference
Protons	16.7	13.9	69.4
Helium	17.9	12.8	69.2
Electrons	5.0	2.5	92.5
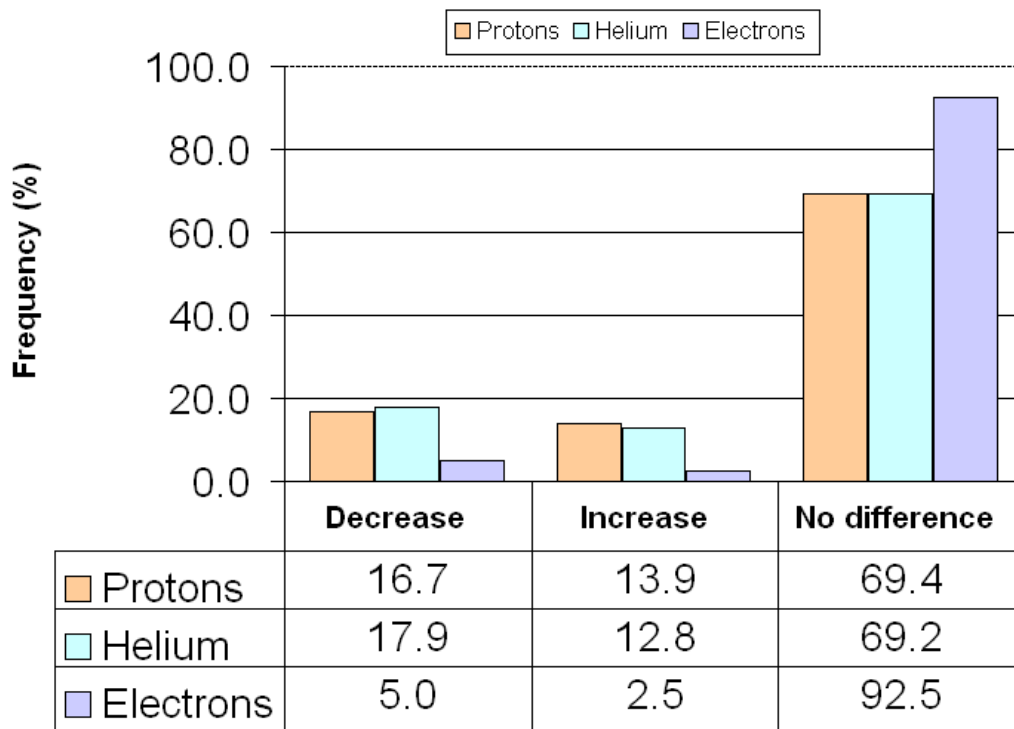
Figure 5.4. Distribution of the helium, proton and electron intensity variations within magnetic clouds with respect to the surrounding particle background (relative occurrence in %).

No clear connection between the energetic particle flux behavior and solar activity (measured by the sunspot number) or latitude of detection could be established, since the different responses were observed at all latitudes and solar cycle phases. Nevertheless, as it was mentioned above, the particle background (which depends on latitude and solar activity) present at Ulysses before cloud arrival may play an important role. In this way, the strongest increases are present at higher latitudes than the strongest decreases. In Figure 5.5 the relation of particle intensities with the parameters mentioned is displayed.
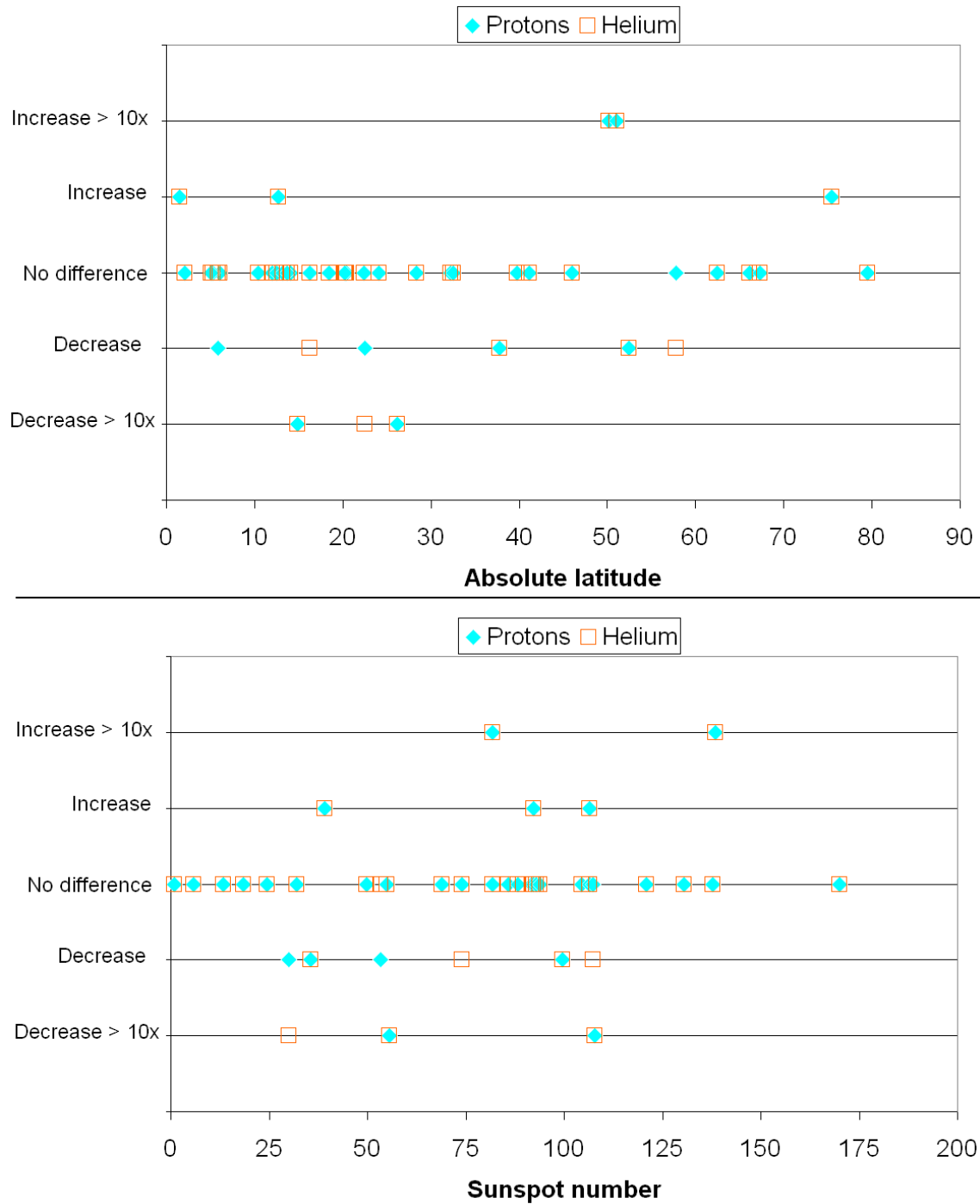
Figure 5.5. Distribution of increases, decreases, no differences and decreases and increases larger than one order of magnitude (> 10x) vs. latitude (top panel) and vs. sunspot number (bottom panel).

5.3   Directional anisotropies

The work presented in this section is almost entirely contained in Rodriguez et al., 2005. To characterize the particle angular distributions, protons in the energy range $0.63 - 0.77$

MeV have been analysed. With protons, the full directional capabilities of EPAC can be used. This is not the case for electrons, since there is no sectorisation for them. The proton directional information from the 32 available different angles of incidence (8 sectors at each of 4 telescopes) has been extended using a spherical expansion method described in Section 3.3.3. With this method the harmonic coefficients up to second order are obtained. They allow a characterization of the particles' directional anisotropies.

More specifically, due to the points discussed in the introduction, main interest is given to bidirectional field-aligned flows. Therefore the second order harmonic coefficient A_{20} will be analysed in more detail. Positive values of A_{20} represent field-aligned bidirectional particle fluxes, with stronger bidirectionality as A_{20} increases (considering that the expansion is around the magnetic field, which is the case for the analysis done in this thesis). For values lower than zero, the particles gyrate around the magnetic field, with a pitch angle close to 90°. In this work the dimensionless value of A_{20} is used, obtained after dividing A_{20} by A_0, which is the zeroth order coefficient, representing the isotropic portion of the distribution. The first order coefficients A_{1-1} and A_{11} describe the first order (unidirectional) part of the distribution perpendicular to the magnetic field. A_{10} represents the unidirectional components parallel to the field. For more information on the harmonic coefficients, see Table 3.3. The use of these coefficients is an important aid which complements and helps to quantify the eye inspection of pitch angle plots.

Figure 5.6 shows a color coded pitch angle representation of proton intensities, along with selected anisotropy coefficients for the event described in Figure 5.3. During the cloud passage, the pitch angle plot (top panel of Figure 5.6) shows a clear bidirectionality along the field, with high fluxes at 0° and 180° and minima close to 90°. A_{20} encompasses this description by increasing above 1, during the whole duration of the event. In addition to the bidirectionalities, increases in the first order coefficients are also present. Possible explanations for this behavior are monodirectional distributions underlying the bidirectional one caused by flows within the structure; or the loss of balance in the bidirectional distribution. In any case, it is clear that within the magnetic cloud, particles are ordered by the magnetic field. The bidirectional distribution extends further into the trailing part of the cloud as more closed field lines seem to trail the MC. It is not the case for the frontal part in which the bidirectional distribution appears suddenly and near to the commencement of the flux rope structure. The event under study is characterized by a closed magnetic structure, probably with both ends still connected to the Sun.
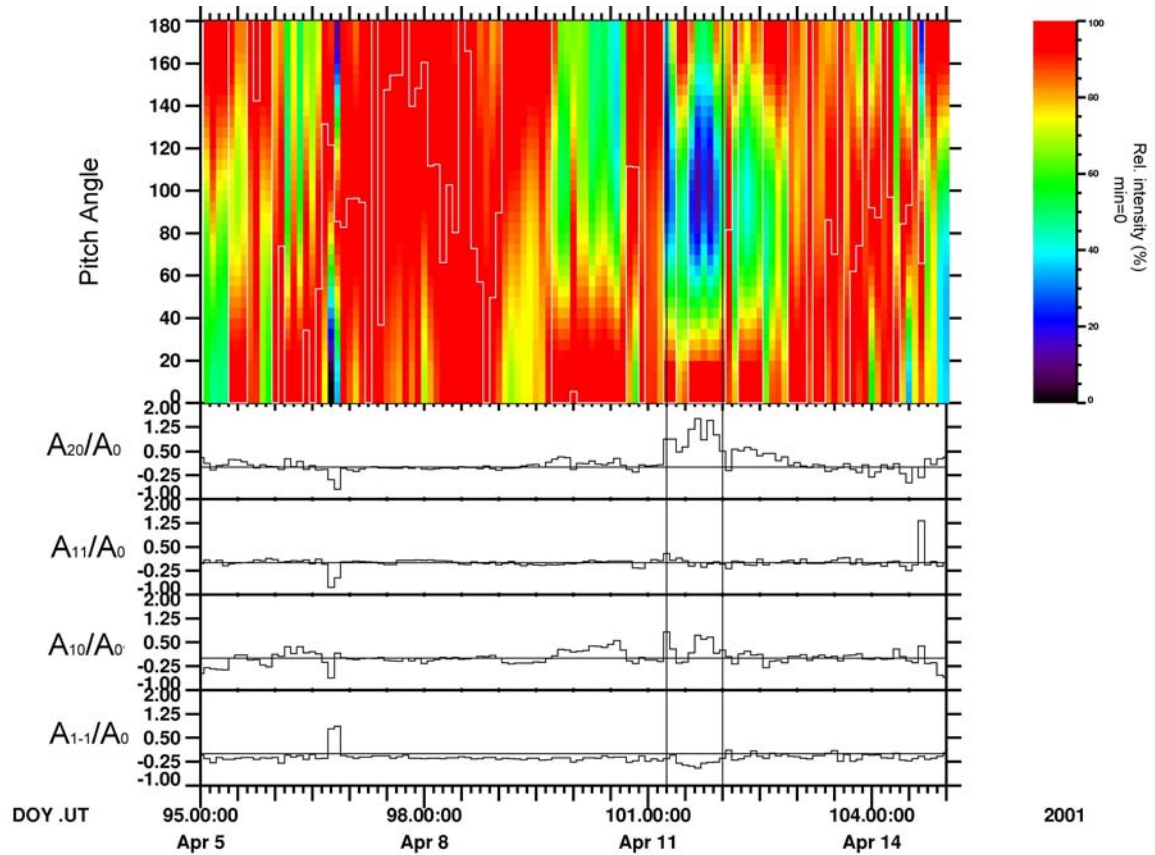
Figure 5.6. Pitch angle and harmonic expansion coefficients (from protons, 0.57-0.63 MeV) for the event in Figure 5.3.

Two parameters were obtained from analysing 1-hour averages of the A_{20} component for each event. The first value represents the average over the positive A_{20} counts (bidirectional field-aligned population); the second one was taken from the negative A_{20} values (population with $\sim 90°$ pitch angle gyrating around the magnetic field). In Table 5.1 a brief summary of the results obtained is given. The energetic protons are predominantly bidirectional (in 88% of the cases) in comparison with few cases in which they were found with pitch angles close to 90° (12%). Considering their duration, relative to that of the MC, in average positive values of A_{20} are present during 60% of the duration of the MC and negative ones during 44% (both percentages were calculated using the respective subsets to which they belong, i.e., $A_{20}>0$ or $A_{20}<0$, as 100%). Low positive values of A_{20} do not indicate a marked bidirectionality, as can be seen directly by eye inspection of the pitch angle plots. In order to assure bidirectionality, a threshold for A_{20} at 0.5 has been set. In this way, it can be estimated that clear bidirectionality is present in 33% of the studied cases with an average duration of 52% of the total duration of the event.

	$A_{20}>0$	$A_{20}<0$	$A_{20}>0.5$
% of cases	88	12	33
% duration	60	44	52
Avg. value	0.47	-0.2	1.09

Table 5.1. Summary of the behavior of the A_{20} coefficient inside magnetic clouds. The first row (% of cases) represents the percentage of MCs which had averaged A_{20} values larger than or smaller than the values stated in each column. The second row (% duration) represents the average duration of the different cases with respect to the duration of the clouds.

These results are qualitatively in agreement with those from Shodhan et al. [2000] and Riley et al. [2004]. By inspection of the pitch angle plots it has been inferred, nevertheless, that the bidirectional characteristics of the more energetic particles studied here show a higher degree of patchiness than their low energy counterparts.

Based on calculations on reconnection rates, Riley et al. [2004] estimated a decrease of approximately 2% of connectivity as the ICME propagates outwards. This calculation was based on theoretical estimations on the required reconnection rates in order to avoid the so-called flux catastrophe paradox (e.g., McComas et al., 1992). Basically, the paradox states that as CMEs propagate away from the Sun they carry new magnetic flux into the heliosphere, leading to a build up of magnetic flux which (according to McComas et al.) would double the heliospheric magnetic flux in 9 months. In this way, the reconnection rate found by Riley et al. represents the lower limit needed to avoid this situation. A similar trend was found here by analysing the A_{20} coefficient vs. heliocentric distance. This result is presented in Figure 5.7. A reduction of $A_{20}>0$ intervals as the ICME travels away from the Sun represents a lost of bidirectionality, explainable by an alteration of the connection to the Sun by magnetic reconnection. Therefore it can be related to the reconnection rate. The slope of 4 - 5%/AU, derived from the linear fit (Figure 5.7) is somewhat steeper than the 2%/AU of Riley et al. [2004]. However it should be considered with care, due to the high level of scatter present in the data. The figure contains separate panels for the $A_{20} > 0$ and the $A_{20} > 0.5$ criteria.

In a further approach to try to correlate periods with bidirectional fluxes and, therefore, with a possible connection of the field lines back to the Sun, the elliptical flux rope model described in Section 3.4.2 has been used. As it was previously mentioned, by applying the model to the events under study parameters such as the orientation of the flux rope axis, current densities and geometric variables describing the expected shape of the clouds are obtained. After a thoughtful comparison it can be concluded that there is no striking dependence between the different parameters obtained from the model and the A_{20} coefficient.
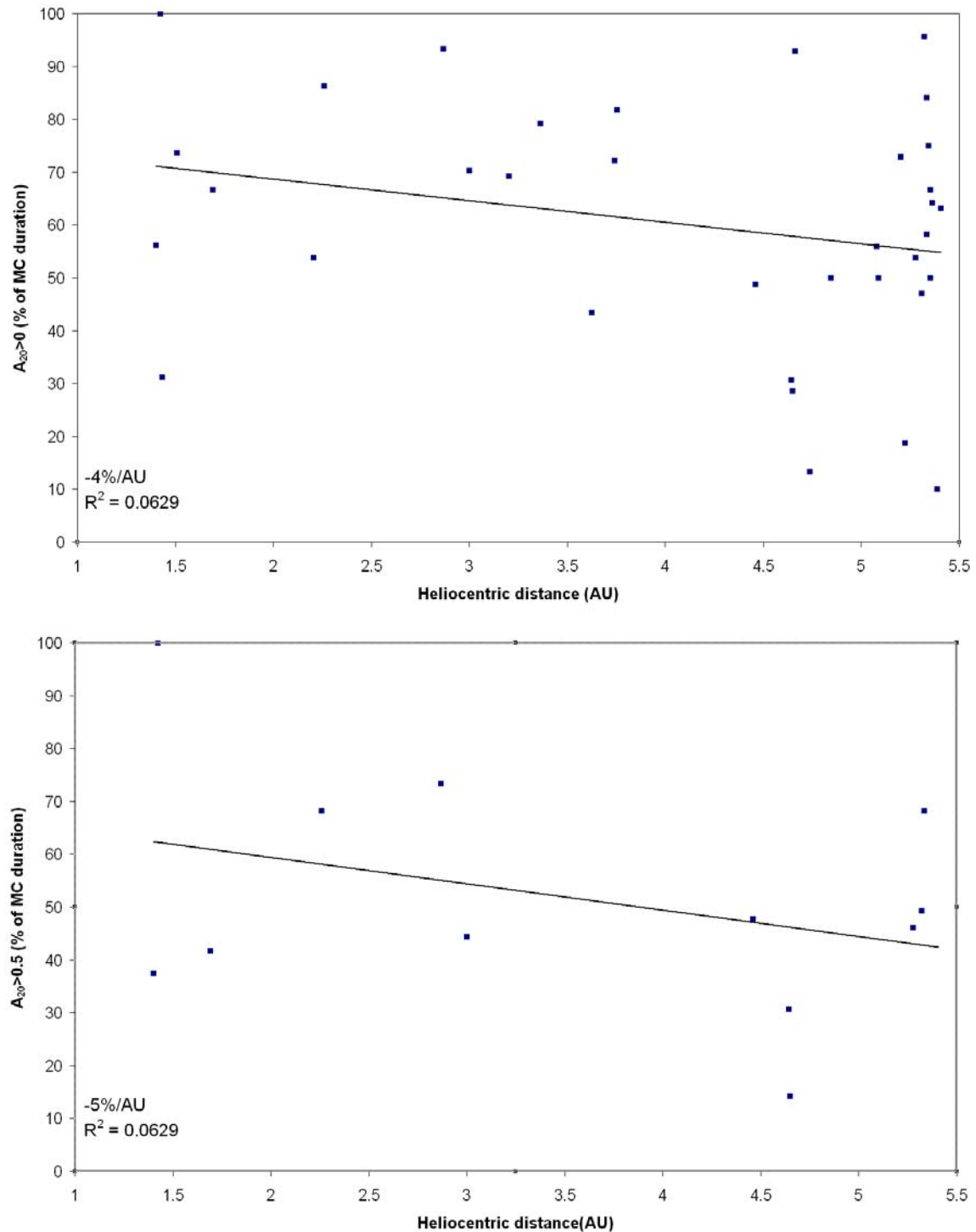
Figure 5.7. Development of the A_{20} coefficient with respect to distance from the Sun. Top panel shows the more permissive $A_{20} > 0$ criterion, while the bottom panel contains fewer events due to the A20 > 0.5 criterion. A negative trend is seen, though the highly scattered points preclude further conclusions to be drawn.

The degree of connectivity of the clouds seems to be independent of the local geometric characteristics as inferred from the model. As an example, Figure 5.8 show the relation between the A_{20} coefficient and the azimuthal (phi) and elevation (theta) angles of the flux rope axis orientation (in the RTN system), obtained from the model.
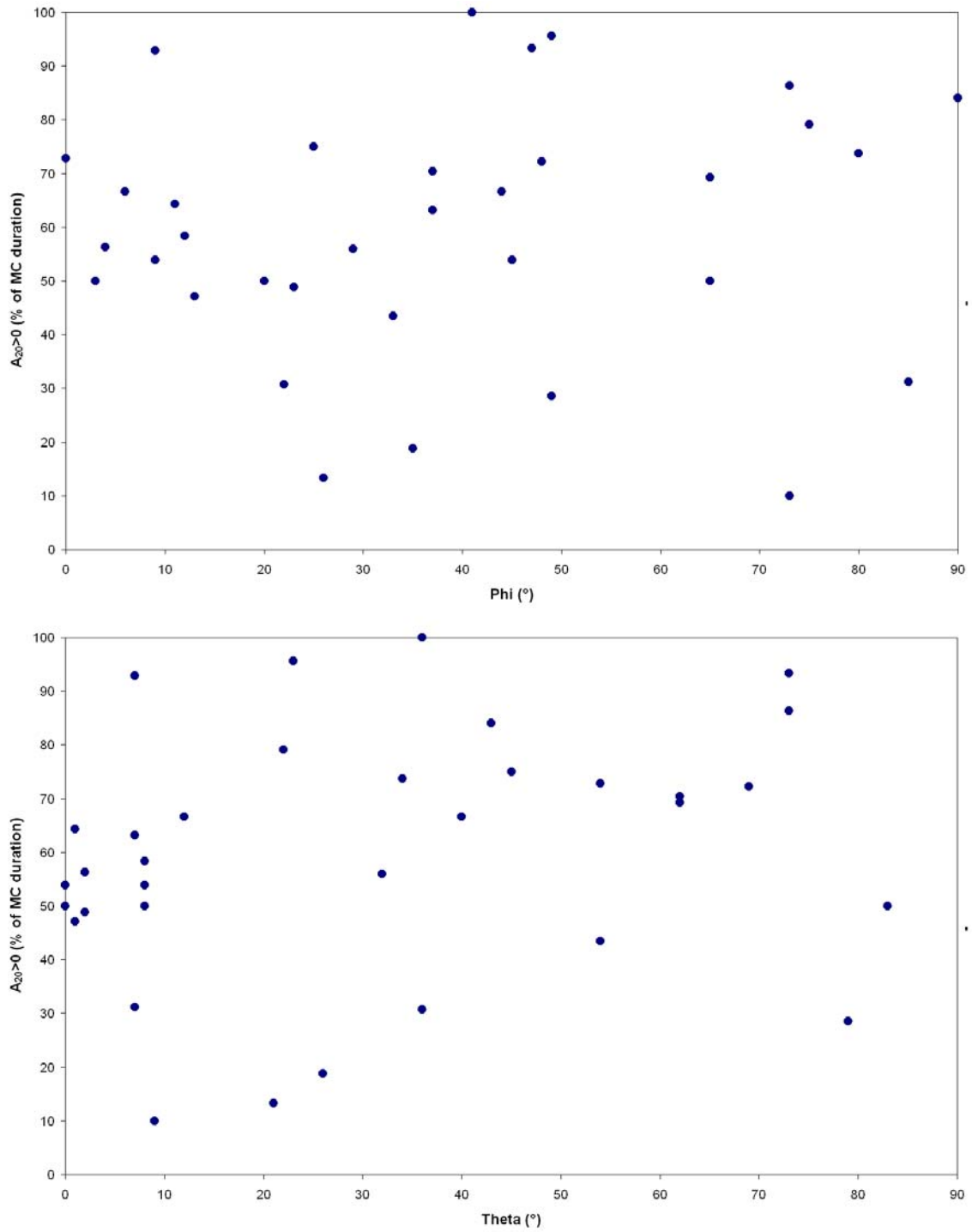
Figure 5.8. Comparison between A20 >0 vs. phi (top panel) and A20>0 vs. theta (bottom panel) with θ and φ obtained from the magnetic cloud model from Section 3.4.2.

5.4   Elemental abundances

In this section, the result of elemental abundance analysis for various ion species $(0.5 - 2$ MeV) over the 40 MCs described in Table 3.1 is presented. Due to low count rates, the sampling of individual events is highly difficult. Therefore, by accumulating over the whole set of events, the statistics are improved. The objective of this procedure is to obtain an idea on which one of the commonly observed energetic particle populations in the heliosphere presents most similarities to the one measured inside magnetic clouds. The abundances found in the way described in Section 3.3.2, for the set of magnetic clouds are shown in Table 5.2, together with abundances of several energetic particles sources for comparison (obtained from the literature, see table caption).

El.	Quiet Times [1]	ACR [2]	CIR [1]	SEP(I)[2]	SEP(G)[2]	MC[3]
He	263 ± 26	5 ± 1	162 ± 16	46 ± 4	57 ± 3	24 ± 5
C	0.05 ± 0.02	0.01	0.8 ± 0.1	0.434 ± 0.03	0.465 ± 0.009	0.414 ± 0.137
N	0.08 ± 0.02	0.12 ± 0.01	0.12 ± 0.01	0.157 ± 0.018	0.124 ± 0.003	0.101 ± 0.053
O	1.0 ± 0.1	1.0 ± 0.01	1.0 ± 0.02	1.0 ± 0.045	1.0 ± 0.01	1.0 ± 0.249
Ne	0.1 ± 0.02	0.07 ± 0.01	0.16 ± 0.01	0.400 ± 0.028	0.152 ± 0.004	0.211 ± 0.069
Mg	0.02 ± 0.01	0.001	0.12 ± 0.01	0.408 ± 0.029	0.196 ± 0.004	0.174 ± 0.101
Si		0.001	0.086 ± 0.008	0.352 ± 0.027	0.152 ± 0.004	0.127 ± 0.055
S		0.001	0.033 ± 0.004	0.117 ± 0.015	0.032 ± 0.007	0.053 ± 0.026
Fe		0.001	0.11 ± 0.01	1.078 ± 0.046	0.134 ± 0.004	0.198 ± 0.071

Table 5.2. Elemental abundances for different populations in the heliosphere with respect to oxygen. The last column represents the average values measured inside magnetic clouds. (1) Keppler et al. [1995]; 2 – 6 MeV/amu for Quiet Times and 0.6 – 2.5 MeV/amu for CIRs. (2) Reames et al. [1999] and references therein; ~5 MeV/amu for ACRs, 5 -12 MeV/amu for SEPs. (3) This work, 0.6 - 2 MeV/amu.

The ratios were obtained during three different periods, since the instrument uses different calibration setups throughout the Ulysses mission. The value shown in the table corresponds to the average of these three values. The standard deviations shown for MC values represent the errors produced by ion track overlapping and counting statistics.
The population of energetic particles within MCs has elemental abundances best comparable with gradual SEP accelerated particles. In Figure 5.9, this correspondence is shown. Intra-MC energetic particles seem to originate from the solar wind population, accelerated by the shock driven by the ICME. Nevertheless, there are deviations from the normal gradual SEP abundances.
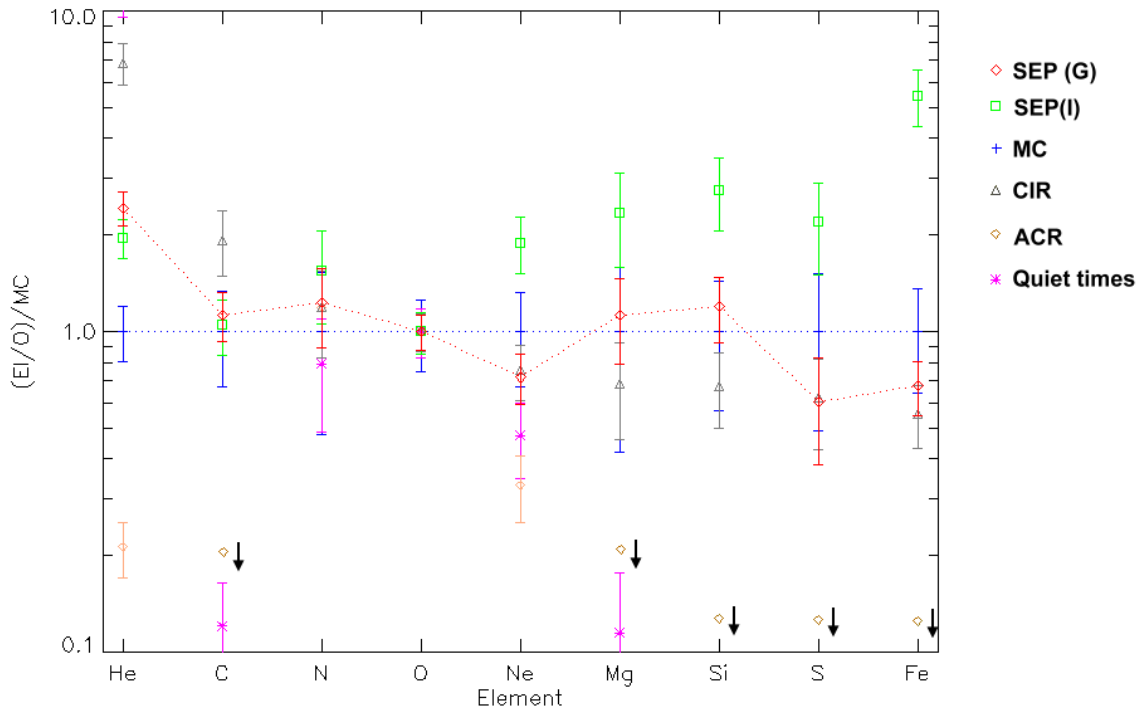
Figure 5.9. Elemental abundances for different populations in the heliosphere normalized to Intra-MC values. The quantities are taken from Table 5.2. The abundances corresponding to MCs and gradual SEP events have been joined for comparison by dashed blue and red lines, respectively.

For all of the elements but one, the differences between Intra-MC and gradual SEP particles are within error limits. Some of the abundance ratios lie also close to the impulsive SEP values. Nevertheless iron (more than 5 times lower in MC than in impulsive SEP) is the best proof that the averaged abundances do not correspond to impulsive SEP. Acceleration by flares, (or impulsive SEP events) is characterized partially by high iron to oxygen abundances, with ratios even greater than 1 (Table 5.2). In any case, it should be noticed that the difference in energy ranges could introduce systematic shifts of the values between the different sources (see caption of Table 5.2), Reames [1995] pointed a 10% increase in Fe/O when moving from 2 – 3 MeV/amu to 5 - 12 MeV/amu.

The only ion which is not within error bars between the Intra-MC and gradual SEP values is helium. Its abundance is a factor of two lower than what is expected in gradual SEP events. This deviation might be instrumental, since the EPAC helium track in this energy range is not complete (see Fränz, 1994). This introduces a systematic underestimation of He fluxes of unknown extent.

The FIP effect (Section 1.1.2) is present in the energetic particles inside MCs, displayed in Figure 5.10. This effect is known to exist for the solar wind (Geiss et al, 1995) and for certain energetic particle populations (Reames, 1999) such as gradual SEP. The existence of the FIP effect in gradual SEP is not surprising if one considers that gradual SEP particles are accelerated from the solar wind thermals and suprathermals swept by

the ICME shock. This is another indication that the energetic particles within MCs belong to gradual SEP events.
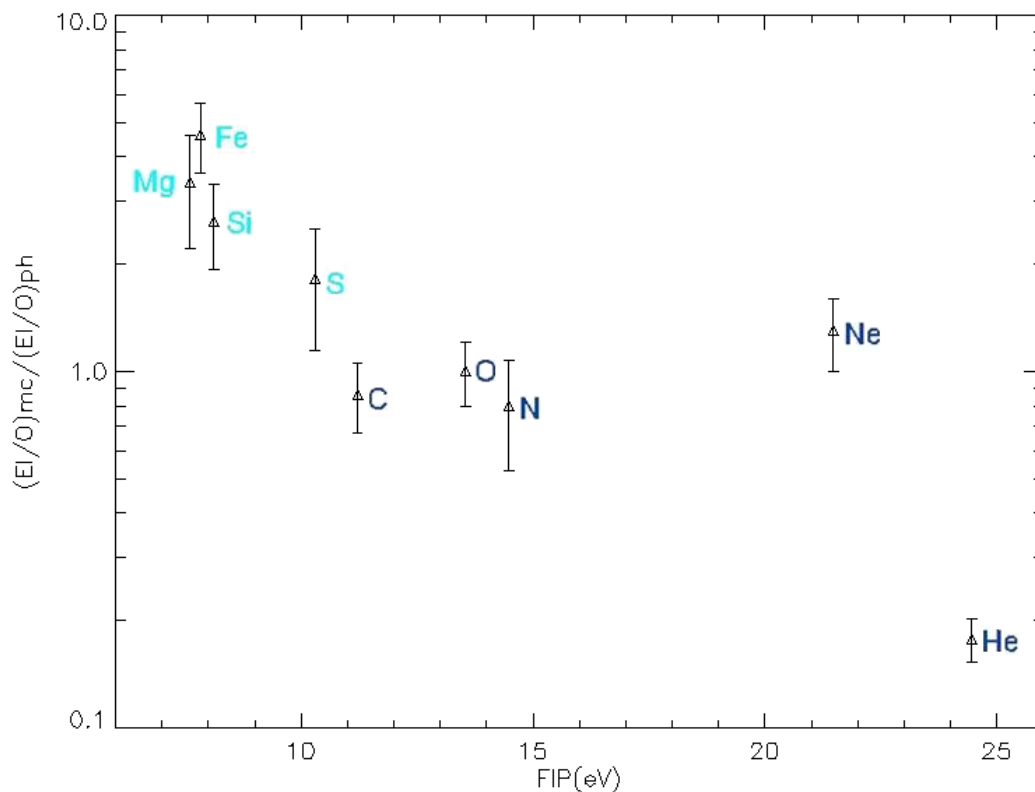
Figure 5.10. Elemental abundances inside MCs, relative to photospheric abundances, vs. First Ionization Potential (FIP).

5.5   Flare associated events: A case study

No indication for flare acceleration on statistical bases has been found, as can be deduced from the previous section. However in this section, a single event which clearly shows flare imprints will be analysed. This event is the one shown in Figure 5.3. Its basic characteristics have been described in Section 5.2, in Section 5.3 directional information provided by protons have been analysed.

An important point concerns the nature of the few energetic particles contained in this closed magnetic region. Figure 5.11 displays ratios of certain ion groups obtained from different divisions in the EPAC matrix. These divisions allow a separation between iron on one side; carbon, nitrogen and oxygen secondly; and finally helium and protons. The remarkable feature in these plots is the increase in iron with respect to the other elements. The ratio Fe/CNO reaches 1 during the peaks, which is close to the characteristic ratio for flare acceleration, as seen in impulsive SEP events (see Table 5.2). The particular composition in this event seems to rule out a shock (or gradual SEP)

acceleration. Flare acceleration seems to be a plausible source for these particles. This process, though, does not appear to be active by the time when Ulysses is immersed in the structure, a hypothesis supported by the lack of electrons increases (see Figure 5.12). The flare particles were probably trapped when the flux rope was ejected from the Sun.
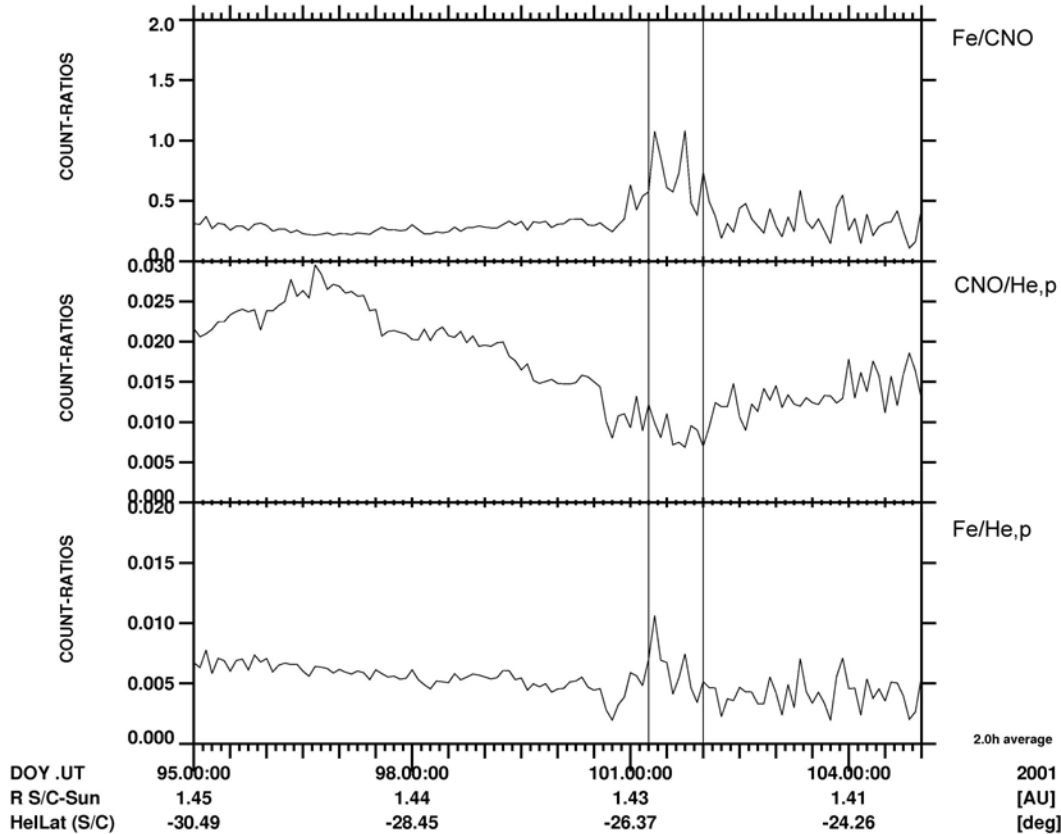
Figure 5.11. Ratios between the count rates of the different EPAC matrix divisions. From top to bottom are shown: Fe / CNO, CNO / He,p, Fe / He,p. The data are 2-hour averaged and the solid line delimits the MC from Figure 5.3.

It is worth noticing that the oxygen freezing-in temperatures (displayed in Figure 5.3) seen within this event are among the highest values ever detected by Ulysses (in- or outside a MC), with temperatures exceeding 3 MK. The presence of these extremely enhanced charge states (including iron) favours the flare explanation. Bame et al. [1979] (later Lepri and Zurbuchen, 2004) proposed that flare accelerated particles are the ones that may heat the plasma up to such high temperatures.

Electron profiles for this event have not been previously shown. In Figure 5.12 the intensities corresponding to the four EPAC telescopes are presented in the top four panels. As it was seen for protons (Figure 5.3) the electron intensity decreases shortly before the arrival of the cloud at Ulysses. In order to assess any possible directional information provided by the electrons, the last two panels show the ratio of the different telescopes. Telescope 1 points towards Earth, telescope 4 in the opposite direction and between them, telescope 2 and 3 are located (Section 2.2.2). For this case, the parker spiral direction coincides with the coverage of telescope 2. This procedure of obtaining

ratios between the different telescopes represents the only source of directional information that can be obtained with electron data, since there is no sectorisation for them. In any case, as can be seen in the figure, there are no deviations in the incoming direction of electrons during the cloud. The ratios remain unaltered throughout the period of time shown. In contrast to protons (Section 5.3), the direction of electrons does not appear to vary during the cloud.
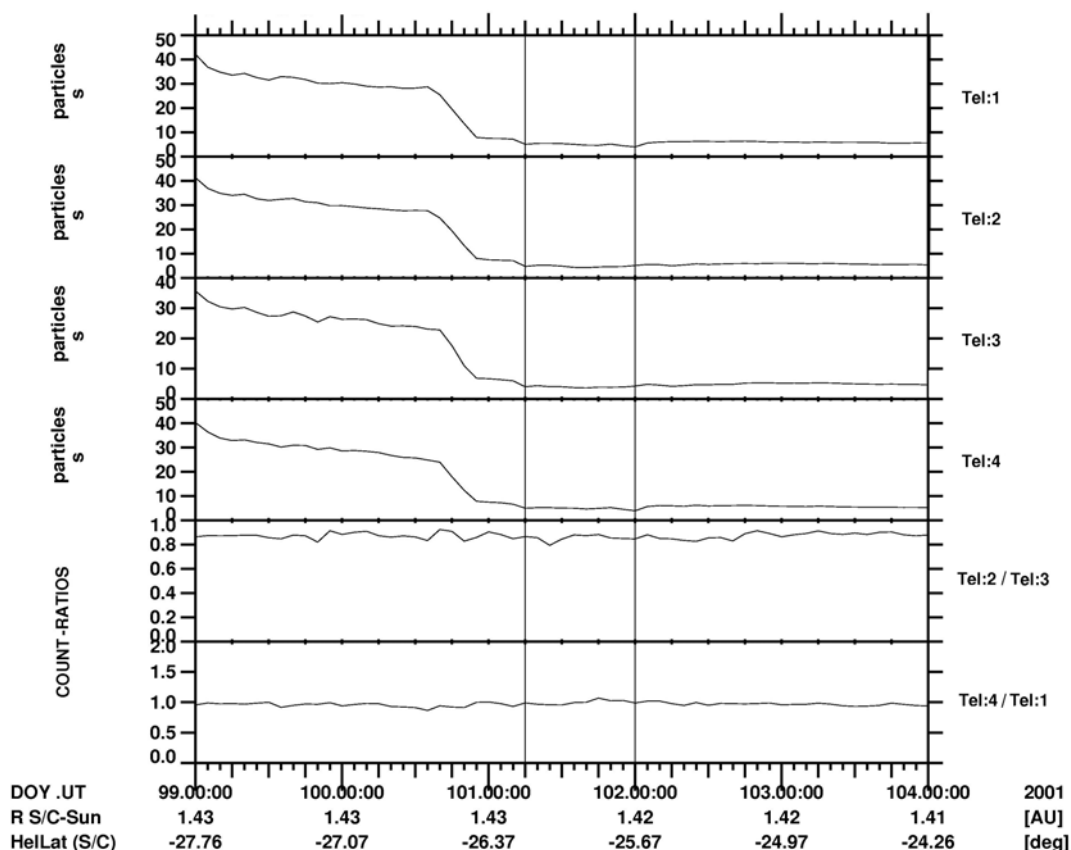
Figure 5.12. Electrons in the 0.1-0.38 MeV energy range for the MC in Figure 5.3. The top four panels show the electron intensity in the four EPAC telescopes. The last two panels present the ratio of Telescope 2 to Telescope 3 and Telescope 4 to Telescope 1.

Thus, directional anisotropies of electrons for this event show no preferential direction of propagation. For protons, an unbalanced bidirectionality of the fluxes was deduced.

Based on this analysis, the MC detected by Ulysses on day 101 in 2001 seems to have acted as an obstacle for the already present particle population. From Figure 5.3 it can be seen that the first decrease in particle fluxes was most probably due to the arrival of a big disturbance, with the highest magnetic field intensity seen by Ulysses so far in 2001. The disturbance blocked the enhanced particle background already present. The appearance of a flux rope structure at Ulysses cause a second 10-fold decrease in the ion intensity, even though the magnetic field strength had already diminished to one half of the peak values in the precedent hours. Characteristic abundances within this period lead to the conclusion that the particles are flare accelerated. Nevertheless, flare particles do not seem to enter the cloud while Ulysses is in it, due to the absence of energetic electrons.

Therefore it is here proposed that the particles were trapped when the flux rope was created at the Sun. Directional anisotropies of protons show mainly bidirectional fluxes within the cloud, which are indicators of closed magnetic structures. The fluxes tend to be unbalanced, especially for the trailing part of the event. Unidirectional fluxes appeared likely due to the presence of flows within the closed structure. The MC was probably connected to the Sun at the moment it crossed Ulysses at 1.4 AU, but field lines on both legs of the CME were not static. They were most probably reconnecting and providing thus different degrees of connection on either side, favouring in this way the observed unbalanced bidirectional fluxes.

The presence of flares in, or near, the CME erupting region would support the flare association of this event. Using a simple ballistic calculation, the ICME should have left the Sun on April 7th (day of year 97), 2001. According to the LASCO CME catalog (this CME catalog is generated and maintained by NASA and The Catholic University of America in cooperation with the Naval Research Laboratory and can be found at http://cdaw.gsfc.nasa.gov/CME_list/), a partial Halo CME left the Sun at 17:17 UT on April 7th. This CME originated just behind the west limb of the Sun at a position angle of 275° (measured counter clockwise from solar north in degrees), Ulysses was located at -25° with respect to the ecliptic and at an angle of 123° west to the Earth-Sun line. Figure 5.13 was created to show this CME in a LASCO C2 running difference image (showing the difference in brightness from one observation to another) as well as the relative position of Ulysses at that time. Temporal and spatial considerations make this CME a plausible candidate for the MC that Ulysses detected almost 4 days later. This CME had an extremely high speed of 2198 km/s (listed in the catalog), but was decelerating at a high rate. Less than 1% of the CMEs detected with SOHO have velocities exceeding 2000km/s. Unfortunately, the source region of this CME is not visible from Earth and the presence of flaring activity close to the erupting region cannot be inferred.

Even though the CME was ejected from behind the west solar limb, making a visual investigation of the source region impossible, the presence of flare accelerated particles and extremely high freezing-in temperatures in the event analysed seem to support the hypothesis of a relation between this CME and a flare.
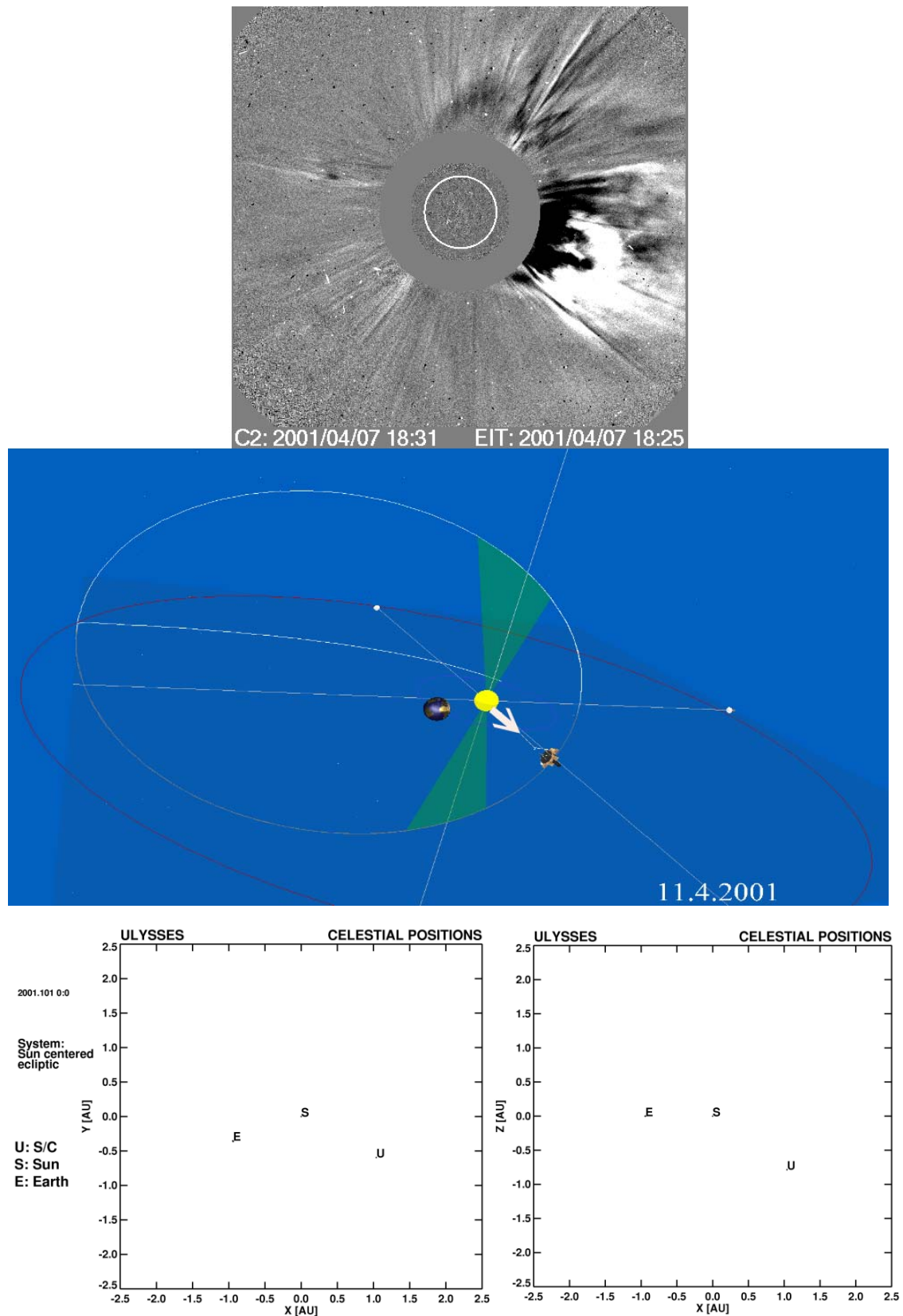
Figure 5.13. Top panel: CME on day 97, 2001 (SOHO running images). Middle panel: Ulysses, the Sun and the Earth on day 101, 2001; when the MC from Figure 5.3 was detected. The direction of propagation of the CME on day 97, white arrow in the middle panel, coincides with the location of Ulysses. Bottom panel: positions of the Sun (S), Ulysses (U) and the Earth (E).

Chapter 6   Summary and Conclusions

The studies presented in this thesis are directed towards a complete characterization of coronal mass ejections (CMEs) in the heliosphere by means of a rich dataset provided by the Ulysses spacecraft. The picture of interplanetary CMEs (ICMEs) is normally composed of magnetic field and plasma parameters. A set of signatures discovered by different authors in the last decades is used to identify ICMEs in in-situ data. Complementary, and significant, information regarding composition of the thermal solar wind plasma and energetic particle properties have been added in this work. The ionization level of solar wind ions, converted to freezing-in temperature provides conclusive information of the source region of the CME. Energetic particles serve as tracers for the magnetic field configuration and their elemental abundances relate to acceleration mechanisms connected to the CME release and propagation.

A characteristic subset of all the ICMEs with particular magnetic field structure, namely magnetic clouds (MC), was specially studied. MCs can be found by the presence of a rotation in the magnetic field vector, a low proton temperature and a depleted plasma beta. MCs represent the pristine version of ICMEs, due to their highly ordered internal magnetic field. In addition, they are highly geoeffective.

By the study of the oxygen freezing-in temperature OFT (or its associated charge states) within ICMEs and its comparison with different solar wind streams, several points have been established. OFT is increased in more than 90% of all the magnetic clouds analysed, by 26% in average with respect to the surrounding solar wind. This behavior can be found at all heliographic latitudes and phases of the solar cycle. There is a profound difference between OFT behavior in cloud and non-cloud ICMEs. The enhancement in the OFT between cloud ICMEs and in the quiet slow solar wind is approximately two slow wind standard deviations ($\sim 2\sigma$). The enhancements are present but to a lower degree in non-cloud ICMEs. The difference between the OFT of non-cloud ICMEs and quiet slow solar wind is less than one slow wind standard deviations

($< 1\sigma$). OFT analysed for each particular case, provides a complementary in-situ tool to differentiate MCs from non-cloud ICMEs and quiet solar wind.

The variations in OFT are mirrored to certain extent in those of carbon and iron. The freezing-in temperatures of all of them are increased within MCs, reflecting once again the high temperatures reigning in the corona during the CME eruption. Nevertheless the spatial profiles from the different ions show different structures. Since various ions freeze-in at different heights in the corona, the difference in charge states reflect the temperature evolution of the ICME. The profiles of O, C and Fe show that the internal structure of the CME is non-homogeneous and has evolved significantly only in a few solar radii from its origin. The highest heating is seen at the height where oxygen freezes-in (around 1.5 Rs).

An analysis was carried out in order to establish possible statistical trends leading towards a differentiation on the ionization levels present before, during and after MCs, in search for traces of the 3-part structure in interplanetary space. In the results shown here there is no indication of such behavior. On a different approach, a case study was undertaken in order to identify possible individual events which were unnoticed in previous statistical analysis. There were no distinctive structures detected at one side of the flux rope which did not appear on the other side. The definite presence of different solar wind structures on both extremes and inside the flux rope can not be definitively inferred. No signs of a 3-part structure have been found for interplanetary CMEs. Nevertheless, the leading part seems to present higher temperatures than the trailing part. The 3-part structure has not been previously detected in interplanetary space, the different parts may be moving with respect to each other, merging, etc. Most probably it represents a feature which is lost close to the Sun.

The freezing-in temperatures of iron, carbon and oxygen ions were combined with results from a flux rope model in order to infer properties of the internal structure of MCs. Freezing-in temperature maps of MCs and their surrounding solar wind were created in this way. Elevated temperatures are highly confined to the flux rope region. On the other hand, there is no clustering of high temperatures close to the center of the cloud as it would have been expected, the tendency is to detect also high temperatures closer to the flanks of the cloud. At low angles, the high temperatures appear more spread and not as well confined as at higher angles, but they are definitely present. The maxima in OFT are occurring most frequently close to the commencement of the flux rope and not close to its end.

On a higher energy range, KeV to MeV fluxes of protons and helium ions have provided hints on the intensity responses to MC passage. For energetic particles fluxes, no correlation with magnetic clouds could be found. The response depends heavily on the energetic particle background, governed by the conditions in which each event is immersed. In the majority of the events, the flux levels remained approximately constant. Increases and decreases were less often observed. The different responses were observed at all latitudes and solar cycle phases. Nevertheless, the strongest increases

were found to occur at higher latitudes than the strongest decreases, due to the different particle background in which the cases were immersed.

In order to establish the magnetic configuration of MCs, the second order harmonic coefficient A_{20} (proton data) was analysed in search of bidirectional distributions within MCs. The energetic protons are predominantly bidirectional within MCs ($A_{20}>0$, in 88% of the cases). Strong bidirectionality ($A_{20}>0.5$) is present in 33% of the studied cases with an average duration of 52% of the total duration of the event.

There is only a weak correlation between percentages of bidirectional periods inside magnetic clouds with respect to distance from the Sun. The trend is negative as expected, meaning that the connectivity decreases as the magnetic field lines reconnect while the ICMEs travel outwards. As a result of comparing the A_{20} coefficient with parameters obtained from the flux rope model it can be concluded that there is no apparent correlation between them. The degree of bidirectionality (and probably resulting connectivity) in the clouds seems to be independent of the local geometric characteristics as inferred from the model.

In summary, MCs most probably consist of a mix of magnetic loops with one or both footpoints connected back to the Sun.

The elemental composition of energetic particles was used as a diagnostic for acceleration mechanisms associated with ICMEs. This analysis showed that energetic particles within MCs have elemental abundances comparable with gradual SEP accelerated particles. Intra-MC energetic particles seem to originate from the solar wind population, accelerated by the shock driven by the ICME. The FIP effect as found for energetic particles inside MCs, which is also present in SEP events, provides another indication that the energetic particles within MCs belong to gradual SEP events.

Finally, a MC detected at Ulysses in April 2001 provided evidence of a possible flare-CME connection. The particular composition of the energetic particles in this event, namely elevated iron abundances, most likely rules out a shock (or gradual SEP) acceleration. Flare acceleration seems to be a plausible source for these particles. These flare particles were probably trapped when the flux rope was ejected from the Sun. The existence of bidirectional protons showed that the MC was probably connected to the Sun at the moment it crossed Ulysses.

The flare association is favoured by the freezing-in temperatures seen within this event, which are among the highest ones ever detected by Ulysses (in- or outside a MC), with temperatures exceeding 3 MK. The presence of these extremely enhanced charge states is consistent with the explanation that flares may heat the related CME plasma up to such high temperatures. Even though the CME was ejected from behind the west solar limb, making a visual investigation of the source region impossible, the presence of flare accelerated particles and extremely high freezing-in temperatures in the event analysed seem to support the hypothesis of a relation between this CME and a flare.

This work has explored the relation between charge states and the magnetic structure of the solar wind, more specifically within magnetic clouds. Composition data of the solar

wind plasma represents a relatively new tool in relation to ICME identification and analysis. It has been proven that it can provide important insights into the internal structure of ICMEs. The information obtained from energetic particles can be used to infer properties of ICMEs, magnetic structure and acceleration processes being among the most important ones. The results provided here serve to add further constraints to CME models and to increase the understanding of these very complex phenomena.

References

Arnaud, M., and R. Rothenflug, An updated evaluation of recombination and ionization rates, Astron. Astrophys. Suppl. Ser., 60, 425, 1985.

Balogh, A., T. J. Beek, R. J. Forsyth, P. C. Hedgecock, R. J. Marquedant, E. J.Smith, D. J. Southwood, B. T. Tsurutani, The magnetic field investigation on the Ulysses mission: Instrumentation and preliminary scientific results, Astron. Astrophys. Suppl., 92, 221, 1992.

Bame, S. J., A. J. Hundhausen, J. R. Asbridge, I. B. Strong, Ion Composition of the Solar Wind, Astronomical Journal, 73, 55, 1968.

Bame, S. J., J. R. Asbridge and J. T. Gosling, Evidence for a structure-free state at high solar wind speeds, J. Geophys. Res., *82*, 1487, 1977.

Bame, S. J., J. R. Asbridge, W. C. Feldman, E. E. Fenimore, J. T. Gosling, Solar wind heavy ions from flare-heated coronal plasma, Sol. Phys., 62, 179, 1979.

Bame, S. J., D. J. McComas, B. L. Barraclough, J. L. Phillips, K. J. Sofaly, J. C. Chavez, B. E. Goldstein, R. K. Sakurai , The Ulysses solar wind plasma experiment, Astron. Astrophys. Suppl., 92, 237, 1992.

Barouch E. and L. F. Burlaga, J., Causes of Forbush Decreases and other Cosmic Ray Variations, J. Geophys. Res., 80, 449, 1975.

Baumjohann W. and R. A. Treumann, Basic Space Plasma Physics, Imperial College Press and World Scientific, 1997.

Bertotti B., R. Ambrosini, S.W. Asmar, J.P. Brenkle, G. Comoretto, G. Giampieri1, L. Iess, A. Messeri and H.D. Wahlquist, The gravitational wave experiment, Astron. Astrophys. Suppl., 92, 431, 1992.

Biermann, L., Kometschweife und solare Korpuskularstrahlung, Z. Astrophys., 29, 274, 1951.

Billings, D. E., A guide to the Solar Corona, Academic Press, New York, 1966.

Bird, M.K., S.W. Asmar, J.P. Brenkle, P. Edenhofer, M. Pätzold, and H. Volland, The coronal-sounding experiment, Astron. Astrophys. Suppl. Ser., 92, 425, 1992.

Bothmer, V., R. G. Marsden, T. R. Sanderson, K. J. Trattner, K.-P. Wenzel, A. Balogh, R. J. Forsyth, B. E. Goldstein, The Ulysses south polar pass: Transient fluxes of energetic ions, Geophys. Res. Lett., 22, 3369, 1995.

Bothmer, V., M. I. Desai, R. G. Marsden, T. R. Sanderson, K. J. Trattner, K.-P. Wenzel,

J. T. Gosling, A. Balogh, R. J. Forsyth, B. E. Goldstein, ULYSSES observations of open and closed magnetic field lines within a coronal mass ejection, Astron. Astrophys., 316, 493, 1996.

Bothmer, V., Schwenn, R., The structure and origin of magnetic clouds in the solar wind, Ann. Geophys. 16, 1, 1998.

Brueckner, G.E., et al., The Large Angle Spectroscopic Coronagraph (LASCO), Sol. Phys., 162, 357, 1995.

Burlaga, L. F., Magnetic clouds: Constant force-free configurations, J. Geophys. Res., 93, 1988.

Burlaga, L.F., Magnetic Clouds, in Physics of the Inner Heliosphere II, eds. R. Schwenn, and E. Marsch, Springer-Verlag, Berlín, 1990.

Cane, H. V., Coronal Mass Ejections and Forbush Decreases, Space Sci. Rev., 93, 55, 2000.

Carrington, R.C., Monthly Notices of the Royal Astronomical Society, 20, 13, 1860.

Cid, C., Estudio de las Eyecciones de Masa de la Corona Solar en el Medio Interplanetario, Thesis, Universidad de Alcalá, Madrid, 2000.

Cocconi, G., K. Greisen, P. Morrison, T. Gold and S. Hayakawa, The Cosmic ray flare effect, Il Nuovo Cimento Supplement Series 10, 8, 161, 1958.

Cravens, T. E., Physics of Solar System Plasmas, Cambridge, 1997.

Cremades, H. and V. Bothmer, On the three-dimensional configuration of coronal mass ejections, Astron. Astrophys., 422, 307-322, 2004.

Crooker, N. U., J. T. Gosling, E. J. Smith, and C. T. Russell, A Bubblelike Coronal Mass Ejection Flux Rope in the Solar Wind, in Physics of Magnetic Flux Ropes, eds. C. T. Russell, E. R. Priest, and L. C. Lee, Geophys. Monogr. Ser., 58, 365, 1990.

Domingo, V., Fleck, B. and Poland, A. I., The SOHO Mission: An Overview, Sol. Phys., 162, 1, 1995.

Feldman, W.C., and E. Marsch, Kinetic phenomena in the solar wind, in Cosmic Winds and the Heliosphere, eds. J.R. Jokipii, J.R. Sonett, C.P. Giampapa, and M.S. Mathews, Univ. Ariz. Press, Tucson, 1997.

Fenimore, E. E., Solar Wind Flows Associated with Hot Heavy Ions, Astrophys. J., 235, 245-257, 1980.

Fisk, L. A., Motion of the Footpoints of Heliospheric Magnetic Field Lines at the Sun: Implications for Recurrent Energetic Particle Events at High Heliographic Latitudes, J. Geophys. Res., 101, 15547, 1996.

Fränz, M. and N. Krupp, Ulysses EPAC Experiment: Spherical Harmonic Expansion of Three-Dimensional Particle Distributions, Internal Paper B v2, MPAe, 1993.

Fränz, M., Ionen mittlerer Energie in der Heliosphäre: Ergebnisse des Ulysses-EPAC-Experiments in der Ekliptik, Dissertation, T.U. Braunschweig, 1994.

Fränz M. et al., Ulysses EPAC Experiment: MPAE IDL program package, Internal Paper D, MPAe, 1995.

Galvin, A. B., Minor ion composition in CME-related solar wind, in Coronal Mass Ejections, Geophysical Monograph 99, eds. N. Crooker, J.A. Joselyn and J.

Feymman, 253, 1997.

Galvin, A. B.; G. Gloeckler, F. M. Ipavich, C. M. Shafer, J. Geiss, K. Ogilvie, Solar wind composition measurements by the ULYSSES SWICS experiment during transient solar wind flows, Adv. Space Res., 13, 75, 1993.

Geiss J., G. Gloeckler and R. von Steiger, Origin of the Solar Wind From Composition Data, Space Sci. Rev. 72, 49, 1994.

Gloeckler, G., J. Geiss, H. Balsiger, P. Bedini, J. C. Cain, J. Fischer, L. A. Fisk, A. B. Galvin, F. Gliem, D. C. Hamilton et al., The solar wind ion composition spectrometer, Astron. Astrophys. Suppl., 92, 267, 1992.

Gold, T., Plasma and Magnetic Fields in the Solar System, J. Geophys. Res., 64, 1665, 1959.

Goldstein, H., On the field configuration in magnetic clouds, in Solar Wind Five, NASA Conf. Publ., CP-2280, 731, 1983.

Gopalswamy, N., et al., On the relationship between coronal mass ejections and magnetic clouds, Geophys. Res. Lett., 25, 2485, 1998.

Gosling, J.T., Coronal mass ejections and magnetic flux ropes in interplanetary space, in Physics of Magnetic Flux Ropes, eds. C.T. Russell, E.R. Priest, L.C. Lee, Geophysical Monograph 58, 343, 1990.

Gosling, J. T., New Findings Challenge Beliefs about Solar-Terrestrial Physics, Eos, 74, 52, 1993a.

Gosling, J. T., The solar flare myth, J. Geophys. Res., 98, 18937, 1993b.

Gosling, J. T., J. R. Asbridge, S. J. Bame, W. C. Feldman, and R. D. Zwickl, Observations of large fluxes of He+ in the solar wind following an interplanetary shock, J. Geophys. Res., 85, 3431, 1980.

Gosling, J. T., D. N. Baker, S. J. Bame, W. C. Feldman, R. D. Zwickl, and E. J. Smith, Bidirectional solar wind electron heat x events, J. Geophys. Res., 92, 8519, 1987.

Gosling, J.T., Corotating and transient solar wind flows in three dimensions, Ann. Rev. Astron. Astrophys., 34, 35, 1996.

Grün, E., H. Fechtig, R.H. Giese, J. Kissel, D. Linkert, D. Maas, J.A.M. McDonnell, G.E. Morfill, G. Schwehm and H.A. Zook, The Ulysses dust experiment, Astron. Astrophys., 92, 411, 1992.

Henke, T., J. Woch, U. Mall, S. Livi, B. Wilken, R. Schwenn, G. Gloecker, R. von Steiger, R. J. Forsyth, A. Balogh, Differences in the O+7/O+6 ratio of magnetic cloud and noncloud coronal mass ejections, Geophys. Res. Lett., 25, 3465, 1998.

Henke, T., J.Woch, R. Schwenn, U. Mall, G. Gloeckler, R. von Steiger, R. J. Forsyth, and A. Balogh, Ionization state and magnetic topology of coronal mass ejections, J. Geophys. Res., 106, 597, 2001.

Hidalgo, M. A., A study of the expansion and distortion of the cross section of magnetic clouds in the interplanetary medium, J. Geophys. Res., 108, A8, SSH 4-1, DOI 10.1029/2002JA009818, 2003

Hidalgo, M. A., C. Cid, A. F. Vinas, and J. Sequeiros, A non-force-free approach to the topology of magnetic clouds in the solar wind, J. Geophys. Res., 106,

DOI:10.1029/2001JA900100, 2002a.

Hidalgo, M. A.; Nieves-Chinchilla, T.; Cid, C, Elliptical cross-section model for the magnetic topology of magnetic clouds, Geophys. Res. Lett., 29, 13, 15-1, DOI 10.1029/2001GL013875, 2002b.

Hirshberg, J., S. J. Bame, and D. E. Robbins, Solar fares and solar helium enrichments, Sol. Phys. 23, 467, 1972.

Ho, G. C., D. C. Hamilton, G. Gloeckler, and P. Bochsler, Enhanced Solar Wind ^{3}He^{2+} Associated With Coronal Mass Ejections, Geophys. Res. Lett. 27, 309, 2000.

Hoffmeister, C., Physikalische Untersuchungen an Kometen. I. Die Beziehungen des primären Schweifstrahls zum Radiusvektor, Z. Astrophys, 11, 265, 1943.

Hundhausen, A. J., Gilbert, H. E., Bame, S. J., Ionization state of the interplanetary plasma, J. Geophys. Res., 73, 5485, 1968.

Hurley, K., Sommer, M., Atteia, J-L., Boer, M., Cline, T., Cotin, F., Henoux, J-C., Kane, S., Lowes, P., Niel, M., Van Rooijen, J., and Vedrenne, G., The Solar X-Ray/Cosmic Gamma-Ray Burst Experiment Aboard Ulysses, Astron. Astrophys. Suppl. Ser., 92, 401, 1992.

Ipavich F.M., Lundgren R.A., Lambird B.A., Gloeckler G., Nucl. Instrum. Methods, 154, 291, 1978.

Ipavich F.M., Ma Sung L.S. and Gloeckler G., Univ. Maryland Tech. Report TR-82-172, 1982.

Joos, R., Zusammensetzung des Sonnenwindplasmas – Eichung des Sonnenwindmassenspektrometers SWICS – Zur Ionization der Elemente im Übergangsbereich der Sonnenatmosphäre, Dissertation, Physikalisches Institut Universität Bern, Bern, 1989.

Kahler, S.W., and D.V. Reames, Probing the magnetic topology of magnetic clouds by means of solar energetic particles, J. Geophys. Res., 96, 9419, 1991.

Kallenrode, M.-B., Space Physics: Plasmas and particles in the Heliosphere and Magnetospheres, Springer, 1998.

Keppler, E., et al., Description of the EPAC-Instrument for the Ulysses Mission, MPAe, 1989.

Keppler, E., J. B. Blake, D. Hovestadt, A. Korth, J. Quenby, G. Umlauft, J. Woch, The Ulysses energetic particle composition experiment EPAC, Astron. Astrophys. Suppl., 92, 317, 1992.

Keppler, E., M. Fränz, A. Korth, M. K. Reuss, J. B. Blake, R. Seidel, J. J. Quenby, and M. Witte, Observations of energetic particles with EPAC on Ulysses in polar latitudes of the heliosphere, Science, 268, 1013, 1995.

Krupp, N., E. Keppler, M. Fränz, A. Korth, M. Witte, X. Moussas, J. B. Blake, K. Naidu, J. J. Quenby, J. Woch, A. Balogh, and S. Bame, Energetic particle composition variations during the March 1991 events measured with the Ulysses EPAC instrument, Geophys. Res. Lett., 19, 1255, 1992.

Krupp N., E. Keppler, A. Korth, M. Fränz, A. Balogh, and M. K. Dougherty, Three-dimensional particle anisotropies in and near the plasma sheet of Jupiter observed

by the EPAC experiment on board the Ulysses spacecraft, Planet. Space Sci., 41, 953, 1994.

Klein, L. W., and L. F. Burlaga, Interplanetary magnetic clouds at 1 AU, J. Geophys. Res. 87, 613, 1982.

Lang, K. R., The Cambridge Encyclopedia of the Sun, Cambridge, 2001.

Lanzerotti, L.J., R.E. Gold, K.A. Anderson, T.P. Armstrong, R.P. Lin, S.M. Krimigis, M. Pick, E.C. Roelof, E.T. Sarris, G.M. Simnett, W.E. Frain, Heliosphere Instrument for spectra, composition and anisotropy at low energies, Astron. Astrophys. Suppl., 92, 349, 1992.

Larson, D. E., et al., Tracing the Topology of the October 18 − 20, 1995, Magnetic Cloud with 0.1 − 102 keV Electrons, Geophys. Res. Lett. 24, 1911, 1997.

Lepping, R. P., and K. W. Behannon, Magnetic Field directional discontinuities: 1. minimum variance errors, J. Geophys. Res., 85, 4695, 1980.

Lepping, R. P., J. A. Jones, and L. F. Burlaga, Magnetic field structure of interplanetary magnetic clouds at 1 AU, J. Geophys. Res., 95, 11957, 1990.

Lepri, S.T., T.H. Zurbuchen, L.A. Fisk, H.V. Cane, I.G. Richardson, Iron charge state distribution as an identifier of interplanetary coronal mass ejections, J. Geophys. Res., 106, 231, 2001.

Lepri, S. T. and T. H. Zurbuchen, Iron charge state distributions as an indicator of hot ICMEs: Possible sources and temporal and spatial variations during solar maximum, J. Geophys. Res., 109, A1, A01112, 2004.

Lin, N., P.J. Kellogg, K.A. Goetz, S.J. Monson, and R.J. MacDowall, Plasma Waves in Coronal Mass Ejections: Ulysses Observations, Solar Wind Nine, AIP Conference Proceedings 471, ed. S. Habbal, 673 1999.

Low, B.C., Zhang, M., The Hydromagnetic Origin of the Two Dynamical Types of Solar Coronal Mass Ejections, Astrophys. J., 564, 1 , L53, 2002.

Lundquist, S., Magneto-hydrostatic fields, Arkiv for Fysik, B2, 361, 1950.

Marsden, R.G., T.R. Sanderson, C. Tranquille, K.-P. Wenzel, and E.J. Smith, ISEE 3 observations of low-energy proton bidirectional events and their relation to isolated magnetic structures, J. Geophys., Res., 92, 11009, 1987.

Marubashi, K., Structure of the interplanetary magnetic clouds and their solar origins, Adv. Space Res., 6, 335, 1986.

Mazur, J. E., G. M. Mason, J. R. Dwyer, T. T. von Rosenvinge, Solar energetic particles inside magnetic clouds observed with the Wind spacecraft, Geophys. Res. Lett., 25, 2521, 1998.

McComas, D.J., J.T. Gosling, and J.L. Phillips, Interplanetary magnetic flux: Measurement and balance, J. Geophys. Res., 97, 171, 1992.

Meyer, J.-P., Element fractionation at work in the solar atmosphere, in Origin and Evolution of the Elements, Cambridge Univ. Press, 1993.

Montgomery, M. D., J. R. Asbridge, S. J. Bame, and W. C. Feldman, Solar Wind Electron Temperature Depressions Following Some Interplanetary Shock Waves: Evidence for Magnetic Merging?, J. Geophys. Res., 79, 3103, 1974.

Morrison, P., Solar-connected variations of the cosmic rays, Physical Reviews, 95, 641, 1954.

Munro, R. H., Gosling, J. T., Hildner, E., MacQueen, R. M., Poland, A. I., Ross, C., Sol. Phys., 61, 201, 1979.

Mulligan, T. and Russell, C. T.: Multispacecraft modeling of the flux rope structure of interplanetary coronal mass ejections: Cylindrically symmetric versus nonsymmetric topologies, J. Geophys. Res., 106, 10581, 2001.

Neugebauer, M., and C.W. Snyder, The mission of Mariner 2: Preliminary observations, solar plasma experiment, Science 138, 1095, 1962.

Parker, E.N., Dynamics of the Interplanetary Gas and Magnetic Fields, Astrophys. J., 128, 664, 1958a.

Parker, E. N., Phys. Fluids 1, 171, 1958b.

Parker, E., Sudden Expanse of the Corona Following a Large Solar Flare and the Attendant Magnetic Field and Cosmic Ray Effects, Astrophys. J., 133, 1014, 1961.

Plunkett S. P., Vourlidas A., Simberova S., Karlicky M., Kotrè P., Heinzel P., Kupryakov Yu.A., Guo W.P., Wu S.T., Simultaneous SOHO and Ground-Based Observations of a Large Eruptive Prominence and Coronal Mass Ejection; Sol. Phys., 194, 371, 2000.

Reames, D. V., Coronal Abundances Determined from Energetic Particles, Adv. Space Res., 15, 41, 1995.

Reames, D. V., Particle acceleration at the Sun and in the heliosphere, Space Sci. Rev., 90, 413, 1999.

Richardson, I. G., and Cane, H. V., Regions of Abnormally low Proton Temperatures in the Solar Wind (1965-1991) and their association with ejecta, J. Geophys. Res., 100, 23397, 1995.

Richardson, I. G., C. J. Farrugia, and H. V. Cane, A Statistical Study of the Behavior of the Electron Temperature in Ejecta, J. Geophys. Res. ,102, 4691, 1997.

Riley, P. and Crooker N. U., Kinematic Treatment of Coronal Mass Ejection Evolution in the Solar Wind, Astrophys. J., 600, 2, 1035, 2004.

Rodriguez L. and G. Stenborg, El clima espacial: satélites y astronautas en peligro?, Ciencia Hoy, 13, 10, 2003.

Rodriguez, L., J. Woch, N. Krupp, M. Fränz, R. von Steiger, R. J. Forsyth, D. B. Reisenfeld, K.-H. Glaßmeier, A statistical study of oxygen freezing-in temperature and energetic particles inside magnetic clouds observed by Ulysses, J. Geophys. Res., 109, A01108, doi:10.1029/2003JA010156, 2004.

Rodriguez L., J. Woch, N. Krupp, M. Fränz, R. von Steiger, C. Cid, R. Forsyth, K.-H. Glaßmeier, Bidirectional proton flows and comparison of freezing-in temperatures in ICMEs and magnetic clouds, Proc. IAU Symposium 226 on Coronal and Stellar Mass Ejections, Beijing, China, 2005 (submitted).

Rosner, R. et al., in Solar-Terrestrial Physics: Present and Future, Edited by D. Butler and K. Papadopoulos, NASA-PR-1120, 1984.

Russell, C. T., and Elphic, R. C., Nature, 279, 616, 1979.

Rust, D. M., The solar STEREO mission, European Space Agency, Special Publication, 417, 133, 1998.

Sanderson, T.R., Observations of three-dimensional anisotropies of 35- to 1000-keV protons associated with interplanetary shocks, J. Geophys. Res., 90, 19, 1985.

Schwenn, R., M. D. Montgomery, H. Rosenbauer, H. Miggenrider, K.-H. Mulhauser, S. J. Bame, W. C. Feldman, and R. T. Hansen, Direct observations of the latitudinal extent of a high-speed system in solar wind, J. Geophys. Res., 83, 1011, 1978.

Schwenn, R., H. Rosenbauer, K.-H. Muehlhaeuser, Singly-ionized helium in the driver gas of an interplanetary shock wave, Geophys. Res. Lett., 7, 201, 1980.

Schwenn, R., Large-Scale Structure of the Interplanetary Medium, in Physics of the Inner Heliosphere, eds. R. Schwenn and E. Marsch, Springer-Verlag, Berlín, 1991.

Shodhan, S., et al., Counterstreaming Electrons in Magnetic Clouds, J. Geophys. Res., 105, 27261, 2000.

Simpson, J.A., J. D. Anglin, A. Balogh, M. Bercovitch, J. M. Bouman, E. E. Budzinski, J. R. Burrows, R. Carvell, J. J. Connell and others, The Ulysses cosmic ray and solar particle investigation, Astron. Astrophys. Suppl., 92, 365, 1992.

Siscoe, G.L., and R.W. Suey, Significance criteria for variance matrix applications, J. Geophys. Res., 77, 1321, 1972.

Sonnerup B.O. and Cahill, L.J., Magnetopause Structure and Attitude from Explorer 12 Observations, J. Geophys. Res., 72, 171, 1967

Sonnerup, B.U.O. and M. Scheible, Minimum and Maximum Variance Analysis, in Analysis Methods for Multi-Spacecraft Data, ISSI Scientific Report, SR-001, eds. G. Paschmann and P.W. Daly, 185, 1998.

Srivastava, N., Schwenn, R., Stenborg, G, Comparative Study of Coronal Mass Ejections Associated with Eruptive prominences, in 8th SoHO Workshop, Plasma Dynamics and Diagnostics in the Solar Transition Region and Corona, ESA-SP, 446, 621, 1999.

Stone, R. G. and B. T. Tsurutani, Collisionless shocks in the heliosphere: A tutorial review, Geophysical Monograph, 34, 1985.

Stone, R.G., J. L. Bougeret, J. Caldwell, P. Canu, De Conchy, Y., N. Cornilleau-Wehrlin, M. D. Desch, J. Fainberg, K. Goetz and others, The unified radio andplasma wave investigation, Astron. Astrophys. Suppl., 92, 291, 1992.

Vandas M, Romashets E. P., A force-free field with constant alpha in an oblate cylinder: A generalization of the Lundquist solution, Astron. Astrophys., 398, 801, 2003.

von Steiger, R.; Schwadron, N. A.; Fisk, L. A.; Geiss, J.; Gloeckler, G.; Hefti, S.; Wilken, B.; Wimmer-Schweingruber, R. F.; Zurbuchen, T. H., Composition of quasi-stationary solar wind flows from Ulysses/Solar Wind Ion Composition Spectrometer, J. Geophys. Res., 105 (A12), 27,217-27,238, 2000.

Tylka, Allan J.; Reames, Donald V.; Ng, Chee K., Observations of systematic temporal evolution in elemental composition during gradual solar energetic particle events, Geophys. Res. Lett., 26, 14, 2141, 1999.

Witte, M., Rosenbauer H., Keppler E., Fahr H., Hemmerich P., Lauche H., Loidl A.,

Zwick R., The interstellar neutral-gas experiment on ULYSSES, Astron. Astrophys. Suppl. Ser., 92, 333, 1992.

Woch, J., Axford, W. I., Mall, U.,Wilken, B., Livi, S., Geiss, J., Gloeckler, G., R. J. Forsyth, SWICS/Ulysses observations: The three-dimensional structure of the heliosphere in the declining/minimum phase of the solar cycle, Geophys. Res. Lett., 24, 2885, 1997.

Zurbuchen, T. H., L. A. Fisk, G. Gloeckler, R. von Steiger, The solar wind composition throughout the solar cycle: A continuum of dynamic states, Geophys. Res. Lett., 29, 1352, 66-1, doi: 10.1029/2001GL013946, 2002.

Zurbuchen, T. H. and I. Richardson, In-Situ Solar Wind and Field Signatures of Interplanetary Coronal Mass Ejections, Space Sci. Rev., in press, 2004.

Zwickl, R. D., J. R. Asbridge, S. J. Bame, W. C. Feldman, and J. T. Gosling, He+ and Other Unusual Ions in the Solar Wind: A Systematic Search Covering 1972-1980, J. Geophys. Res., 87, 7379, 1982.

Acknowledgements

The administrative staff of the institute was always ready to help me address my problems, to them (headed by Andreas Poprawa) I am grateful. I would like to express also my recognition to our group secretary, Sibylla.

Thanks to my colleagues from the International Max-Planck Research School I felt always like at home, peculiar feeling while being in the company of people from all over the world. I thank Dr. Dieter Schmitt for coordinating the School. Special thanks go to my close friends with whom I shared the every-day life in Germany.

I continue to receive valuable support from my professors in Mendoza (Enrique, Carlos, and the people from IEMA), they were the ones who introduced me to science and taught me fundamental things (about engineering, science and life).

My friends in Argentina, who are (luckily) too many to be named here have always been there for me, even from thousands of kilometers away; gracias!.

My deepest recognition and appreciation for my family. Their support throughout these years and during my whole life has been crucial. Mirta, Pulqui, Julita y Gabriel: gracias!

Finally and most important, Hebe… it is because of her that I am writing this now. Hopefully the future will allow us to have many more experiences like this one.

Lebenslauf

Persönliche Daten

Name: Luciano Rodriguez Romboli
Geboren: 09.04.1978 in Mendoza, Argentinen
Nationalität: argentinisch

Schulbildung

1991-1994:   Gymnasium "Escuela de Comercio Martín Zapata"
1995:   Gymnasium "Corazón de María"

Studium

1996-2001:   Universidad de Mendoza, Facultad de Ingeniería,
                         Elektronik und Telekommunikation Ingenieur

Promotion

2002-2005:   Stipendiat am Max-Planck Institut für
                         Sonnensystemforschung.